



Multi-user Interference Mitigation in Visible-Light Communication Networks

Mahmoud Eltokhey

► To cite this version:

Mahmoud Eltokhey. Multi-user Interference Mitigation in Visible-Light Communication Networks. Networking and Internet Architecture [cs.NI]. Ecole Centrale Marseille, 2021. English. NNT : 2021ECDM0005 . tel-03702254

HAL Id: tel-03702254

<https://theses.hal.science/tel-03702254>

Submitted on 23 Jun 2022

HAL is a multi-disciplinary open access archive for the deposit and dissemination of scientific research documents, whether they are published or not. The documents may come from teaching and research institutions in France or abroad, or from public or private research centers.

L'archive ouverte pluridisciplinaire **HAL**, est destinée au dépôt et à la diffusion de documents scientifiques de niveau recherche, publiés ou non, émanant des établissements d'enseignement et de recherche français ou étrangers, des laboratoires publics ou privés.

École Doctorale – 352

Unité de recherche – INSTITUT FRESNEL

THÈSE DE DOCTORAT

pour obtenir le grade de

DOCTEUR de l'ÉCOLE CENTRALE de MARSEILLE

Discipline :

Optique, Photonique et Traitement d'Image

TITRE DE LA THÈSE :

**Réduction d'Interférences Multi-Utilisateurs
dans les Réseaux de Communication par la Lumière Visible**

Par

ELTOKHEY Mahmoud

Directeur de thèse : KHALIGHI Mohammad-Ali

Co-Directeur de thèse : GHASSEMLOOY Zabih

Soutenue le 22 Juin 2021

devant le jury composé de :

ALOUINI Mohamed-Slim
DI RENZO Marco
SAFARI Majid
JUNGNICKE Volker
ORTEGA Beatriz
KHALIGHI Mohammad-Ali
GHASSEMLOOY Zabih

Professor – HDR, KAUST
Directeur de recherche CNRS HDR, Université de Paris-Saclay
Associate Professor – HDR, The University of Edinburgh
Professor – HDR, Fraunhofer HHI
Professor – HDR, Universitat Politècnica de València
Maître de Conférences HDR, École Centrale de Marseille
Professor – HDR, Northumbria University

Président
Rapporteurs
Rapporteurs
Examineurs
Examineurs
Dir. de thèse
Co-Dir. de thèse

N° assigned by library
XXXX

TITLE:

**Multi-user Interference Mitigation
in Visible-Light Communication Networks**

THESIS

to obtain the degree of Doctor of Philosophy

issued by ÉCOLE CENTRALE MARSEILLE

Doctoral school : Physics and Material Sciences

Discipline : Optics, Photonics and Image Processing

Carried out at FRESNEL INSTITUTE

Presented and defended publicly by:

Mahmoud Eltokhey

on June 22nd 2021

COMMITTEE :

| | | |
|-------------------------|----------------------------|--|
| Chairman: | Prof. Mohamed-Slim Alouini | KAUST, Kingdom of Saudi Arabia |
| Reviewers: | Prof. Marco Di Renzo | CNRS, Paris-Saclay University, France |
| | Dr. Majid Safari | University of Edinburgh, United Kingdom |
| Examiners: | Prof. Volker Jungnickel | Fraunhofer HHI, Germany |
| | Prof. Beatriz Ortega | Universidad Politécnica de Valencia, Spain |
| Thesis advisors: | Dr. Mohammad-Ali Khalighi | École Centrale Marseille, France |
| | Prof. Zabih Ghassemlooy | Northumbria University, United Kingdom |

YEAR : 2021

Acknowledgments

First and foremost I thank and praise Allah. I would like to offer my sincere gratitude and thanks to my supervisor Prof. Ali Khalighi for his consistent support and guidance and his valuable insights and suggestions throughout my Ph.D. research. I want also to give my special thanks to my co-supervisor Prof. Fary Ghassemlooy, for his valuable advising and encouragement and his indispensable support. I would like to thank Prof. Mohamed-Slim Alouini, Prof. Marco Di Renzo, Prof. Majid Safari, Prof. Volker Jungnickel, and Prof. Beatriz Ortega for accepting to become members of my thesis committee and for their valuable comments and advice. I want to thank the European Commission for supporting my research through the European Union's H2020 Marie Skłodowska-Curie Innovative Training Network VisIoN project. I want to thank my wife for her care and backing, my parents for their love and support throughout my entire life, and the rest of my family for their encouragement and support. I want to thank also my colleagues from GSM team, Institut Fresnel, Ecole Centrale Marseille, and the OCRG lab at Northumbria University, and the members of VisIoN Project, for the experiences we had and the time we spent, which formed many precious memories in my life.

Funding

This work has received funding from the European Union's Horizon 2020 research and innovation programme under the Marie Skłodowska-Curie grant agreement No. 764461 (VisIoN).

RÉSUMÉ:

La communication par la lumière visible (VLC pour *Visible Light Communication*) est une technologie prometteuse pour fournir la connectivité sans-fil à grande efficacité énergétique, et est considérée comme un candidat sérieux pour les futurs réseaux de télécommunication au-delà de la 5G. Pour un déploiement dans de grands espaces, une architecture VLC cellulaire doit être adoptée en utilisant plusieurs luminaires. En outre, des solutions efficaces doivent être utilisées pour gérer la mobilité des utilisateurs, ainsi que les interférences multi-utilisateurs (MUI pour *Multi-User Interference*) lorsque plusieurs utilisateurs (ou dispositifs) doivent être connectés au réseau simultanément. Une solution simple consiste alors à utiliser la technique de pré-codage à forçage de zéro (ZF pour *Zero Forcing*) à l'émission. Cependant, ce schéma ne peut traiter qu'un nombre limité d'utilisateurs et, de plus, ses performances sont très sensibles au conditionnement de la matrice de canal. Par conséquent, des schémas de transmission d'accès multiples plus efficaces doivent être développés afin de permettre de desservir un nombre potentiellement important d'utilisateurs, tout en garantissant des transferts intercellulaires (*handover*) fluides, ainsi qu'une gestion efficace des ressources pour réduire les MUI, qui ont fait l'objet de ce travail de thèse.

Dans cette thèse, dans un premier temps, nous proposons l'optimisation des paramètres de l'émetteur et du récepteur pour améliorer les performances des réseaux VLC utilisant le pré-codage ZF, en améliorant le conditionnement de la matrice du canal. Ensuite, et afin de gérer un nombre potentiellement grand d'utilisateurs, nous proposons de nouvelles techniques d'accès multiple, qui permettent une réduction efficace des MUI et une amélioration des performances du réseau. En particulier, nous proposons un schéma hybride de pré-codage ZF et d'accès multiple non-orthogonal (NOMA pour *Non-Orthogonal Multiple-Access*), où le pré-codage ZF est utilisé pour diffuser les signaux des utilisateurs se trouvant au bord des cellules avec l'ordre de décodage le plus élevé dans le schéma NOMA. D'autre part, pour le cas d'une transmission basée sur le schéma NOMA, et pour permettre une adaptation aux variations de l'intensité lumineuse, nous proposons une solution de gestion des MUI basée sur la planification temporelle et la coordination des transmissions au sein de chaque cellule. Enfin, nous étudions le cas de la mobilité des utilisateurs et proposons de nouvelles techniques de *handover* qui permettent une amélioration du débit et de la fiabilité des connexions.

MOTS-CLÉS : Communication par la lumière visible ; accès multiple ; interférences multi-utilisateurs; réseaux Li-Fi cellulaires ; NOMA ; pré-codage ZF; handover.

ABSTRACT:

Visible light communication (VLC) is a promising technology for providing energy-efficient wireless connectivity in both indoor and outdoor environments, and is regarded as a serious candidate for providing wireless access in beyond-5G networks. When deployed in large spaces, a multi-cell architecture needs to be adopted using multiple luminaires. In addition, efficient solutions should be used to manage the user mobility, as well as the multi-user interference (MUI) when multiple users (or devices) should be connected to the network. There, a simple solution is that of multi-user multiple-input single-output (MU-MISO) with zero-forcing (ZF) pre-coding at the transmitter. However, this scheme can only handle a limited number of users and, furthermore, its performance is very sensitive to the condition number of the network channel matrix. More efficient multiple-access (MA) signalling schemes need to be designed in order to allow serving potentially large numbers of users, while ensuring smooth handovers as well as efficient resource management to mitigate MUI, which has been the subject of this research.

In this thesis, firstly, we propose the optimization of the transmitter and the receiver parameters to improve the performance of the ZF pre-coding VLC networks, by decreasing the correlation in the network channel matrix. Following this, and in order to handle a potentially large number of users, we propose novel MA techniques, which allow efficient MUI mitigation and improved network performance. In particular, we propose a hybrid non-orthogonal multiple-access (NOMA)-ZF pre-coding scheme, where ZF pre-coding is used for broadcasting the signals of the cell-edge users with the highest decoding order in the NOMA scheme. On the other hand, for the case of NOMA-based transmission, we propose handling MUI in a dimming-aware manner, through efficient time-scheduling, scaling, and coordination of the transmissions within each cell. Furthermore, we investigate the case of user mobility, and propose new efficient soft handover techniques, which guarantee an improved network throughput and reliability.

KEYWORDS : Visible-light communications; multi-user interference; multiple-access techniques; cellular Li-Fi networks; NOMA; ZF pre-coding; handover.

Table of contents

| | | |
|----------|--|-----------|
| 1 | Introduction | 1 |
| 1.1 | Overview of visible-light communication | 1 |
| 1.1.1 | Wireless communications | 1 |
| 1.1.2 | Optical communications | 2 |
| 1.1.3 | VLC | 2 |
| 1.2 | VisIoN project | 6 |
| 1.3 | Thesis objectives | 6 |
| 1.4 | Thesis overview and contributions | 7 |
| 1.4.1 | Thesis outline | 7 |
| 1.4.2 | Author's contributions | 9 |
| 1.4.3 | Author's publications | 9 |
| 2 | Multi-cell VLC Networks | 11 |
| 2.1 | Introduction | 12 |
| 2.2 | VLC system | 13 |
| 2.2.1 | Tx | 13 |
| 2.2.2 | Rx | 13 |
| 2.2.3 | VLC channel | 14 |
| 2.2.4 | Signal modulation | 15 |
| 2.2.5 | VLC uplink | 16 |
| 2.2.6 | Multi-cell VLC system | 17 |
| 2.3 | Interference mitigation in multi-cell VLC networks | 18 |
| 2.3.1 | Linear pre-coding | 18 |
| 2.3.2 | MA techniques | 21 |

| | | |
|----------|---|-----------|
| 2.4 | Optimization of VLC systems | 23 |
| 2.4.1 | PSO | 24 |
| 2.5 | Chapter summary | 26 |
| 3 | UAV Locations Optimization in MISO ZF Pre-coded VLC Networks | 29 |
| 3.1 | Introduction | 29 |
| 3.1.1 | UAV-based BSs | 30 |
| 3.2 | System model | 31 |
| 3.3 | UAV locations optimization | 31 |
| 3.4 | Performance analysis | 33 |
| 3.4.1 | Performance over different optimization parameters | 35 |
| 3.4.2 | Case study of UAVs with optimized and non-optimized locations | 36 |
| 3.4.3 | Performance of optimized UAV locations in case of mobility | 38 |
| 3.5 | Chapter summary | 38 |
| 4 | Rx FOV Optimization in MISO ZF Pre-coded VLC Networks | 41 |
| 4.1 | Introduction | 41 |
| 4.2 | System model | 43 |
| 4.3 | FOV optimization | 43 |
| 4.4 | Performance analysis | 47 |
| 4.4.1 | Performance over different optimization parameters | 47 |
| 4.4.2 | Case study of optimized and non-optimized FOVs | 49 |
| 4.4.3 | Performance over random Rx locations | 49 |
| 4.4.4 | Performance in the case of user mobility | 51 |
| 4.5 | Chapter summary | 52 |
| 5 | Performance Comparison Between OFDMA and NOMA | 55 |
| 5.1 | Introduction | 55 |
| 5.2 | Performance analysis | 56 |
| 5.2.1 | OFDMA-based signal transmission | 56 |
| 5.2.2 | NOMA-based signal transmission | 56 |
| 5.3 | Performance comparison | 59 |
| 5.4 | Chapter summary | 63 |

| | |
|--|-----------|
| 6 Hybrid NOMA-ZF pre-coding for VLC Networks | 65 |
| 6.1 Introduction | 65 |
| 6.2 Hybrid NOMA-ZFP | 66 |
| 6.2.1 Concept | 66 |
| 6.2.2 NOMA-ZFP schemes | 68 |
| 6.3 Performance study of hybrid NOMA-ZFP schemes | 69 |
| 6.3.1 Main assumptions and considered scenarios | 70 |
| 6.3.2 Performance study | 73 |
| 6.3.3 Computational complexity and network latency | 79 |
| 6.4 Chapter summary | 81 |
| 7 Time-Sliced NOMA for Multi-Cell VLC Networks | 83 |
| 7.1 Introduction | 83 |
| 7.2 System model | 85 |
| 7.3 TS-NOMA signaling | 85 |
| 7.3.1 Concept | 85 |
| 7.3.2 TS-NOMA schemes | 87 |
| 7.3.3 Time-slot fixing strategies | 88 |
| 7.4 Performance analysis | 89 |
| 7.4.1 Main assumptions and considered scenarios | 89 |
| 7.4.2 Numerical results | 90 |
| 7.5 Chapter summary | 93 |
| 8 Addressing User Handover in Multi-Cell VLC Networks | 95 |
| 8.1 Introduction | 95 |
| 8.2 Handover-aware scheduling | 97 |
| 8.2.1 Single cluster network | 97 |
| 8.2.2 Multiple cluster network | 101 |
| 8.3 Time scheduling strategies study | 104 |
| 8.3.1 Time scheduling strategies | 105 |
| 8.4 Performance analysis | 105 |
| 8.4.1 Main assumptions and considered scenarios | 105 |
| 8.4.2 Numerical results | 106 |

| | |
|---|------------|
| 8.5 Chapter summary | 110 |
| 9 Experimental Investigation of Effect of PA in NOMA | 111 |
| 9.1 Introduction | 111 |
| 9.2 Experiment setup | 111 |
| 9.3 Effect of varying PA coefficient in NOMA | 114 |
| 9.4 Chapter summary | 114 |
| 10 Conclusions and Perspectives | 117 |
| 10.1 Conclusions | 117 |
| 10.2 Perspectives | 119 |
| List of Figures | 121 |
| List of Tables | 127 |
| Bibliography | 129 |

Résumé étendu

Ces dernières années, la communication par lumière visible (VLC pour *Visible-Light Communication*) a suscité un intérêt croissant en tant que solution pour les réseaux de communication à haut débit dépassant la 5G. Par rapport aux communications par radiofréquence (RF), les avantages des VLC sont nombreux, notamment une bande passante très large, qui permet de fournir un débit élevé à faible coût, ainsi qu'une utilisation efficace des ressources en exploitant les luminaires déjà installés pour assurer en même temps l'éclairage et la communication. En outre, cette technologie permet de sécuriser le réseau et de réutiliser les fréquences en profitant de l'impossibilité d'accéder aux signaux lumineux dans les pièces voisines en raison du confinement de la lumière, ce qui renforce la sécurité de la couche physique et permet d'augmenter la capacité du réseau en réutilisant les mêmes bandes de fréquences dans les pièces voisines. En utilisant la lumière pour le transfert de données, le VLC peut fournir une solution de communication dans les zones sensibles aux interférences électromagnétiques, comme les hôpitaux.

La Figure 1 montre le schéma général d'un système VLC, où les données utilisateur sont transmises à travers un luminaire, et ensuite réceptionnées du côté de l'utilisateur par un photodétecteur, qui convertit les signaux optiques reçus en signaux électriques correspondants avant d'être traités pour récupérer les données transmises. En raison de ses mérites, le VLC a été considéré dans divers cas d'utilisation indoor comme un complément au WiFi, pour fournir des communications à haut débit, prendre en charge la connectivité sans fil dans des scénarios industriels et dans les établissements de santé, sensibles aux interférences électromagnétiques, et pour réaliser la localisation indoor. En outre, VLC a également été envisagé pour les scénarios outdoor, bénéficiant de l'utilisation généralisée de l'éclairage à dans les lampadaires, les phares et les feux arrière des véhicules, et dans les véhicules aériens sans pilote (UAV pour *Unmanned-Aerial Vehicle*) fonctionnant la nuit. La Figure 2 illustre l'utilisation des VLC dans divers applications indoor et outdoor.

Malgré ses avantages, le VLC souffre du blocage du chemin direct entre les luminaires et les appareils utilisateurs, ce qui dégrade la puissance des signaux reçus. En considérant le luminaire comme étant un point d'accès (AP pour *Access Point*) chargé de fournir un éclairage et une connectivité sans fil aux utilisateurs dans la zone éclairée (càd la cellule), l'utilisation de plusieurs luminaires peut être assimilée à un scénario de communication multicellulaire. Dans les scénarios VLC multicellulaires, en raison des intersections entre les zones des cellules, les utilisateurs

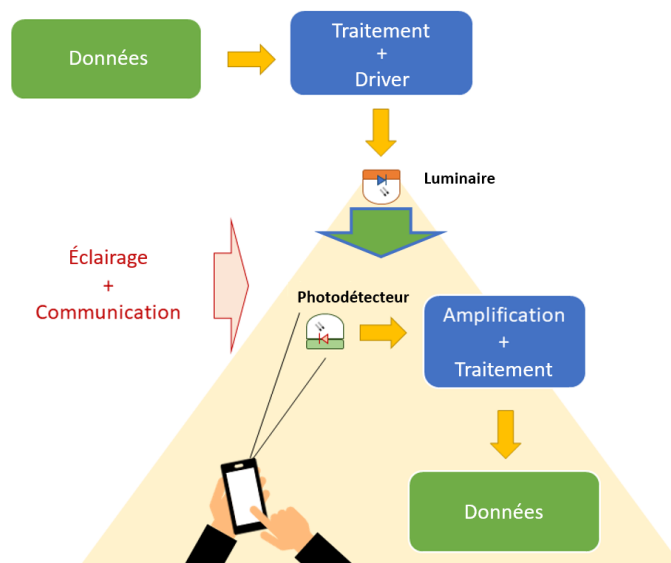


Figure 1 — Le schéma général d'un système VLC.

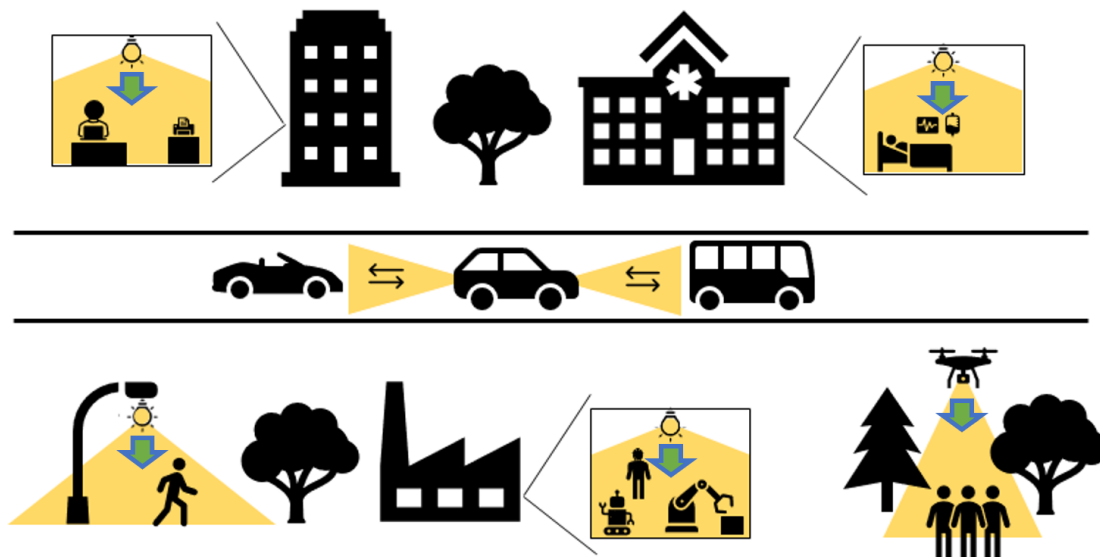


Figure 2 — L'utilisation des VLC dans divers applications indoor et outdoor.

peuvent subir des interférences (c'est-à-dire recevoir des signaux non désirés destinés à d'autres utilisateurs), ce qui limite leurs débits atteignables. Ces interférences sont incontrôlables dans de nombreux cas en raison de l'emplacement des luminaires qui suit des considérations architecturales et d'éclairage. La quantité d'interférences dépend de nombreux de facteurs, notamment l'emplacement des utilisateurs et des luminaires, et les techniques utilisées pour transmettre les signaux des utilisateurs.

De plus, en raison de la mobilité des utilisateurs, les mouvements fréquents des utilisateurs entre les cellules provoquent des modifications subséquentes des points d'accès à partir desquels

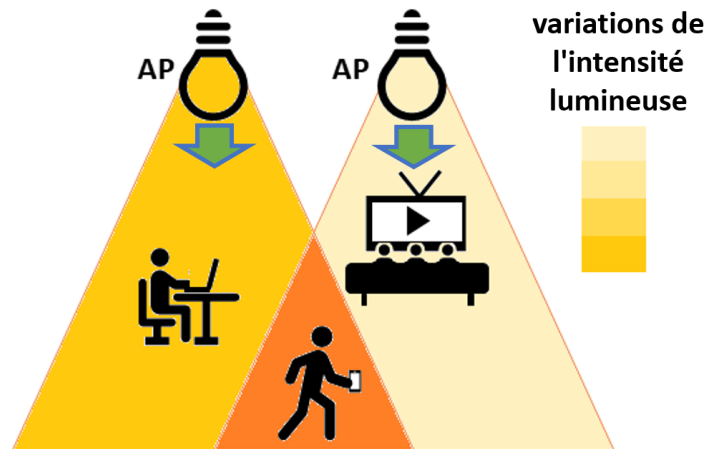


Figure 3 — Un exemple de scénario VLC multicellulaire.

ils reçoivent les données (c'est-à-dire qui sont effectués via un processus nommé (*handover*)), provoquant des coupures de liaison, ce qui affecte la fiabilité de la liaison de communication. De plus, pour satisfaire les besoins d'éclairage des utilisateurs, les systèmes VLC doivent tenir compte des exigences de variations de l'intensité lumineuse dans l'environnement de communication, tout en garantissant l'efficacité de la liaison de communication. La Figure 3 montre un exemple de scénario VLC multicellulaire, mettant en évidence l'intersection entre les zones d'éclairage, les transitions des utilisateurs entre les zones de couverture des différents APs et les différentes exigences de dimming dans les cellules.

Dans cette thèse, nous nous concentrons sur les problèmes associés aux scénarios VLC multicellulaires. En particulier, nous abordons les problèmes d'interférence, en tenant compte de différents aspects tels que les exigences de dimming, les handovers entre les cellules et l'exploitation des degrés de liberté spatiale au niveau des émetteurs (Tx) et des récepteurs (Rx).

Après avoir présenté une brève introduction aux systèmes VLC dans le Chapitre 1. Nous donnons au Chapitre 2 un aperçu des composants du système VLC, tels que les Tx et Rx, suivi d'une discussion sur le canal VLC, les schémas de signalisation et la configuration envisagée pour les réseaux VLC multicellulaires. De plus, nous discutons des différentes techniques multi-utilisateurs pour VLC, en commençant par les schémas de pré-codage et en terminant par les principales techniques MA considérées dans les réseaux VLC. Enfin, nous discutons des différents outils pouvant être utilisés pour l'optimisation des VLCs afin d'améliorer les performances, en mettant en évidence ceux qui s'accordent avec les caractéristiques des réseaux VLC considérés.

Pour discuter des solutions proposées afin d'augmenter la densité d'utilisateurs dans les réseaux VLC, nous étudions au Chapitre 3 l'optimisation des performances des réseaux VLC pré-codés zero-forcing (ZF), dans lesquels les UAVs sont utilisées pour fournir un éclairage et une communication simultanés, dans des scénarios industriels indoor et outdoor. L'optimisation par essaims particulaires (PSO pour *Particle Swarm Optimization*) est utilisée pour optimiser les em-

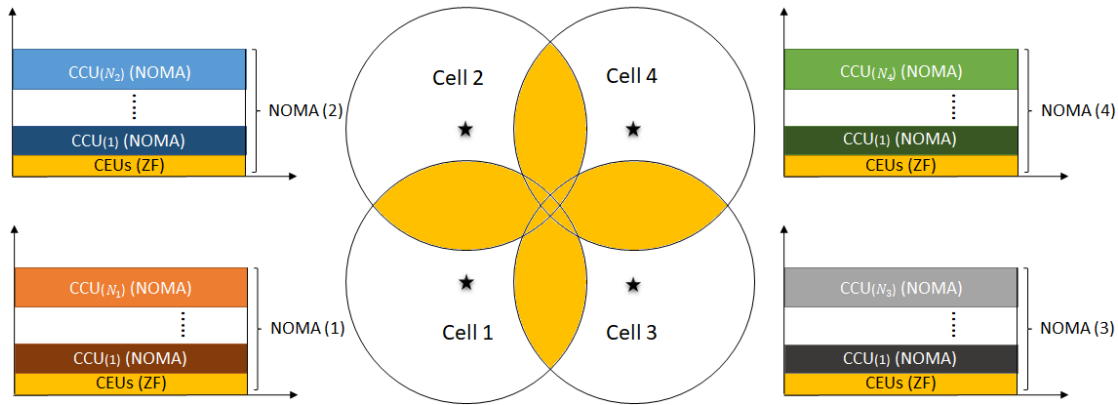


Figure 4 — le schéma de pré-codage hybride NOMA-ZF proposé.

placements des UAVs, pour réduire la corrélation dans la matrice des canaux du réseau, dans le but d'améliorer le débit utilisateur réalisable dans le réseau. Une comparaison est effectuée entre les performances du réseau pour les cas d'emplacements UAVs optimisés et non optimisés dans différentes conditions de mobilité des utilisateurs.

Dans Chapitre 4 nous proposons une amélioration des performances du pré-codage ZF dans les réseaux VLC indoor, en optimisant les angles de réception Rx (càd champs de vision (FOV pour *Field-of-View*)) des utilisateurs en utilisant PSO afin de diminuer la corrélation dans la matrice de canal de réseau. Nous comparons les performances des FOV optimisés et non optimisés. De plus, nous proposons une modification de l'algorithme proposé pour diminuer le temps d'optimisation, qui est comparé à l'algorithme d'origine et aux FOV non optimisés.

Pour gérer un plus grand nombre d'utilisateurs au sein du système VLC que ceux considérés aux Chapitres 3 et 4, nous envisageons d'utiliser les techniques d'accès multiple dans le réseau VLC. Nous commençons au Chapitre 5 en comparant numériquement les techniques d'accès multiple les plus performantes du Chapitre 2, l'accès multiple par répartition orthogonale de la fréquence (OFDMA pour *Orthogonal Frequency Division Multiple Access*) et l'accès multiple non orthogonal dans le domaine de puissance (NOMA pour *Non-Orthogonal Multiple Access*), avant de discuter du développement de NOMA.

Sur la base des résultats de la comparaison du Chapitre 5, nous développons au Chapitre 6 une solution d'atténuation des interférences pour les réseaux VLC multicellulaires basés sur NOMA. En particulier, le pré-codage ZF est utilisé pour diffuser les signaux des utilisateurs qui souffrent d'interférences intercellulaires (ICI pour *Inter-Cell Interference*), c'est-à-dire les interférences résultant de la réception de signaux provenant de cellules voisines, tout en transmettant le signal de pré-codage ZF par chaque point d'accès comme le signal d'un seul utilisateur NOMA. En effet, le nombre d'utilisateurs desservis par le pré-codage ZF est limité. Les performances du schéma de pré-codage hybride NOMA-ZF proposé sont comparées à celles du NOMA classique en termes de débit atteignable par l'utilisateur et d'équité du réseau. La Figure 4 illustre le schéma de pré-codage hybride NOMA-ZF proposé.

Pour gérer un plus grand nombre d'utilisateurs souffrant d'ICI, tout en tenant compte des exigences de dimming du réseau VLC, nous proposons en Chapitre 7 une planification et une coordination efficaces de la transmission NOMA dans chaque cellule, dans le but de maximiser le débit réalisable et l'équité du réseau. La performance de la planification sensible au dimming proposée est comparée à celle du NOMA conventionnel sur différentes conditions de dimming.

Pour résoudre le problème de handover associé à la prise en compte des techniques d'accès multiple dans les réseaux VLC multicellulaires, nous proposons au Chapitre 8 des solutions de planification prenant en charge le handover, pour les réseaux VLC à petite/moyenne échelle et à grande échelle, afin d'améliorer la fiabilité de la liaison lors des transferts des utilisateurs, et le débit atteignable par l'utilisateur dans le réseau. Les performances du schéma proposé sont comparées à celles d'un handover sans ordonnancement.

Dans le Chapitre 9, nous évaluons expérimentalement les performances de NOMA pour les réseaux VLC. Nous montrons l'effet de la variation des paramètres NOMA sur les performances de l'utilisateur. Le Chapitre 10 conclut la thèse et discute des perspectives de travaux futurs.

List of Acronyms

6G 6th generation

ACO-OFDM Asymmetrically clipped optical orthogonal frequency-division multiplexing

ADC Analog-to-digital converter

ADR Angle-diversity receiver

ANFR Agence nationale des fréquences

AP Access point

APD Avalanche photodetector

AWG Arbitrary waveform generator

AWGN Additive white Gaussian noise

BER Bit error rate

Bias-T Bias-tee

bps Bits per second

BS Base station

CCU Cell-centre user

CDF Cumulative distribution function

CDMA Code division multiple access

CEU Cell-edge user

CP Cyclic prefix

CSI Channel state information

CSMA/CA Carrier-sense multiple access with collision avoidance

| | |
|-----------------|---|
| DAC | Digital-to-analog converter |
| DCO-OFDM | Direct current optical orthogonal frequency-division multiplexing |
| EMI | Electromagnetic interference |
| FFT | Fast Fourier transform |
| FI | Fairness index |
| FOV | Field-of-view |
| GPS | Global positioning system |
| HOM | Handover margin |
| ICI | Inter-cell interference |
| IFFT | Inverse fast Fourier transform |
| IM | Intensity modulation |
| IM/DD | Intensity modulation and direct detection |
| IoT | Internet-of-Things |
| ITU | International Telecommunication Union |
| IUI | Inter-user interference |
| LAN | Local area network |
| LBR | Line-blocked receiver |
| LED | Light-emitting diode |
| LOS | Line-of-sight |
| MA | Multiple access |
| MADR | Mirror-aided diversity receiver |
| MDR | Mirror diversity receiver |
| MMSE | Minimum mean-square-error |
| MU-MIMO | Multi-user multiple-input multiple-output |
| MU-MISO | Multi-user multiple-input single-output |
| NLOS | Non-line-of-sight |

| | |
|-----------------|--|
| NOMA | Non-orthogonal multiple access |
| NOMA-ZFP | Non-orthogonal multiple access-zero forcing pre-coding |
| Ofcom | Office of Communication |
| OFDM | Orthogonal frequency-division multiplexing |
| OFDMA | Orthogonal frequency division multiple access |
| OOK | ON-OFF keying |
| OWC | Optical wireless communication |
| P/S | Parallel to serial |
| PAM | Pulse-amplitude modulation |
| PAR | Prism array receiver |
| PD | Photodetector |
| PIN | Positive-intrinsic-negative |
| PPM | Pulse-position modulation |
| PSO | Particle swarm optimization |
| PWM | Pulse-width modulation |
| QAM | Quadrature amplitude modulation |
| QoS | Quality of service |
| RF | Radio frequency |
| ROA | Receiving orientation angle |
| Rx | Receiver |
| S/P | Serial to parallel |
| SDMA | Space division multiple access |
| SIC | Successive interference cancellation |
| SINR | Signal-to-interference-plus-noise ratio |
| SiPM | Silicon photo-multiplier |
| SNR | Signal-to-noise ratio |

SSR Spatially separated receiver

TDMA Time division multiple access

TIA Transimpedance amplifier

TS-NOMA Time-sliced non-orthogonal multiple access

TTT Time to trigger

Tx Transmitter

UAV Unmanned aerial vehicle

UV Ultraviolet

VLC Visible-light communication

VLCC Visible Light Communications Consortium

WDM Wavelength-division multiplexing

ZF Zero-forcing

Chapter 1

Introduction

Contents

| | |
|--|----------|
| 1.1 Overview of visible-light communication | 1 |
| 1.1.1 Wireless communications | 1 |
| 1.1.2 Optical communications | 2 |
| 1.1.3 VLC | 2 |
| 1.1.3.1 VLC advantages | 3 |
| 1.1.3.2 VLC applications | 4 |
| 1.1.3.3 VLC challenges | 4 |
| 1.2 VisIoN project | 6 |
| 1.3 Thesis objectives | 6 |
| 1.4 Thesis overview and contributions | 7 |
| 1.4.1 Thesis outline | 7 |
| 1.4.2 Author's contributions | 9 |
| 1.4.3 Author's publications | 9 |

1.1 Overview of visible-light communication

1.1.1 Wireless communications

Wireless communication has been playing an important role in the current era of information technology. It forms the core of many concepts used in everyday-life such as cellular telecommunications and global positioning system (GPS) localization. In indoor scenarios, where it is estimated that more than 70% of wireless traffic takes place [1], wireless connectivity is essential for supporting the local area networks (LANs), and the internet-of-things (IoT) applications. Recently, the pandemic outbreak of COVID-19, and its subsequent sanitary measures, such as curfews, teleworking, and remote education, increased the internet traffic [2], and raised the pressure

on the wireless LANs. In parallel, due to the growing increase in the multimedia applications, and the number of wireless-connected user devices, wireless LANs suffer from the limitations on the available radio frequency (RF) spectrum to satisfy user data demands. Generally, one of the main problems in wireless communications is the availability of RF spectrum, which is licensed globally by the International Telecommunication Union (ITU), and locally by the regulatory bodies such as *Agence Nationale des Fréquences* (ANFR) in France and the *Office of Communications* (Ofcom) in the United Kingdom. In fact, most of the RF spectrum ranged up to 300 GHz has been considered for different wireless standards, and limited spectrum is left for exploitation. To satisfy the ongoing increase in demand for wireless data traffic, the main approaches considered include (i) improving the spectral efficiency of the current existing RF solutions; and (ii) using the available spectrum beyond 300 GHz (e.g., terahertz and optical frequency bands). By considering the latter approach, use of optical frequency bands for wireless data transmission, which is referred to as “optical wireless communication (OWC)”, emerges as an interesting solution, to benefit from its huge and unlicensed bandwidth, and the solid state optical technology advancements [3, 4].

1.1.2 Optical communications

Use of optical signals is among the oldest communication forms used by mankind. It has been realized for transmitting predefined messages through different forms, including the use of fire beacons located on high altitudes, and the use of smoke signals [5]. However, achieving optical communications using a practical communication system dates back to 1880, when Graham Bell transmitted the variations due to the voice signals through a corresponding vibration of a mirror that reflected sunlight [6, 7]. Currently, OWC can be carried out in different bands, such as the infrared (IR) [8, 9], visible [10, 11], and ultraviolet (UV) [12]. Use of visible bands for communication, which is referred to as “visible-light communication (VLC)”, has been of particular interest, backed by the widespread use of the light-emitting diode (LED)-based lighting, to achieve simultaneous illumination and communication as well as indoor positioning and sensing [13, 14]. Using LED luminaires for data transmission could be achieved by varying the light signals, according to the transmitted data, at higher rates than those perceived by human eye, to guarantee a uniform lighting experience for the users [15]. Figure 1.1 shows a general illustration for a VLC system, where an LED luminaire transmits user data, while a photo-detecting component at the user side converts the received optical signals into corresponding electrical signals that are then processed to recover the transmitted data.

1.1.3 VLC

First research on VLC was carried out in Japan in early 2000s [10, 16], followed by the establishment of the Visible Light Communication Consortium (VLCC) in Japan in 2003, to guide VLC promotion and standardization. Since then, there have been many research and standardization activities across the world on the VLC technology. Currently, among the leading funding bodies of VLC re-

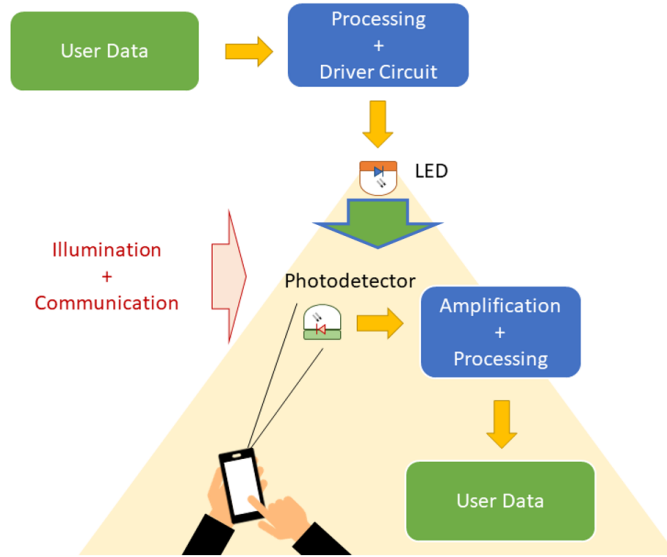


Figure 1.1 — Demonstration of a VLC system, highlighting transmission of the user data using light signals by an LED luminaire, and reception of the data by the user after processing the received signals.

search activities is the European Union’s Horizon 2020 research and innovation programme, with the training networks VisIoN [17] and ENLIGHT’EM [18] and the COST Action NEWFOCUS [19] among the most recently funded activities.

1.1.3.1 VLC advantages

Compared to RF-based wireless communications technologies, VLC offers a number of advantages, including:

- **Huge unregulated bandwidth:** As VLC offers about 300 THz of unlicensed spectrum [20], it provides cost-efficient opportunities to achieve high data rates, e.g., to support the 6th generation (6G) wireless networks and the 4th industrial revolution (Industry 4.0).
- **Efficient resource utilization:** By exploiting the existing LED-based lighting infrastructure (i.e., LED luminaires), VLC dually uses the luminaires to provide simultaneous illumination and communication.
- **Security and frequency reuse:** VLC benefits from the inability to access the light signals from neighbouring rooms, due to light confinement, which increases the physical layer security and allows increasing the network capacity by reusing the same frequency bands in neighbouring rooms.
- **Absence of RF-induced interference:** By using light for data transfer, VLC offers a communication solution in the areas that are sensitive to the electromagnetic interference (EMI), such as hospitals.



Figure 1.2 — Illustration for different indoor use cases of VLC in rooms/offices and factories (industrial scenarios) to provide high data rate communications, and in hospitals for communications in EMI-sensitive scenarios. Shown also are outdoor use cases of VLC in inter-vehicular communications, communications using streetlights, and communications using UAVs in remote and hard-to-reach areas.

1.1.3.2 VLC applications

Because of the merits of VLC, it has been considered in various use cases in indoor scenarios such as (i) complementing WiFi in providing broadband communications [21, 22], given the wide deployment of LED-based lighting solutions for their energy efficiency, and its advantage of inherent security; (ii) supporting wireless connectivity in industrial scenarios [23, 24], while mitigating EMI; (iii) and healthcare applications [22, 25], while not effecting the operation of EMI-sensitive devices; and (iv) indoor localization [26, 27] along with data transfer by efficient utilization of the lighting luminaires.

In addition, VLC has been also considered in outdoor application scenarios, benefiting from the widespread use of LED-based illumination in (i) streetlights to provide data transfer for users in the streets and at bus stops [28]; (ii) headlights and taillights of vehicles to enable inter-vehicular communications, and communications with other network nodes [29, 30]; and (iii) unmanned-aerial vehicles (UAVs) operating at night time (e.g., for search and rescue, night delivery, path illumination, etc.) [31–33]. Figure 1.2 shows an illustration for the use of VLC in various indoor and outdoor use cases.

1.1.3.3 VLC challenges

Despite the above mentioned VLC advantages, the transmitted signal can be affected by the limited dynamic range of the LED or its driver, as well as its limited modulation bandwidth. Fur-

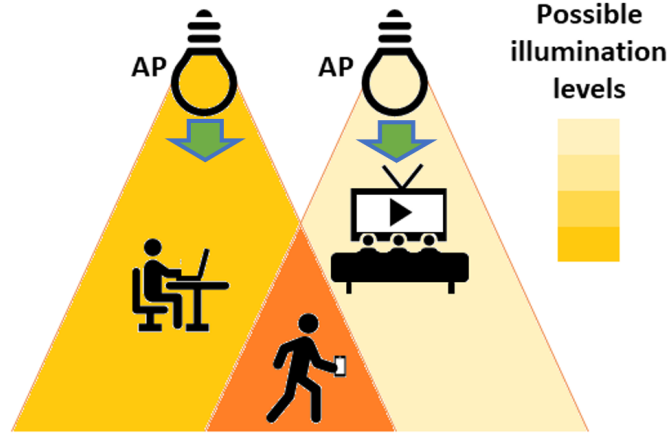


Figure 1.3—An example of multi-cell VLC scenario, in which two APs provide illumination and communication to the users, highlighting different dimming needs (i.e., different illumination levels) for the users, and transition of user between cells.

thermore, the movement of user devices can lead to the blockage of the line-of-sight (LOS) path between the LED luminaires and the user devices, which can result in the degradation of the received signal quality, and hence, the link performance.

By considering the LED luminaire as an access point (AP) responsible for providing lighting and wireless communication to the users within the illuminated area (i.e., cell), using multiple LED luminaires can be regarded as a multi-cell scenario. In multi-cell VLC scenarios, due to the intersections between the areas of the cells, which is uncontrollable in many use cases due to the placement of the LED luminaires following architectural and lighting considerations, users may suffer from interference (i.e., receiving signals intended for other users), which limits their achievable data rates. The amount of interference depends on many factors including the locations of the users and the LED luminaires, and the techniques used for transmitting the user signals.

In addition, due to user mobility, frequent movement of the users between the cells causes subsequent changes of the APs from which they receive data (i.e., which is carried out through a process named “handover”), causing link interruptions, which affects the reliability of the communication link.

Moreover, to satisfy the user illumination needs, VLC systems have to account for the dimming requirements in the communications environment, while ensuring the communications link efficiency. Figure 1.3 shows an example of multi-cell VLC scenario, highlighting the intersection between the LED illumination areas, transitions of user between the AP coverage areas, and the different dimming requirements in the cells.

1.2 VisIoN project

This PhD thesis has been funded by the European Union's Horizon 2020 research and innovation programme under the Marie Skłodowska-Curie grant agreement No. 764461 (VisIoN: Visible light based Inter operability and Networking). VisIoN project is a Marie Skłodowska-Curie Innovative Training Network (MSCA ITN) [17], which offers training for 15 early-stage researchers (ESRs) working in the area of VLC, on technical topics (e.g., PhD courses, organized tutorials and workshops), and non-technical topics (e.g., entrepreneurship, science dissemination). The project is carried out by partnership of universities, research institutes, and industrial partners located in 7 countries.

VisIoN is structured around individual research projects, each assigned to an ESR. The targeted use cases include using VLC in indoor and outdoor scenarios, smart transportation, and healthcare and industrial environments. The research programme is based on 3 technical Work packages (WPs), which are (i) WP2: Smart Cities, Offices and Homes; (ii) WP3: Smart Transportation; and (iii) WP4: Manufacturing and Medical. This research was carried out as part of WP2, which addresses proposing reliable, high-speed VLC solutions for indoor and outdoor scenarios.

As a part of VisIoN project, I had a 6-month secondment to the Optical Communications Research Group (OCRG) at Northumbria University, United Kingdom. During the secondment I gained experience on developing experimental testbeds for VLC, benefiting from the expertise of the members of the OCRG in building testbeds for different optical communications solutions. I also participated in discussions and meetings with the members of OCRG addressing the development of different optical communications solutions.

1.3 Thesis objectives

This thesis focuses on the multi-cell VLC networks. In particular, we address the problem of interference management, while accounting for different aspects such as dimming requirements, handover between cells, and exploiting the spatial degrees of freedom at the transmitters (Tx) and at the receivers (Rx).

To handle multiple users in multi-cell VLC networks while mitigating interference, two approaches could be considered. The first approach is broadcasting the user data by the APs while pre-coding the transmitted signals according to the user's experience (i.e., strength of the communication link between the user and each of the APs), to fully use the time and the frequency resources in the network. However, this comes at the expense of constraints on the number of users that can be handled, and the sensitivity of the performance to the correlation between user experiences (channel gains), where a higher correlation (e.g., for the case of users getting closer together) results in a performance degradation. For this approach we propose optimizing the VLC system parameters at the AP and the user sides to decrease such correlations and to improve the achievable throughput performance. To increase the flexibility on the number of users handled by

the VLC network, the second approach consists in distributing the channel resources (e.g., time, frequency) among users using non-precoded multiple access (MA) schemes (in this thesis we will simply refer to them as MA schemes). However, careful resource management is needed to minimize the interference for the users located in intersection areas between cells, which receive signals from multiple APs. In addition, due to user transfers between the cells because of mobility, link interruptions may occur as a result of handovers between the data-providing APs, which affects the reliability of the communications. We propose solutions to improve both the interference mitigation capabilities of the MA techniques and the handover performance in the VLC network. To achieve these objectives, we proceeded by the following steps:

- We briefly introduce the components of the multi-cell VLC networks, before discussing the pre-coding and the MA techniques used in VLC (**Chapter 2**).
- We propose optimization of the AP parameters in the pre-coded VLC network, to decrease the correlation between the user channel gains, and to improve the network performance (**Chapter 3**).
- We consider the optimization of the Rx parameters to improve the pre-coded VLC network performance through decreasing the correlation between user channel gains (**Chapter 4**).
- We compare the performance of different MA techniques, with respect to the multi-cell VLC networks, to select the most compatible technique, with respect to the desired system characteristics, for further development (**Chapter 5**).
- We develop interference mitigation solutions for the MA technique selected in Chapter 5, while accounting for different design constraints, such as the transmit power and the dimming requirements (**Chapters 6 and 7**).
- We further propose solutions for improving the communications reliability and performance during user handovers in the multi-cell VLC network (**Chapter 8**).
- We consider experimental implementation of MA solutions (**Chapter 9**).

1.4 Thesis overview and contributions

1.4.1 Thesis outline

This dissertation comprises 10 chapters, including this introduction as **Chapter 1**.

Chapter 2 presents a brief introduction to the VLC system components, such as the Tx and the Rx, followed by discussing the VLC channel, the signalling schemes, and the considered configuration for the multi-cell VLC network. Furthermore, we discuss different multi-user (MU) techniques for VLC, starting with the pre-coding schemes, and ending with the main MA techniques

considered in VLC networks. Lastly, we discuss the optimization of VLC networks to improve performance.

For discussing the proposed solutions for MU VLC in the order of increasing user density, we study in **Chapter 3** performance optimization of UAV-based ZF pre-coded VLC networks, in which LEDs are mounted on the UAVs to provide simultaneous lighting and communication, in indoor industrial and outdoor scenarios. Particle swarm optimization (PSO) is used to optimize the locations of the UAVs, to reduce the correlation in the network channel matrix, with the goal of improving the achievable user throughput in the network. A comparison is carried out between the network performance for the cases of optimized and non-optimized UAV locations over different user mobility conditions.

Moving to a denser scenario than that in Chapter 3, we propose in **Chapter 4** improvement of the ZF pre-coding performance in indoor VLC networks, by optimizing the Rx field-of-views (FOVs) of the users using PSO to decrease the correlation in the network channel matrix. We compare the network performance with optimized and non-optimized FOVs. In addition, we propose a modification of the proposed algorithm to decrease the optimization time.

To handle still a larger number of users within the VLC network than those considered in Chapters 3 and 4, we consider using MA techniques in the VLC network. We start in **Chapter 5** with comparing numerically the most appropriate techniques identified in Chapter 2, i.e., orthogonal frequency-division multiple access (OFDMA) and power domain non-orthogonal multiple access (NOMA), before discussing the development of NOMA.

Based on the conclusions of Chapter 5, we develop in **Chapter 6** an interference mitigation solution for NOMA-based multi-cell VLC networks. In particular, ZF pre-coding is used for broadcasting the signals of the users who suffer from inter-cell interference (ICI), which is the interference arising from receiving signals from neighbouring cells, while transmitting the ZF pre-coding signal by each AP as the signal of a single NOMA user. The performance of the proposed hybrid NOMA-ZF pre-coding scheme is compared with that of conventional NOMA in terms of user achievable throughput and network fairness.

To handle a larger number of users that would suffer from ICI, while accounting for the dimming requirements in the VLC network, we propose in **Chapter 7** efficient scheduling and coordination of the NOMA transmission in each cell, with the goal of maximizing the achievable throughput and the network fairness. The performance of the proposed dimming-aware scheduling is compared with that of conventional NOMA over different dimming conditions.

To address the handover problem associated with considering MA techniques in multi-cell VLC networks, we propose in **Chapter 8** handover-aware scheduling solutions, for small/medium-scale and large-scale VLC networks, to improve the link reliability during user handovers, and the user achievable throughput. The performance of the proposed scheme is compared with that of non-scheduling based handover.

In **Chapter 9** we evaluate experimentally the performance of NOMA for VLC systems and show

the effect of varying NOMA parameters on the user performance.

Lastly, **Chapter 10** concludes the thesis, and discusses some perspectives for future work.

1.4.2 Author's contributions

The main contributions in this thesis can be summarized as follows:

- Performance optimization of UAV-based ZF pre-coded VLC networks, by optimizing the UAVs locations using PSO, to improve the achievable user throughput by decreasing the correlation in the network channel matrix.
- Performance optimization of ZF pre-coding in indoor VLC networks, by optimizing the FOVs of the Rxs using PSO, to reduce the correlation in the network channel matrix, and subsequently improve the network performance.
- Performance comparison of different MA techniques in large space VLC scenarios, elucidating the fact that NOMA offers the best performance in terms of total achievable throughput.
- Proposing an ICI mitigation solution for NOMA-based multi-cell VLC networks, by using ZF pre-coding to broadcast the signals of the users who suffer from ICI, while transmitting such signals as the signal of the user with the least decoding order in the NOMA transmission scheme of each AP.
- Proposing solutions which enable ICI mitigation in the NOMA-based multi-cell VLC networks, by efficient time-scheduling, scaling, and coordination of the APs' transmissions, while satisfying the dimming requirements.
- Proposing handover-aware scheduling solutions to achieve soft handovers, while improving the network throughput, for the cases of small/medium -scale and large-scale VLC networks.

Figure 1.4 summarizes the contributions of the thesis with respect to the VLC challenges.

1.4.3 Author's publications

1. M. W. Eltokhey, M. A. Khalighi, and Z. Ghassemlooy, "Multiple Access Techniques for Large Space Indoor Scenarios: A Comparative Study," in *International Conference on Telecommunications (ConTEL)*, July 2019, Graz, Austria.
2. M. W. Eltokhey, M. A. Khalighi, A. S. Ghazy, and S. Hranilovic, "Hybrid NOMA and ZF Pre-Coding Transmission for Multi-Cell VLC Networks," *IEEE Open Journal of the Communications Society*, vol. 1, pp. 513–526, 2020.
3. M. W. Eltokhey, M. A. Khalighi, and Z. Ghassemlooy, "Dimming-Aware Interference Mitigation for NOMA-Based Multi-Cell VLC Networks," *IEEE Communications Letters*, vol. 24, pp. 2541–2545, 2020.

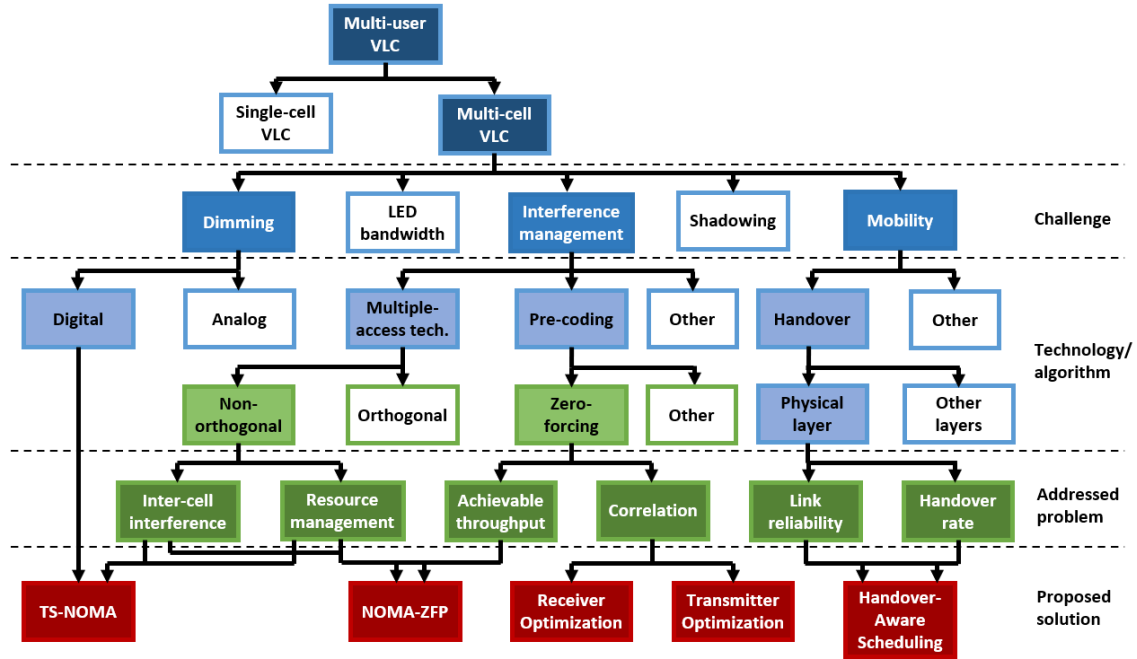


Figure 1.4 — Illustration of the contributions of the thesis with respect to the main challenges in VLC.

4. M. W. Eltokhey, M. A. Khalighi, and Z. Ghassemlooy, "Optimization of Receivers Field-of-Views in Multi-user VLC Networks: a Bio-inspired Approach," *IEEE Wireless Communications*, to appear.
5. M. W. Eltokhey, M. A. Khalighi, and Z. Ghassemlooy, "UAV Location Optimization in MISO ZF Pre-coded VLC Networks," *IEEE Wireless Communications Letters*, under revision.

Chapter 2

Multi-cell VLC Networks

Contents

| | | |
|------------|---|-----------|
| 2.1 | Introduction | 12 |
| 2.2 | VLC system | 13 |
| 2.2.1 | Tx | 13 |
| 2.2.2 | Rx | 13 |
| 2.2.3 | VLC channel | 14 |
| 2.2.3.1 | Rx noise | 14 |
| 2.2.3.2 | Channel gain | 14 |
| 2.2.4 | Signal modulation | 15 |
| 2.2.4.1 | DCO-OFDM | 16 |
| 2.2.5 | VLC uplink | 16 |
| 2.2.6 | Multi-cell VLC system | 17 |
| 2.3 | Interference mitigation in multi-cell VLC networks | 18 |
| 2.3.1 | Linear pre-coding | 18 |
| 2.3.1.1 | ZF pre-coding | 19 |
| 2.3.2 | MA techniques | 21 |
| 2.3.2.1 | TDMA | 21 |
| 2.3.2.2 | SDMA | 21 |
| 2.3.2.3 | O-CDMA | 22 |
| 2.3.2.4 | OFDMA | 22 |
| 2.3.2.5 | NOMA | 22 |
| 2.3.2.6 | Comparison of MA techniques | 23 |
| 2.4 | Optimization of VLC systems | 23 |
| 2.4.1 | PSO | 24 |
| 2.5 | Chapter summary | 26 |

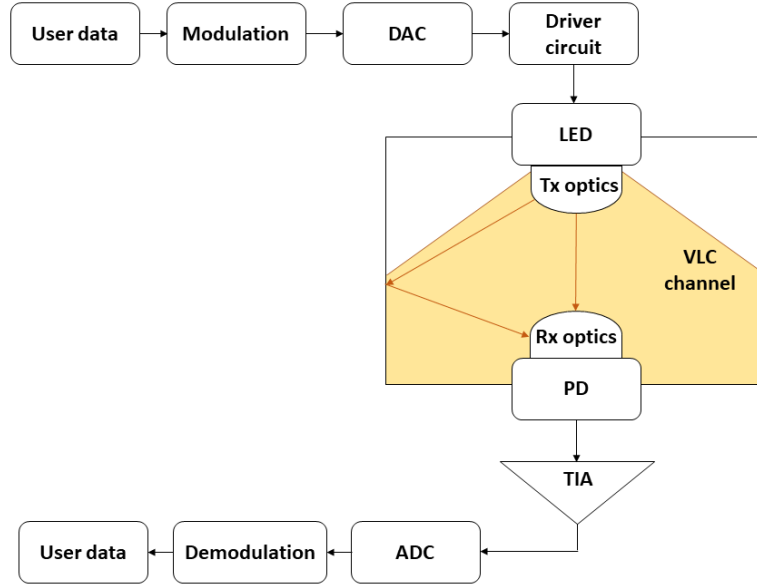


Figure 2.1 — Block diagram for the main components in the VLC system, highlighting the components at the Tx and the Rx, and the VLC channel.

2.1 Introduction

In typical VLC systems, the user data are processed before being forwarded to the LED luminaires used for lighting, which act as APs that serve the users within their illumination areas. At the user device, Rxs are used for signal reception and processing. The main building blocks for a typical VLC system are shown in Fig. 2.1. At the Tx, user data bits are modulated then converted to electrical analog signals using a digital-to-analog converter (DAC). The electrical signals are then used to modulate the LED's output light, using a driver. As the LED luminaires used for lighting are non-coherent sources, intensity modulation (IM) is commonly used, which requires the electrical signals to be positive and real. The modulated light signals then propagate through the channel, before being received at the Rx. According to the Rx architecture, a lens may be used to concentrate the received signal on the photodetector (PD). The PD generates a photo-current, which is passed to a transimpedance amplifier (TIA), then an analog-to-digital converter (ADC) is used to sample the signal. Following the demodulation of the signal, the user data are recovered.

In this chapter, we provide a brief introduction to the main components in the VLC system and the VLC channel, before discussing the signalling schemes and the configuration of the considered multi-cell VLC network. Following this, we discuss the main MU techniques considered for interference mitigation, and the optimization tools that can be used for improving the network performance. In Section 2.2, we explain the considered VLC system model, before discussing the MU techniques in Section 2.3, and the optimization of VLC systems in Section 2.4. Section 2.5 concludes the chapter.

2.2 VLC system

2.2.1 Tx

LED-based luminaires, which are considered as APs in VLC, are based on using diodes that convert electrical signals to light signals. They have been receiving an increasing interest, for their advantages in terms of energy and luminance efficiency compared to other types of luminaires (e.g., the incandescent and fluorescent -based lamps) [34]. Because of their relatively fast response, they have been considered for wireless communication applications, in addition to their illumination purposes. For VLC systems, the main types of LEDs used include RGB LEDs, and phosphor-based LEDs.

In RGB LEDs, red, green, and blue LED chips are used to generate the corresponding lighting, where by controlling and mixing the LED chips' outputs the overall illumination experience changes. By modulating each colour separately, RGB LEDs can achieve high capacity using wavelength-division multiplexing (WDM) [35–37]. On the other hand, given the balance needed between the red, green, and blue components for white lighting, the overall lighting experience is prone to changes due to components' colour deviation over time [34].

For the phosphor-based LEDs, which are commonly referred to as “white LEDs”, an ensemble of blue LED chips and yellow phosphor coating is utilized for an overall white lighting experience. Compared to RGB LEDs, white LEDs offer a simpler structure and a lower cost, which supports their widespread use. However, they suffer from slow response during signal modulation, because of the phosphor part, which results in limiting the modulation bandwidth to few MHz [10]. To boost the VLC link capacity, different solutions have been proposed, such as blue filtering at the Rxs [38], equalization [39], and using spectrally efficient modulation (e.g., multi-carrier modulation) schemes, such as optical orthogonal frequency-division multiplexing (OFDM) [40], which will be explained in more detail later in Subsection 2.2.4.

Note that, interest in other types of LEDs such as micro LEDs [41] and organic LEDs [42] has been increasing recently. However, for the rest of the thesis, we will consider the widely used white LEDs.

2.2.2 Rx

For signal detection at the Rxs, the main types of PDs used include the positive-intrinsic-negative (PIN) photodiodes, the avalanche photodiodes (APDs), and the silicon photo-multipliers (SiPMs), which are in fact arrays of APD pixels operating in Geiger mode [9, 43–45]. For the considered indoor and outdoor VLC systems, due to the relatively strong ambient light at the Rxs, and for Rx simplicity in the user device, we consider PIN PDs in the rest of the thesis. Note, these PDs are non-coherent detectors, thus the converted signal is independent of the phase of the light wave.

To increase the received optical intensity, optical concentrators can be considered at the Rx, to

increase the effective area of the PD, which will be further explained in Subsection 2.2.3.

2.2.3 VLC channel

Due to the physical properties of the VLC systems, which allow the transmission of positive and real signals, VLC signalling is based on IM and direct detection (IM/DD). The equivalent VLC link model is given by:

$$y(t) = h(t) \otimes x(t) + z(t), \quad (2.1)$$

where $x(t)$ and $y(t)$ denote the transmitted and the received photocurrents, respectively, \otimes is the convolution operation, $h(t)$ represents the channel gain, and $z(t)$ refers to the Rx noise.

2.2.3.1 Rx noise

The noise at PIN-based Rxs comprises mainly of shot and thermal noise. Shot noise is caused by the fluctuations of the photo-current at the Rx, which is generated by the incidence of the transmitted signals as well as any other ambient radiations, and its power is directly proportional with the strength of the incident radiation. In case of background radiations, shot noise can be dominant, which can be modelled as signal-independent additive white Gaussian noise (AWGN) with zero mean [9, 46]. As concerns the thermal noise, it results mainly from the Rx electronic circuits and dominates in case of negligible background radiation. Similar to shot noise, thermal noise is modelled as signal-independent AWGN with zero mean. The overall noise at the Rx is modelled by the summation of the variance of the AWGN shot and thermal noises, which can be given by $B \times N_0$, where B represents the system bandwidth and N_0 denotes the one-sided noise power spectral density.

2.2.3.2 Channel gain

VLC signals propagate in the communication environment following the physical properties of light. As a result, the received signal may result from LOS or non-LOS (NLOS) propagation components, where the latter results from the reflection of light signals by the reflecting surfaces within the environment. It has been shown in several works that, NLOS components have small contribution to the received signal compared with LOS component in VLC networks [47–50]. For this reason, we consider only LOS propagation in this thesis, assuming that the LOS component is not blocked or shadowed. For modelling the link between AP_{*i*}, and user *j* (U_j) utilizing a PIN PD and an optical concentrator, the channel gain is denoted by h_{ij} . Figure 2.2 shows the channel gain parameters for a typical LOS VLC link. Assuming a Lambertian pattern for the LED, the channel gain can be written as (see [10, 51–54]):

$$h_{ij} = R S \frac{(m+1) A_j}{2\pi l_{ij}^2} \cos^m(\phi_{ij}) \cos(\theta_{ij}), \quad (2.2)$$

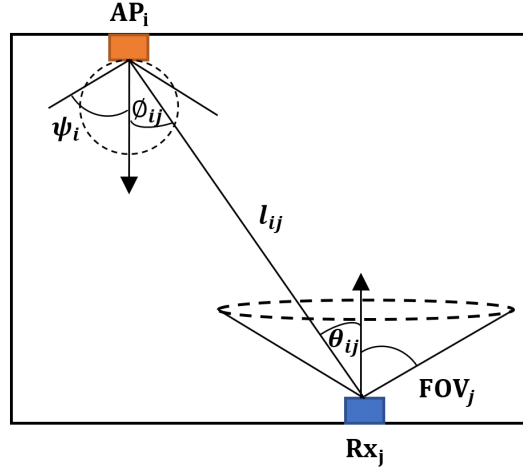


Figure 2.2 — Demonstration for LOS propagation between AP_i and Rx_j .

where ϕ_{ij} refers to the angle of emission with respect to AP_i , θ_{ij} refers to the incident angle with respect to U_j (j^{th} Rx, Rx_j), and l_{ij} denotes the link distance between AP_i and U_j . Also, R is the PD responsivity, assumed to be the same for all RxS, S is the LED conversion efficiency, and m is the Lambertian order, assumed to be the same for all LED luminaires. In addition, A_j is the j^{th} Rx collection area, which is given by [9]:

$$A_j = \frac{q_j^2}{\sin^2(\text{FOV}_j)} A_{PD_j}, \quad (2.3)$$

with A_{PD_j} denoting the Rx active photo-detection area, q_j the optical concentrator refractive index, and FOV_j the Rx FOV corresponding to Rx_j . The Lambertian order m is given by $m = -\ln(2)/\ln(\cos \psi_i)$ with ψ_i being the half-power angle of the LED-luminaire at AP_i . Note that $h_{ij} = 0$ for $\theta_{ij} > \text{FOV}_j$, where FOV_j is the FOV of Rx_j . If no concentrator is used at Rx_j , we have $A_j = A_{PD_j}$.

2.2.4 Signal modulation

Signal modulation techniques in VLC systems can be classified into serial transmission (usually called “single-carrier”) and multiple-subcarrier (usually called “multi-carrier”) schemes. Serial transmission techniques include on-off keying (OOK), pulse amplitude modulation (PAM), pulse position modulation (PPM), and pulse width modulation (PWM), which encode messages using two intensity levels, multiple intensity levels, position of the pulse in time-domain, and width of the transmitted pulse, respectively. Because of susceptibility of serial transmission techniques to inter-symbol interference due mainly to the limited modulation bandwidth of the white LEDs, multiple-subcarrier modulation techniques, such as multiband carrier-less amplitude and phase modulation (m-CAP) [55–59] and OFDM [60,61], are usually considered to provide high data rates. Generally, use of OFDM offers (i) efficiency in spectrum utilization; (ii) adaptability to the frequency selectivity of the channel through bit/power loading; and (iii) simplicity of channel equalization [40]. Note, since OFDM signals are complex and bipolar, they cannot be used directly in

VLC systems, which rely on IM/DD. To comply with the VLC signal requirements, various techniques have proposed to generate real unipolar OFDM signals, such as direct-current biased optical OFDM (DCO-OFDM), and asymmetrically clipped optical OFDM (ACO-OFDM) [61]. In DCO-OFDM, a DC bias is added to the signal before clipping to obtain a unipolar signal [62, 63]. For ACO-OFDM, only odd-numbered subcarriers are modulated before zero-level clipping, which does not result in any loss of information [64]. Given the advantage of DCO-OFDM in terms of spectral efficiency [65], it is assumed by default as the signalling scheme in the rest of the thesis.

2.2.4.1 DCO-OFDM

Figure 2.3 shows the block diagram for DCO-OFDM based transmission. At the Tx, firstly, information bits are mapped (typically using quadrature amplitude modulation (QAM) mapping), before serial to parallel (S/P) conversion. Then, such parallel stream passes by Hermitian symmetry to ensure having real-value signals, followed by an inverse fast Fourier transform (IFFT) block, to generate the time-domain signal. Note, every $\frac{N_c}{2} - 1$ symbols are grouped to form an OFDM symbol $\mathbf{X} = [X_0, X_1, \dots, X_{N_c}]$, where N_c is the number of OFDM subcarriers, X_k is the symbol transmitted on the k^{th} subcarrier, and the Hermitian symmetry is imposed on the OFDM symbol such that:

$$X_0 = X_{\frac{N_c}{2}} = 0, \quad (2.4)$$

$$X_k = X_{N_c-k}^*, \quad 0 < k < \frac{N_c}{2}. \quad (2.5)$$

Here, $(.)^*$ denotes complex conjugation. After passing the output of the IFFT block to parallel to serial (P/S) conversion, adding a cyclic prefix (CP), and performing DAC, a DC-bias is added to the signal in order to get a positive-value signal. Afterwards, double-sided clipping is applied on the signal to fit it to the dynamic range of the LED. The resulting signal is then used to modulate the LED intensity. After propagation through the channel, the received optical signals are converted to electrical signals by the PD, then filtered and amplified by the TIA, before undergoing ADC and removing the CP of each block. After S/P conversion, fast Fourier transform (FFT) is applied on the received blocks, then one-tap frequency domain equalization is applied to compensate the channel effect. Following this, P/S conversion and demapping are performed to recover the transmitted bits.

2.2.5 VLC uplink

Obviously, bidirectional transmission is needed for the considered wireless networks. Whereas VLC is considered as a promising solution for downlink (i.e., from the LED luminaire to a device), implementing the uplink could use IR or RF transmission. Note that, using VLC for uplink could result in unpleasant experience for users. A relatively recent approach considers using short light pulses for uplink, to ensure minimum impact on the user lighting experience, which is referred to as “DarkVLC” [66]. However, this results on limitations on the link performance in terms of the

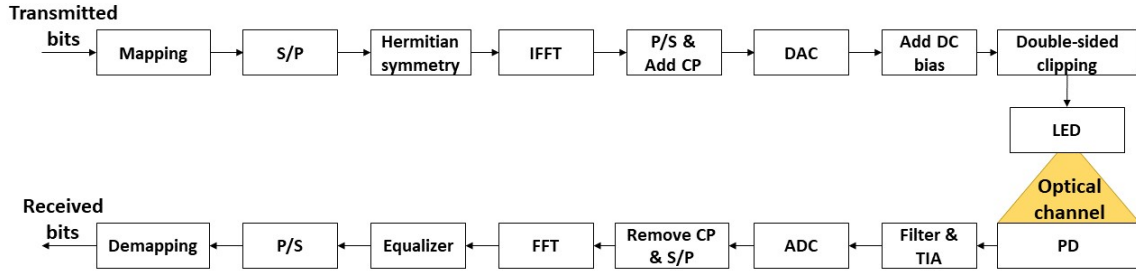


Figure 2.3 — A generalized block diagram for DCO-OFDM.

user achievable throughput. On the other hand, the use of RF signals (e.g., WiFi [67]) is not compatible with EMI-sensitive scenarios. As a result, the use of IR band for uplink has been considered as a reliable solution to make the balance between link performance, user lighting experience, and compatibility with EMI-sensitive scenarios [67]. To address MA requirements, in the uplink, carrier-sense MA with collision avoidance (CSMA/CA) protocol can be used in the MAC layer, as suggested in [68], given its advantage in terms of resource utilization efficiency by allowing users to access the channel according to their traffic, after checking the availability of the channel resources.

2.2.6 Multi-cell VLC system

For VLC systems, as the area of the illumination area increases, the number of LED luminaires required to satisfy the lighting and the communications needs increases. As mentioned earlier, such LEDs serve as APs, each one potentially handling several users in its coverage area (i.e., cell). This is the case, for example, for a relatively large office or a conference hall. Figure 2.4 illustrates the principle of such a multi-cell network. Therein, users are handled differently depending on whether they are located at “cell centers” or at “cell edges”. A central control unit connects the APs and has the task of information exchange and coordination between them. It also defines the cell boundaries, and consequently, specifies cell-center users (CCUs) and cell-edge users (CEUs). The APs, in turn, are responsible for identifying the channel information for all users, and forwarding it to the central control unit. In such a cellular scenario, there are two primary types of interference: the inter-user interference (IUI) resulting from the interference between the users within a cell, and the ICI resulting from the interference arising from the users in neighbouring cells. In particular, handling CEUs that are subject to intense ICI is a delicate task. In the next sections, different techniques for handling IUI and ICI will be discussed.

Note, the ensemble of TxS (APs) and RxS (users) can be regarded as either a MU multiple-input single-output (MU-MISO) or a MU multiple-input multiple-output (MU-MIMO) system, depending on using a single PD or multiple PDs per Rx, respectively. Throughout this thesis we consider a single PD at each Rx for the reason of reduced implementation complexity. Consequently, the MU-MISO architecture is considered in the sequel.

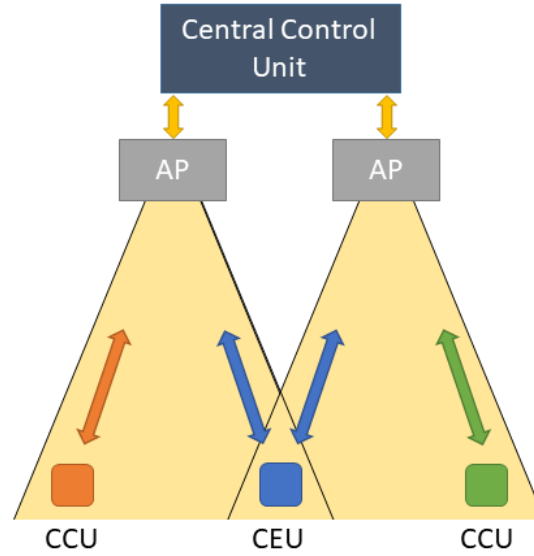


Figure 2.4 — Block diagram for the main components in the VLC system, highlighting the components at the Tx and the Rx, and the VLC channel.

2.3 Interference mitigation in multi-cell VLC networks

To handle multiple users in multi-cell VLC networks while mitigating IUI and ICI, two main approaches could be considered. The first is exploiting the spatial degrees of freedom at the Tx and the Rx (e.g., the Tx and the Rx locations), by using linear pre-coding techniques, to fully use the time and the frequency resources in the network. However, this comes at the expense of constraints on the number of users that can be handled, and increased complexity of the network. Higher flexibility on the number of users can be achieved by distributing the network resources (e.g., time, frequency) among the users using MA techniques, which come at the expense of a lower spectral efficiency.

2.3.1 Linear pre-coding

The idea of linear pre-coding is based on pre-processing the user data, based on the channel gain, to improve the user performance according to a pre-defined criterion. Indeed, this requires the availability of the user channel state information (CSI) at the Tx.

For the context of VLC, different pre-coding schemes have been proposed, such as those based on zero forcing (ZF) pre-coding [69–71] and mean-squared error (MSE) [50, 72, 73] criteria. For MU-MISO VLC systems, linear ZF pre-coding has been widely used, due to its simplicity, and its good performance at high signal-to-noise ratio (SNR) levels. This is mostly the case for indoor VLC networks because of the limited link distance in the case of existing LOS [74–77]. Due to the merits of ZF pre-coding, it is further considered in the following chapters.

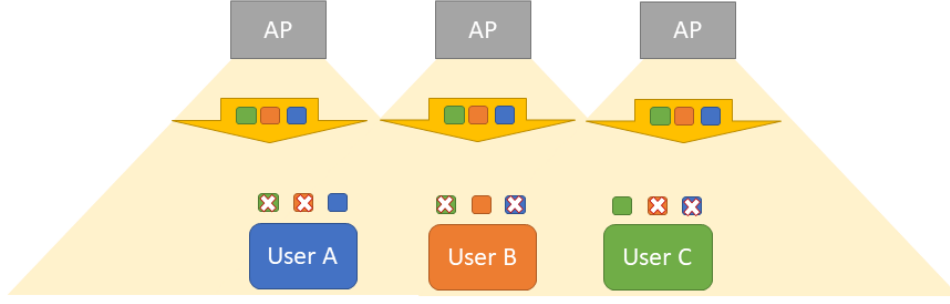


Figure 2.5 — An example of 3 Tx - 3 Rx VLC network, where ZF pre-coding is used for interference mitigation at each of the Rx.

2.3.1.1 ZF pre-coding

For the given MU-MISO network structure, linear ZF pre-coding is performed at the APs on the users' signals, which results in the suppression of interference from the other users at each Rx. To do this, the CSI of all underlying channels must be estimated at each Rx (for instance, based on the transmission of some pilot symbols from the APs in the downlink), and sent back to the APs (in the uplink). This CSI is then used by the APs to calculate the appropriate ZF pre-coding matrix [69]. Figure 2.5 shows a simplification for the idea of ZF pre-coding.

Let N_t denotes the number of APs, located at the VLC network, that handle a total number of N_r Rx within their coverage area, such that $N_r \leq N_t$. At AP_i , the Rx_j symbol d_j is multiplied by a pre-coding weight w_{ij} . Combining all weighted symbols for N_r users (excluding the DC bias), we obtain the transmitted signal x_i

$$x_i = \sum_{j=1}^{N_r} w_{ij} d_j. \quad (2.6)$$

The received signal at Rx_j after removing the DC offset is

$$r_j = \sum_{i=1}^{N_t} x_i h_{ij} + z_j, \quad (2.7)$$

where z_j is the Rx noise, considered as Gaussian distributed with variance σ_n^2 , which models the impact of ambient noise and the Rx pre-amplifier thermal noise. Define $\mathbf{d} = [d_1, \dots, d_{N_r}]$, $\mathbf{x} = [x_1, \dots, x_{N_t}]$, $\mathbf{r} = [r_1, \dots, r_{N_r}]$, $\mathbf{h}_j = [h_{1j}, \dots, h_{N_t j}]^T$, and $\mathbf{w}_j = [w_{1j}, \dots, w_{N_t j}]$. Equation (2.7) can then be rewritten as

$$r_j = \mathbf{h}_j^T \mathbf{x} + z_j = \mathbf{h}_j^T \mathbf{w}_j^T d_j + \sum_{k \neq j} \mathbf{h}_j^T \mathbf{w}_k^T d_k + z_j, \quad (2.8)$$

where $(\cdot)^T$ denotes transposition. In (2.8), the first term on the right side contains the desired signal and the second term refers to the interference from the other users. In matrix form,

$$\mathbf{r} = \mathbf{H} \mathbf{W} \mathbf{d} + \mathbf{z}, \quad (2.9)$$

where $\mathbf{H} = [\mathbf{h}_1^T, \dots, \mathbf{h}_{N_r}^T]^T$ and $\mathbf{W} = [\mathbf{w}_1^T, \dots, \mathbf{w}_{N_r}^T]$ denote the network channel matrix and the pre-coding weight matrix, respectively, both of dimension $(N_r \times N_t)$, and $\mathbf{z} = [z_1, \dots, z_{N_r}]$ is the noise

vector at the Rxs. Considering linear ZF pre-coding, we have [69]:

$$\mathbf{W} = \mathbf{H}^T (\mathbf{H} \mathbf{H}^T)^{-1} \text{diag}(\boldsymbol{\gamma}). \quad (2.10)$$

The diagonal entries $\gamma_j > 0$ (that can be considered as the coefficients of parallel sub-channels) determine the SNR at user Rx_j , and are determined based on a performance metric (e.g., throughput maximization, as considered in [69]). For simplicity, we consider the max-min fairness criterion proposed in [69], where the goal is to maximize the minimum achievable throughput. Let's define the vector $\boldsymbol{\mu}$ as:

$$\boldsymbol{\mu} = [\mu_1, \dots, \mu_{N_r}] = \left[\frac{\gamma_1}{\sigma_1}, \dots, \frac{\gamma_{N_r}}{\sigma_{N_r}} \right], \quad (2.11)$$

we have [69]:

$$\boldsymbol{\mu} = \mu^* \mathbf{1}, \quad (2.12)$$

$$\mu^* = \frac{\sqrt{P_e}}{\max(\mathbf{A} \mathbf{1})}, \quad (2.13)$$

where the matrix \mathbf{A} is:

$$\mathbf{A} = \text{abs}(\mathbf{H}^T (\mathbf{H} \mathbf{H}^T)^{-1}) \text{diag}(\boldsymbol{\sigma}), \quad (2.14)$$

with $\text{abs}(\cdot)$ denoting element-wise absolute value operation. Also, $\mathbf{1}$ in (2.12) is a vector with all entries equal to one and P_e is the transmit electrical power, assumed to be the same for all APs.

The SNR at Rx_j can be written as:

$$\text{SNR}_j = \frac{(\mathbf{h}_j^T \mathbf{w}_j^T)^2}{\sigma_n^2} = \frac{\gamma_j^2}{\sigma_n^2}. \quad (2.15)$$

Also, the maximum achievable throughput for Rx_j is:

$$R_j = \frac{B}{2} \log_2(1 + \text{SNR}_j) \quad (\text{bps}), \quad (2.16)$$

where the data rate is measured in units of bits per second (bps), and due to the Hermitian symmetry constraint in DCO-OFDM, we have a loss of factor two in the spectral efficiency [1].

Although ZF pre-coding offers an efficient solution for handling IUI and ICI, it limits the number of users. Indeed the number of users cannot exceed the number of APs. To allow handling a larger number of users, other MA scheme should be used, as discussed in the next subsection.

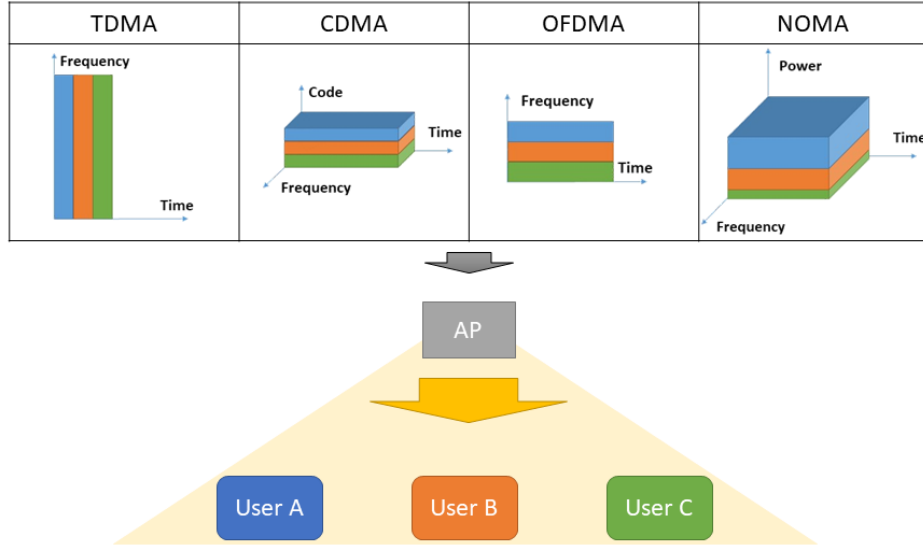


Figure 2.6 — Comparison between TDMA, CDMA, OFDMA, and NOMA techniques with respect to time, frequency, and power domains, for a 3-user example.

2.3.2 MA techniques

To serve a number of users larger than the number of APs, another approach for IUI and ICI mitigation in VLC networks is to use MA techniques. We present here different techniques, namely, time-division MA (TDMA), space-division MA (SDMA), optical code-division MA (O-CDMA), OFDMA, and power-domain NOMA (that we will simply refer to as “NOMA”), while discussing their suitability for a multi-cell VLC network with specific features including high data rate, large communication area, and user mobility. Figure 2.6 shows a comparison between different MA techniques with respect to the time, code, frequency, and power domains.

2.3.2.1 TDMA

By TDMA, the channel temporal resources are shared among users by allocating to each one a certain time slots [9, 78]. Although in indoor applications, we are concerned with a relatively low mobility of users, the accurate synchronization required at the user terminals and at the AP could become a challenge due to very high data-rates, especially for increased number of users. Also, in a multi-cell network, TDMA suffers from increased ICI at overlapping areas between the cells [79].

2.3.2.2 SDMA

SDMA basically consists in separating users in space domain, which could be realized using angle diversity transmitters (TxS) [79]. In RF systems, SDMA can be achieved using antenna arrays used for generating narrow beams pointing at users’ locations [79]. However, in VLC systems, this requires employing either special LEDs or using special optics with the off-the-shelf LEDs.

Therefore, from a practical point of view, SDMA is not well adapted to VLC networks in general. Nevertheless, it has been shown that combining TDMA and SDMA can result in a significant improvement in the network performance, compared with the simple TDMA approach [79].

2.3.2.3 O-CDMA

By O-CDMA, a unique code, also called signature sequences (SS) is attributed to each user, which is typically an optical orthogonal code (OOC) [80]. Users then use full time and spectral resources of the VLC channel. At the Rx, each user correlates the received signal with its specific code in order to (ideally) suppress the IUI. For this, the SS should be distinguishable from its shifted version as well as the shifted versions of other users' SS [81]. Note that random optical codes (ROCs) are simpler to generate than OOCs [82], but they provide a sub-optimal performance. In general, to handle a larger number of users, longer OOCs are needed, which impacts the achievable data rates and also increases the system complexity [83]. This can be a serious disadvantage for a relatively dense VLC network in a typical large-space scenario.

2.3.2.4 OFDMA

As explained earlier in this chapter, optical OFDM is a popular transmission technique to achieve high data-rates in VLC networks, overcoming the highly constrained modulation bandwidth of the LEDs [61, 84, 85]. Due to use of Hermitian symmetry in optical OFDM to obtain real signals, a spectral efficiency loss of factor 2 and 4 occurs for DCO-OFDM and ACO-OFDM schemes, respectively [62, 86]. OFDMA relies basically on using an OFDM-based transmission scheme, where the MA feature is obtained via sharing the spectral resources (i.e., groups of sub-carriers) between users.

For multi-cell scenarios, appropriate frequency reuse solutions can be used to decrease the network ICI [87]. For instance, fractional frequency reuse (FFR) has been proposed for DCO-OFDM-based systems in [87], which offers a good balance between the performance of CEUs, the average spectral efficiency, and low system complexity. Therein, two approaches of strict and soft FFR were considered. Strict FFR is based on dividing the available bandwidth to a common sub-band, used by CCUs, and a number of additional sub-bands, used by CEUs; these sub-bands are assigned so as to minimize the spatial reuse distance. For soft FFR, CCUs can use the sub-bands reserved to CEUs in the adjacent cells. In such a case, the performance of CEUs could degrade due to a higher interference level. To reduce this effect, more power is allocated to CEUs, compared with CCUs.

2.3.2.5 NOMA

By NOMA, multiplexing of users' signals is carried out at the AP using superposition coding, which allows the users to simultaneously use the whole temporal and spectral resources [47]. NOMA is

particularly interesting in VLC applications, compared, for example, to the context of RF cellular networks. Indeed, VLC networks likely have a small number of users per cell, benefit from relatively high SNRs, and typically experience slow channel variations due to the limited user mobility in indoor environments.

At the Rx side, users apply successive interference cancellation (SIC) to their received signal, to partially or fully remove the IUI from the other users (except for the first user in the decoding order), requiring hence the corresponding CSIs. At the AP, user signals are sorted based on their channel gains, so that users with lower channel gains are allocated a larger power. These latter decode their data first at the Rx side.

There has been an increasing interest in developing the performance of NOMA in VLC networks [88]. Several works proposed solutions for improving sum-rate in single-cell scenarios. In [89–91], power allocation (PA) schemes were proposed, which outperformed gain ratio power PA. Cuckoo Search (CS) optimization was used in [92] to optimize the VLC system parameters, including PA, with the objective of maximizing received power and achievable rate. In [93] joint power line communication (PLC) -VLC PA strategy was proposed to maximize the network sum-rate. Optimal user pairing followed by PA using majorization minimization was considered in [94] to maximize sum-rate for VLC scenario with steerable beams.

On the other hand, compared to single-cell scenarios, fewer works addressed NOMA problems in multi-cell VLC scenarios, which include, handling of IUI and ICI. In [95], overlapped clustering based on hybrid NOMA- orthogonal multiple access (OMA) were considered in layered asymmetrically clipped optical OFDM (LACO-OFDM) VLC networks, for minimizing interference. In [96] user assignment was handled for ICI mitigation, such that PA was optimized using gradient projection algorithm for sum-rate maximization. In [97] PA was optimized in multi-cell VLC networks, while offering flexibility in controlling the desired performance criteria.

2.3.2.6 Comparison of MA techniques

Following the above discussions, OFDMA and NOMA schemes are the most appropriate schemes for a high-rate large-space VLC network. Table I shows a brief comparison between the MA schemes presented above, considering the three main features of large-space scenarios, i.e., the ICI, the potential large number of users, and the requirement to high data rate. We have shown which scheme can support each of these features. We will later propose in Chapter 5 a more precise performance comparison between OFDMA and NOMA (Section 5.3).

2.4 Optimization of VLC systems

For VLC systems, to maximize the exploitation of time and frequency resources, real time adaptation of the system parameters (e.g., positions of the APs (considered in Chapter 3) or FOVs of the Rxs (considered in Chapter 4)) to the evolving communications environment is an impor-

Table 2.1 — Comparison between different MA techniques.

| | TDMA | SDMA | CDMA | OFDMA | NOMA |
|-----------------|------|------|------|-------|------|
| ICI | ✓ | ✓ | | ✓ | |
| Large no. users | | | | ✓ | ✓ |
| High data rate | | ✓ | | | ✓ |

tant point. Indeed, this can be considered as an optimization problem. In cases of large number of network parameters (to optimize), and consequently, the number of possible solutions, finding the optimal solution through a “parameter sweep” (i.e., trying all possible combinations of the parameters) can involve a huge computational complexity. Here, the use of artificial intelligence, especially, machine learning and deep learning algorithms, has been receiving increasing interest [98–101]. However, the particularity of VLC networks (e.g., LOS coverage at the Rx), may require re-training/adaptation of the optimization algorithms in response to minor changes in the network configuration. In addition, for networks with limited computational resources and/or requiring real-time adaptation to changes in the communications environment, more computationally-efficient algorithms are of higher applicability. To address this, metaheuristic algorithms offer an interesting and simple solution. By efficient exploration of the solution space, metaheuristic algorithms can make a good trade-off between the quality of solution and computational complexity [102, 103]. Although these algorithms do not need deep adaptation to each problem, fine-tuning is needed for the parameters that control the exploration of the solution space, in order to be tailored to the optimization problem [97, 103, 104]. One of the most efficient metaheuristic optimization techniques is particle swarm optimization (PSO). The interest in PSO has already been demonstrated in solving diverse problems in the area of optical wireless communications [97, 105–109]. Therefore, we will consider PSO in this thesis for the optimization of the VLC system parameters.

2.4.1 PSO

As mentioned above, PSO is a metaheuristic optimization technique, which mimics swarms movement [110]. In PSO, each point in a D -dimension search space (which involves all possible combinations of the values of the D variables to be optimized) is a solution; each particle moves between points to find the optimal solution. The direction and the speed of such movements in the solution space are decided by the best solution found by the particle itself (that we call personal best position, P_{best}), and by the ensemble of particles (that we call global best position, G_{best}). The quality of the solutions found by the particles are assessed using a fitness function, which is designed according to the optimization goals.

PSO can be well described by an example of a swarm of bees (particles) searching in a garden (solution space) for location with most flowers (optimal solution), over a certain time (iterations).

Bees communicate their experiences in terms of flower density at their locations to each other (i.e., $Pbest$ and $Gbest$), to decide the speed of movement in all possible directions (i.e., particles' velocities) in their next move. The flowers' density corresponds to how good the location is (i.e., solution quality), where higher flower densities correspond to better locations (i.e., better solutions). Figure 2.7 illustrates the PSO idea in a 2-variable solution space, where particles (represented by bees) wander the solution space formed by the axes of Variable 1 and Variable 2 to search the optimal solution. The axis of fitness value represents the evaluation of each possible solution using the fitness function, where larger fitness values represent better solutions. In Fig. 2.7(a) the particles are distributed in the entire solution space and exchange information about the $Pbest$ and $Gbest$, which illustrates the exploration of the solution space by the particles at the start of the optimization (i.e., first iterations). On the other hand, Fig. 2.7(b) shows the behaviour of the particles at the last iterations, where particles are about to converge to the optimal solution (i.e., solution with the largest fitness value).

For PSO algorithm, the considered parameters include the maximum number of iterations N_{it} , the number of particles N_p , and the number of variables D . For the q^{th} particle at iteration ℓ , the algorithm updates the following quantities:

- the position vector $\mathbf{p}_q = [p_{q1}, p_{q2}, \dots, p_{qD}]$,
- the velocity vector $\mathbf{v}_q = [v_{q1}, v_{q2}, \dots, v_{qD}]$, which represents the rate of change of the particles' positions in the solution space,
- and the personal best position vector $\mathbf{Pbest}_q = [pbest_{q1}, pbest_{q2}, \dots, pbest_{qD}]$.

In case where the fitness of the q^{th} particle is better than the fitness achieved by all other particles in the current/previous iterations, the global best position vector $\mathbf{Gbest} = [gbest_1, gbest_2, \dots, gbest_D]$ is updated by the particle's position. The new velocity of the q^{th} particle for the variable d at the iteration $\ell + 1$ is given by:

$$v_{qd}^{\ell+1} = \underbrace{w^\ell v_{qd}^\ell}_{(1)} + \underbrace{c_P^\ell \text{rand}_P (pbest_{qd} - p_{qd}^\ell)}_{(2)} + \underbrace{c_G^\ell \text{rand}_G (gbest_d - p_{qd}^\ell)}_{(3)}, \quad (2.17)$$

where the 1st, 2nd, and 3rd terms represent the contribution to the new velocity from the particle's old velocity, $Pbest$, and $Gbest$, respectively. Also, the new position of the q^{th} particle for variable d is given by:

$$p_{qd}^{\ell+1} = p_{qd}^\ell + v_{qd}^{\ell+1} \Delta t. \quad (2.18)$$

In (2.17), w^ℓ denotes the inertia weight, which controls the contribution of the old values of velocity on the new calculated velocity. Also, c_P^ℓ and c_G^ℓ refer to the weights that control the contributions of $Pbest$ and $Gbest$ on the new velocity, respectively, and rand_P and rand_G refer to random numbers ranged between 0 and 1. Also, in (2.18), Δt refers to time step, which is considered as unity. Without loss of generality, for preventing particles to move to locations outside the solution

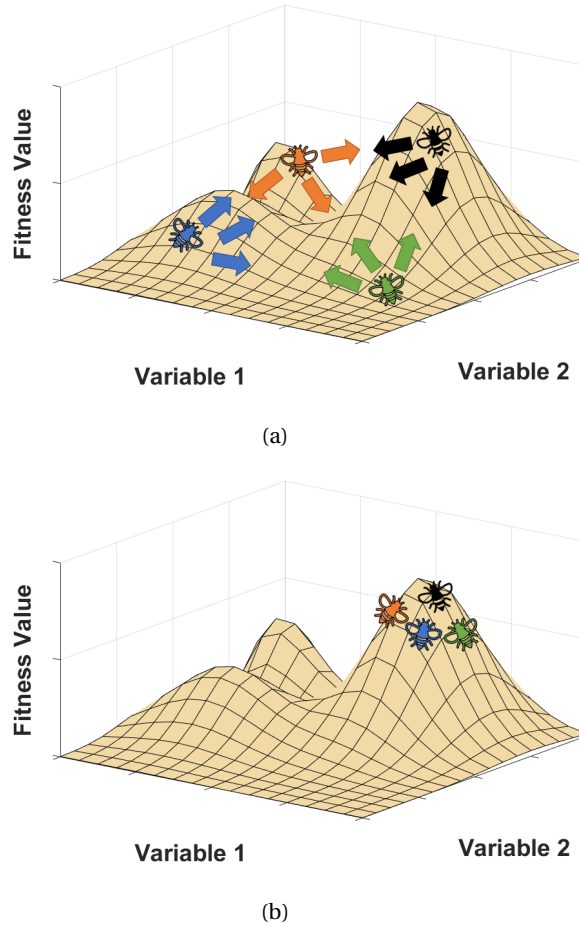


Figure 2.7 — Illustration for the PSO, where (a) represents the particles (represented by bees) at the first iterations while exploring the solution space and exchanging information about the personal best and global best positions and (b) represents the particles at the final iterations after converging to the optimal solution, that is represented by the largest fitness value. Note that the units of the axes depend on the variables being optimized.

space, we consider hard boundary conditions, where new positions (represented by new variable's values) exceeding the solution space are clipped in order to remain at the boundaries (maximum or minimum values).

2.5 Chapter summary

In this chapter we briefly introduced the main components of a VLC system, including the Tx, the Rx, and the optical wireless channel. We also discussed the signalling schemes and the presented multi-cell configuration considered. Following this, we explained and compared different MA interference mitigation solutions. Based on these discussions, we will consider ZF pre-coding for further development in Chapters 3 and 4, and will afterwards consider NOMA to allow handling relatively large number of users. Finally, as a computationally-efficient real-time optimization ap-

proach for VLC system parameters, we introduced the PSO algorithm.

Through the following subsequent chapters, we develop MA interference mitigation techniques for increasing the user density in the network.

Chapter 3

UAV Locations Optimization in MISO ZF Pre-coded VLC Networks

Contents

| | |
|---|-----------|
| 3.1 Introduction | 29 |
| 3.1.1 UAV-based BSs | 30 |
| 3.2 System model | 31 |
| 3.3 UAV locations optimization | 31 |
| 3.4 Performance analysis | 33 |
| 3.4.1 Performance over different optimization parameters | 35 |
| 3.4.2 Case study of UAVs with optimized and non-optimized locations | 36 |
| 3.4.3 Performance of optimized UAV locations in case of mobility | 38 |
| 3.5 Chapter summary | 38 |

3.1 Introduction

To develop MA interference mitigation solutions for multi-cell VLC networks, we start in this chapter by addressing the use of ZF pre-coding in UAV-based VLC networks in which the number of Rx is equal to the number of APs. We consider indoor industrial and outdoor scenarios, where UAVs are used as APs for the network in addition to providing illumination. Also we assume that the number of Rx is equal to the number of UAVs.

In fact, the growing use of LEDs for illumination in UAVs (i.e., drones) has opened up opportunities for VLC applications such as surveillance and monitoring, data collection from IoT devices, off-loading traffic data from base stations (BSs), and improving the quality-of-service (QoS) for users. Recently, the concept of Twinkle was proposed in [31], in which LEDs mounted on UAVs were used for illumination in urban areas. In addition, UAVs with LED-based lights have been reported for operation at night times [32].

3.1.1 UAV-based BSs

Use of UAVs as flying BSs to provide on-demand wireless communications offers a cost-effective and flexible solution [111]. However, RF-based transmission may result in interference for the ground networks, and may decrease the applicability of high-speed communications due to the limited energy [111]. To avoid such problems, VLC-based transmission is seen as a possible alternative, since it maximizes the resource utilization by using the existing LED-based lights. This combined feature of illumination and data communication is much favoured in search and rescue, delivery by drone at night, path illumination by UAVs in areas with no lighting, etc. [32], as well as in large space indoor industrial scenarios.

The use of VLC in UAV-based networks has been reported in literature [32, 111–117], where UAV locations optimization, for improving the system performance, has been receiving an increasing interest. In [112], UAVs were equipped with PDs and LEDs to act as relays in VLC-based vehicular communications, such that UAV locations were optimized to improve the link performance. In [113, 114] UAVs provided coverage to cars, where UAV locations were optimized for improved network throughput. For minimizing power consumption with respect to communication and illumination in UAV-based VLC network, optimization of UAV locations was carried out in [115]. In [32], the authors developed an algorithm for minimizing the power consumption of the UAVs, by optimizing the UAV locations and the users association. Further investigation of the problem in [32] was carried out in [111, 116] using deep learning. The work in [117] considered maximizing the sum-rate for NOMA UAV-based VLC networks, by optimizing the PA and the UAVs' placement.

It is noted that, in [32, 111, 113–117] each user was associated with only a single cell, which necessitates dealing with the handover and the cell-based IUI management. To avoid handovers while mitigating the IUI and ICI, use of MU-MISO ZF pre-coding is favoured, as explained in Chapter 2, as it has less constraints on the Rx architecture compared to the MIMO techniques, while offering simplicity, and improved performance at high SNRs [74–77]. However, linear ZF pre-coding performance is affected by the user locations, which impacts the correlation between the user channel gains. In fact, a high correlation results in a degradation in the network performance.

In this chapter, we propose decreasing the correlation in the network channel matrix for UAV-based MU-MISO ZF pre-coded VLC networks by means of location optimization of UAVs using PSO. To evaluate the network performance, optimization is carried out over random Rx positions, where the performance is compared with cases with non-optimized UAV locations. To relax the optimization requirements, we carry out tests to evaluate the impact of decreasing the rate of optimization on the network performance for different user mobility scenarios. Figure 3.1 illustrates the idea of improving the correlation in the network channel matrix by optimizing the UAV locations.

For the rest of the chapter, we present the system model in Section 3.2, the proposed optimization algorithm in Section 3.3, and the performance analysis in Section 3.4. The chapter is then concluded in Section 3.5.

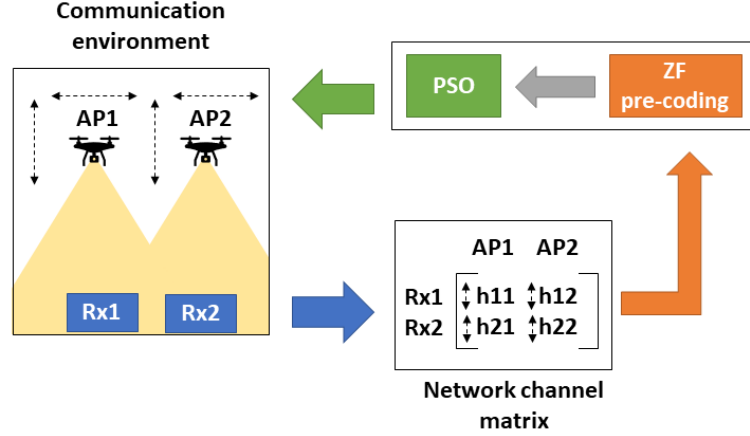


Figure 3.1 — Demonstration for the proposed optimization of UAV locations to improve correlation in the network channel matrix, where the changes of the UAV locations tune the channel gains in the network channel matrix for reduced correlation, which subsequently improves the performance of ZF pre-coding.

3.2 System model

We consider a UAV-based VLC system, see Fig. 3.2. Each UAV acts as AP where the LED-based APs mounted on UAVs provide illumination and a VLC downlink to the Rxs for data communication, and a central control unit, which is mounted on one of the UAVs, or located in a separate central UAV (not used for direct communications with the Rxs) exchanges information with the APs. In addition, the uplink, which uses IR transmission to the APs, as discussed in Chapter 2, is used for data transfer from the Rxs as well as sending the estimated CSI. This latter is used in determining the ZF pre-coding matrix, and in UAV location optimization, which are carried out in the central control unit, connected to the cellular network via RF or free-space optical links.

3.3 UAV locations optimization

The considered optimization problem targets decreasing the correlation in \mathbf{H} for maximization of the sum-rate given by:

$$\text{maximize} \quad \sum_{j=1}^{N_r} R_j. \quad (3.1)$$

For measuring the correlation in \mathbf{H} , the 2-norm condition number of \mathbf{H} , $\text{cond}(\mathbf{H})$, is considered, defined as the ratio of its largest to its smallest singular values, where decreasing the correlation is achieved by:

$$\text{minimize} \quad \text{cond}(\mathbf{H}). \quad (3.2)$$

The variables used for controlling the correlation are the UAV locations that directly impacts \mathbf{H} , which are optimized using PSO given the non-linearity and the non-concavity in the problem.

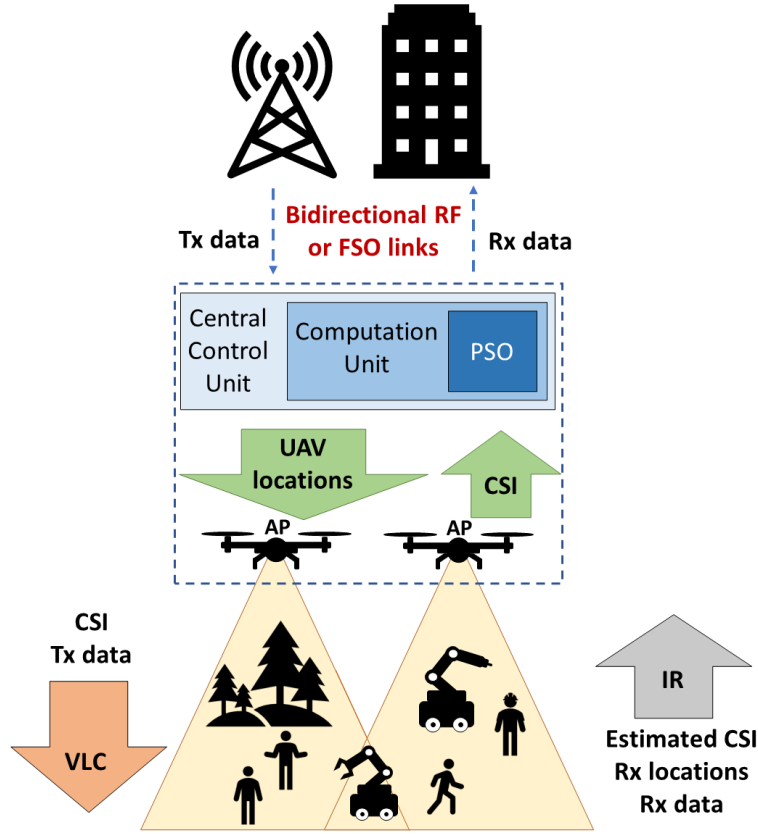


Figure 3.2—Illustration of the VLC system considered, highlighting the flow of information between a cellular network, a central control unit, UAV APs, and Rxs.

We explain in this part the proposed PSO-based UAV locations optimization as depicted in Fig. 3.3. As shown, first random positions and velocities for each particle are generated prior to evaluation of the performance of each particle. For the performance evaluation, the associated solution is converted from integer values to the UAV locations, which are used in the ZF pre-coding scenario. Following this, the sum-rate and the condition number for the corresponding network configuration are used to determine the fitness function for evaluating the solution quality. Based on the value of the fitness function, both $Pbest$ and $Gbest$ are updated followed by calculating the new position and velocity of the particle in the solution space. Following evaluation of each particle for all iterations, the $Gbest$ vector (i.e., the solution with the maximum fitness evaluation) represents the optimized UAV locations. To generalize the algorithm to cases where only discrete, and non-uniform separated UAV locations are considered (e.g., due to constraints on the accuracy of the localization available, or the communications environment), the possible UAV location values are converted to the integers, and the problem is considered as an integer programming problem. For such problems, the indices of UAV locations in the x and y coordinates are used in the solution space to ensure equal spacing between successive solutions in each coordinate.

Following this, the sum-rate and the condition number of \mathbf{H} for the corresponding network configuration are used to determine a fitness function F for evaluating the solution quality. Here

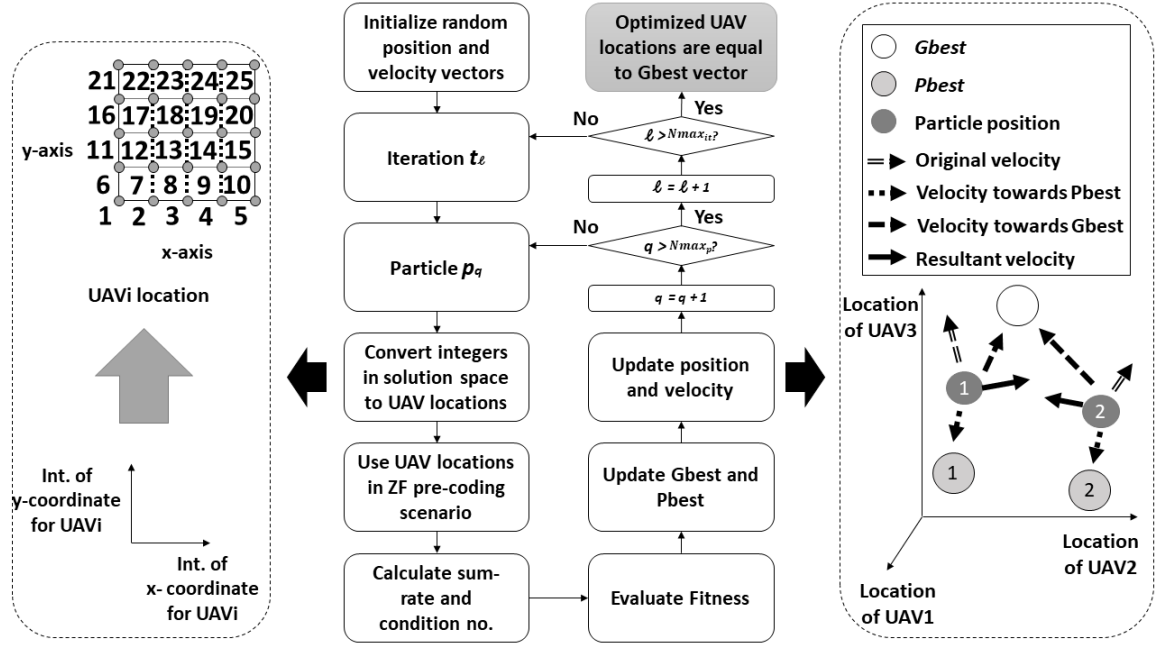


Figure 3.3 — Flow chart of the proposed algorithm for location optimization of three UAVs, where ℓ and q are the indices of the number of iterations and particles, respectively. The boxes on the left and right illustrate how UAV locations are converted to integers (Int.), and how two particles move in the solution space to find the optimal solution, respectively.

we propose the following fitness function:

$$F = F_1 \times \sum_{j=1}^{N_r} R_j - F_2 \times \text{cond}(\mathbf{H}) - (F_3 \times N_0), \quad (3.3)$$

where N_0 is the number of users with no LOS link with any AP. The 1st term promotes the solutions with higher sum-rates, the 2nd term downgrades the solutions that results in poor condition number in the network channel matrix, and the 3rd term ensures that the solutions with the users experiencing LOS blocking are avoided. Constants F_1 , F_2 , and F_3 control the contribution of the different terms. Based on the value of F , both $Pbest$ and $Gbest$ are updated, followed by calculating the new position and velocity of the particle in the solution space. After evaluating each particle for all iterations, the $Gbest$ vector (i.e., the solution with the maximum fitness evaluation) represent the optimized UAV locations.

3.4 Performance analysis

Here we compare the performance of the proposed system using both the optimized and non-optimized UAV locations in indoor industrial and outdoor scenarios. For the ZF pre-coding-based VLC network, we consider 4 LED-based APs, and 4 Rxs positioned at the height of 0.85 m above the floor level. No concentrators are considered at the Rxs side, and the channel gain values are given by equation (2.2). Each UAV has an AP, which ensures a real-time wireless transmission link

Table 3.1 — Simulation parameters.

| Parameter | Value |
|--|---|
| Transmit power per LED | 15.84 W |
| Room dimension | $(7 \text{ m} \times 7 \text{ m} \times 3 \text{ m}) \text{ m}^3$ |
| LED luminaire Lamertian order m | 1 |
| Number of LED chips per luminaire | 36 [72] |
| LED conversion efficiency S | 0.44 W/A [72] |
| PD responsivity R | 0.4 A/W [47] |
| PD area | 1 cm^2 [69] |
| Rx FOV | 62° [69] |
| Refractive index of optical concentrator | 1.5 [69] |
| System bandwidth B | 10 MHz |
| Equivalent Rx noise power spectral density | $10^{-21} \text{ A}^2/\text{Hz}$ [47] |

with the central control unit. In general, UAVs can be classified as either rotary-wing for hovering or fixed-wing for moving forward or staying aloft for a given time. In this work, we consider the rotary-wing UAVs. All the key system parameters adopted in the simulations are given in Table 3.1.

The sum-rate values corresponding to the 1st term in (3.3) are determined for 10 MHz bandwidth, whereas the 2-norm condition numbers, which corresponds to the 2nd term in (3.3), have reached orders of 10^3 for high condition number. Following the previous discussions at the end of last section, we have set F_1 , F_2 , and F_3 in (3.3) to 1, 10^5 , and 10^{10} , respectively to ensure that the 3rd term in (3.3) is the dominant term in case of LOS absence, while degrading the solutions with large 2-norm condition numbers. Note that, considering the heights of UAVs, it is highly unlikely that a Rx will experience a blind spot due to the LOS path being blocked. However, we have decided to include the 3rd term in (3.3) to guarantee the applicability of the proposed algorithm over wide range of UAV heights and communications scenarios. Figure 3.4 shows a top view for the considered communications environment, highlighting the possible locations for the 4 UAVs. Table 3.2 shows the parameters for both of the indoor industrial and the outdoor scenarios.

For PSO parameters in (2.17), w^ℓ is varied between 0.9 and 0.4 throughout the simulations [118]. To manage how particles search for the optimal solution in the solution space and benefit from their experiences, the weight c_p^l in (2.17) is decreased from 2.5 (at the start of optimization) to 0.5 (at the end) for better exploration of the solution space at the beginning by maximizing the reliance on $Pbest$. On the other hand, for $Gbest$, c_G^l is increased from 0.5 (at the start of optimization) to 2.5 (at the end) to enhance the convergence to the optimal solution [119].

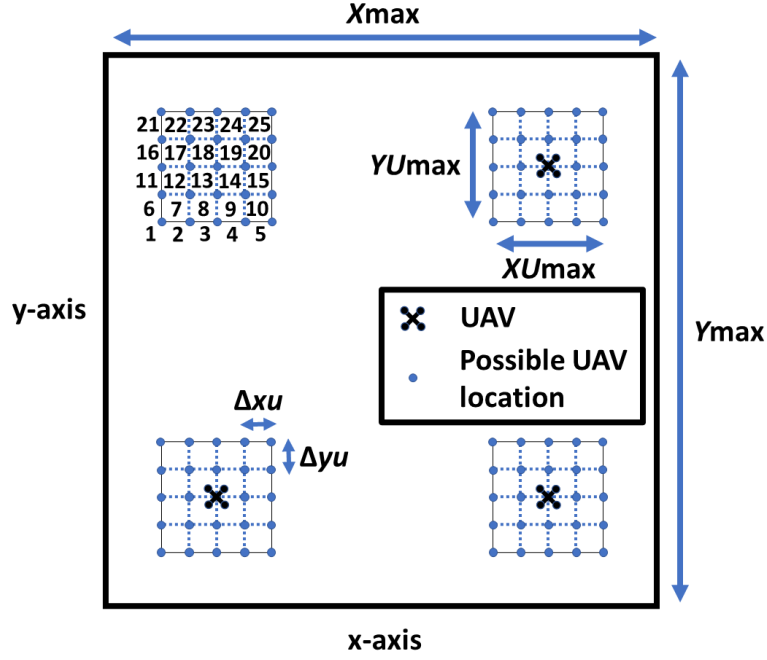


Figure 3.4 — Top view for the possible locations of the UAVs over the considered indoor industrial and outdoor scenarios.

Table 3.2 — Parameters of the indoor industrial and the outdoor scenarios.

| Parameter | Indoor industrial (m) | Outdoor (m) |
|--------------|-----------------------|-------------|
| X_{\max} | 10 | 20 |
| Y_{\max} | 10 | 20 |
| XU_{\max} | 2 | 4 |
| YU_{\max} | 2 | 4 |
| Δx_u | 0.5 | 1 |
| Δy_u | 0.5 | 1 |
| UAV height | 8 | 12 |

3.4.1 Performance over different optimization parameters

To find the best combinations of the numbers of particles and iterations for a given number of evaluations (i.e., $N_{\max_p} \times N_{\max_{it}}$), we compare in Fig. 3.5 the average sum-rate for different combinations of N_{\max_p} and $N_{\max_{it}}$, over 1000 random user positions, for both indoor and outdoor scenarios. As shown, the average sum-rate improves with increasing $N_{\max_p} \times N_{\max_{it}}$. For the same evaluations number, generally, higher average sum-rate is achieved for $N_{\max_p} > N_{\max_{it}}$, which is because of better exploration of the solution space prior to the converging to the optimal solution. Note that, lower sum-rates are achieved for the outdoor scenario since UAVs are considered with higher altitudes with the same transmit power as for the indoor case. Also, note

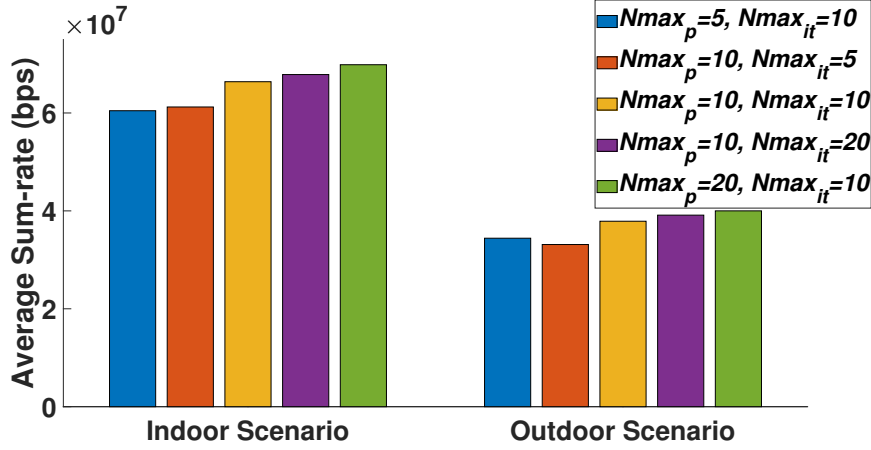


Figure 3.5 — Comparison between different pairs of particles (N_{max_p}) and iterations ($N_{max_{it}}$), over average sum-rate performance, for 4 Rxs 1000 random positions generated for indoor and outdoor scenarios.

that the required number of evaluations is much smaller than when evaluating all possible solutions (4 UAVs, with 25 possible locations each). Based on these results, we set $N_{max_p} = 20$ and $N_{max_{it}} = 10$ in the sequel.

3.4.2 Case study of UAVs with optimized and non-optimized locations

To highlight how the sum-rate performance vary throughout the proposed optimization, with the change of the UAV locations over the iterations, we consider in Fig. 3.6 the performance over a definite indoor industrial scenario, where the locations of the 4 Rxs in terms of (x, y) are (0.26, 4.63), (2.93, 3.55), (6.17, 3.18), and (7.54, 9.87). Figure 3.6(a) shows top view for the possible and the optimized UAV locations, and the Rx locations. Using (3.3), the evolution of the fitness function at each iteration is illustrated in Fig. 3.6(b). In the blue dotted-line boxes we have the UAVs' location indices, sum-rates, and condition number of \mathbf{H} , over every change in the fitness value (i.e., the most optimal performance achieved at that iteration). The red dotted-line boxes contain the performance for UAVs' position indices of (1,1); (9,1); (1,9); (9,9), (3,3); (11,3); (3,11); (11,11), and (5,5); (13,5); (5,13); (13,13) (i.e., the minimum, central, and maximum values possible for each of the UAV locations, respectively). As shown in Fig. 3.6(b), the increase in the iterations resulted in improving the solution quality, due to deeper exploration by the particles for the solution space. It is noted that for the considered scenario, PSO converges at iteration 5 to the optimal solution (optimized UAV locations).

Although a lower correlation in the network channel matrix results in higher sum-rate and an expected decrease in the 2-norm condition number (which corresponds to the ratio between the largest and the smallest singular values of the matrix), we note in the red boxes where sum-rates are 6.23×10^7 and 6.29×10^7 that the corresponding 2-norm condition numbers are 28.8810 and 29.8384, respectively. When calculating the 1-norm condition number for the same scenarios to

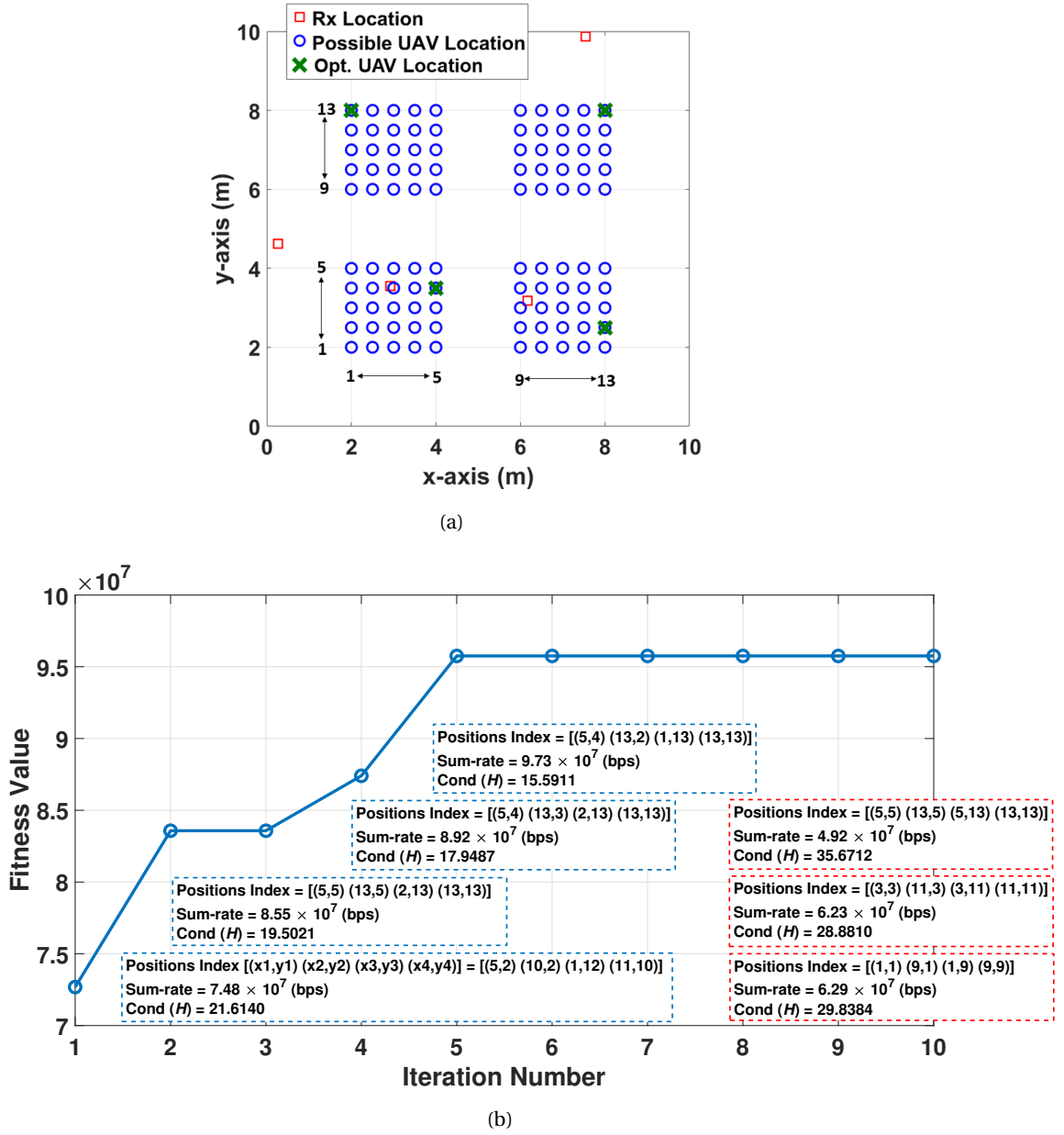


Figure 3.6 — Comparison between the optimized and the non-optimized UAV locations, where (a) presents a top view for the possible and the optimized locations of the UAVs, and the locations of the Rxs, and (b) illustrates the fitness value evolution over iterations. The blue and the red boxes provide the performance of the optimized and the non-optimized UAV locations, respectively.

verify the behaviour, the corresponding values for the former and the latter solutions are 42.9096 and 39.7116, respectively, reflecting the expected behaviour for the condition number. The unexpected behaviour for the 2-norm condition number could be linked to the reliance on the values of the largest and smallest singular values for the channel matrix. This shows the importance of including the sum-rate in addition to the 2-norm condition number in (3.3) while calculating

the fitness function for finding the optimal solution, to avoid problems due to such small fluctuations. It is worth mentioning that the obtained solution via PSO after convergence (sum rate of 0.973×10^8 bps) is quite close to the global optimal solution of 1.0×10^8 bps, obtained via parameter sweep (with considerably higher complexity).

3.4.3 Performance of optimized UAV locations in case of mobility

Although the evaluations considered in the proposed optimization are lower than those needed for parameter sweep, relaxation of the optimization requirements can lead to improved real-time adaptation to the user mobility. This can be achieved by decreasing the rate of optimization of the UAV locations with respect to the changes in the user positions. To this end, we compare the performance of using different rates for doing the optimization of UAV locations, with the case of non-optimized UAV locations, over different user mobilities.

Figure 3.7 shows a comparison of the average sum-rate for different mobilities, over indoor industrial and outdoor scenarios. For each mobility, 1000 users' positions are generated using the random way-point mobility model, where the time interval between each two successive positions is set to 0.5 s. Maximum velocities of 0.5, 1.4, 2, and 5 m/s are adopted for walking, fast walking, current and future industrial scenarios [120], respectively¹. Note, the optimization rates are 0.5, 1, 2, and 5 s, for a single, two, four and ten change in the positions, respectively. The results show an improved performance for the optimized UAV locations compared with the non-optimized locations for all cases, as expected. In addition, decreasing the optimization rate resulted in the performance degradation, which increased by increasing the mobility. This is because of higher variations in the user positions over the given time window, which results in faster deviation from the optimal configuration (i.e., optimized UAV locations for a given Rx locations). Note that, the differences in the sum-rates between the cases are due to the random positions. The lower sum-rates in Fig. 3.7(b) compared to Fig. 3.7(a) are due to the different heights of the UAVs with the same transmit power. It should be noted that, even at the highest mobility, updating the UAV positions at the lowest rate (i.e., every 5 s) for the optimized case offers improved performance compared with the non-optimized UAV locations, thus demonstrating the robustness of the proposed optimization.

3.5 Chapter summary

In this chapter, we proposed the optimization of the UAV locations using PSO, for MU-MISO ZF pre-coded UAV-based VLC networks. Firstly, we presented the trade-off between the quality of the solution and the number of evaluations considered, where the results showed that considering an adequate number of particles is important for sufficient exploration of the solution space. Follow-

¹We consider lower value for the maximum velocity in case future industrial, due to lower area in the indoor scenario considered.

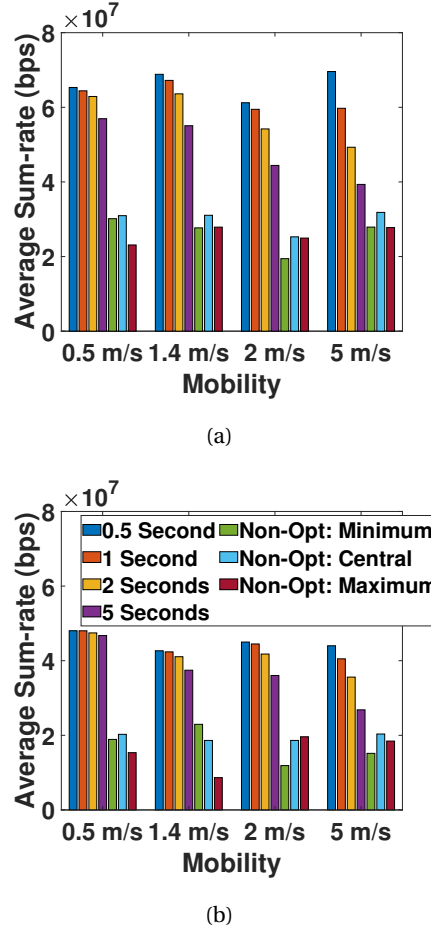


Figure 3.7 — Comparison between optimized and non-optimized UAV locations over average sum-rate performance for different user mobilities for (a) indoor industrial and (b) outdoor scenarios, considering different optimization update intervals.

ing this, we compared the performance of the optimized and the non-optimized UAV locations for a certain scenario, which illustrated the increase in the solution quality with the number of iterations, and highlighted the importance of carefully choosing the fitness function. Lastly, we compared the performance of the optimized and the non-optimized UAV locations over different mobility scenarios, where different rates for optimization were considered. Although decreasing the rate of optimization resulted in lower performance, due to higher deviation from the optimized configuration for the system, the proposed system offered improved performance compared to non-optimized UAV locations, illustrating the robustness of the proposed optimization, even for the use cases with limited computational resources and/or with high user mobilities.

Although the proposed optimization improved the sum-rate performance, however, the large area of the communications environment resulted in low user-density. In addition, using the privilege of optimizing the Tx locations (i.e., UAV locations) is not feasible for most of the VLC use cases in indoor scenarios. Starting from these points, we propose optimizing the ZF pre-coding performance in indoor VLC networks in the next chapter.

Chapter 4

Rx FOV Optimization in MISO ZF Pre-coded VLC Networks

Contents

| | |
|--|-----------|
| 4.1 Introduction | 41 |
| 4.2 System model | 43 |
| 4.3 FOV optimization | 43 |
| 4.4 Performance analysis | 47 |
| 4.4.1 Performance over different optimization parameters | 47 |
| 4.4.2 Case study of optimized and non-optimized FOVs | 49 |
| 4.4.3 Performance over random Rx locations | 49 |
| 4.4.4 Performance in the case of user mobility | 51 |
| 4.5 Chapter summary | 52 |

4.1 Introduction

Following the study presented in Chapter 3, we consider in this chapter relatively small indoor scenarios, e.g., a room or an office, where a small number of devices should be connected to the network. We again consider MISO ZF pre-coding for managing the MA. Here, to improve the network performance, we cannot use the same solution of Tx location optimization in Chapter 3, since the LED luminaires are fixed and usually installed following architectural and lighting constraints. Therefore, we propose to optimize the Rx parameters to improve the correlation in the network channel matrix.

The adaptation of Rxs parameters to reduce the correlation between users channel gains has already been proposed by several works. One approach is to use lenses along with imaging Rxs for separation of light images and hence improving correlation in the network channel matrix

[121, 122]. Improved correlation for imaging-based Rx's was reported in [49, 123] by using thin-lens, in [124] by using convex lens, in [121] by using hemispherical lens, and in [122] by using fisheye lens. However, the limitations of non-imaging Rx's on the FOV and the Rx size favours using non-imaging Rx's without lens as a relatively simpler solution [125].

For improved correlation performance in case of non-imaging based Rx's, the authors in [126] used line-blocked Rx (LBR) to block certain channel components at the PDs, and spatially separated Rx (SSR) to increase the separation between the PDs. Also, to reduce the channel gains due to incident radiation from specific paths, the orientation of PDs was varied using angle diversity Rx (ADR) in [127], whereas in [128] light signals from specific directions were guided by prisms to the PDs using prism array Rx (PAR). On the other hand, for controlling the increase and the decrease in the channel gains from certain directions, mirror diversity Rx (MDR) was proposed in [125, 129, 130], which separates the PDs by double sided mirrors that controlled the received signals to reduce correlation. Also, to reduce correlation, the use of mirrors along with ADR in mirror-aided angle diversity Rx (MADR) and optimization of PD orientation in variable receiving orientation angle (ROA) PD was considered in [131] and [132], respectively.

The effect of considering different FOVs at the Rx's on the correlation in the network channel matrix has also been studied in [70, 133, 134], where separation of signals from different channels was proposed in [133] using PDs with different FOVs, while [70, 134] studied the impact of varying the Rx's FOVs on the performance of MIMO pre-coded VLC systems. More specifically, [70] considered different FOVs for the PDs used by the same user to improve the BER performance. In [134], the effect of varying the FOV of one Rx on the correlation of users' channel gains was studied for a 2-user MIMO system, where increasing the FOV increased the correlation and led to a degradation of the BER performance. Recently, [135] proposed FOV tuning to achieve a range of discrete values, by controlling a mechanical iris placed at the top of the PD. Inspired by such works, we propose optimization of the FOVs to reduce the correlation in the network channel matrix.

In this chapter, we propose the tuning of FOVs of the Rx's in MU-MISO ZF pre-coding VLC systems to improve the network throughput performance, using PSO. For evaluating the network performance independent of users' locations, we apply the proposed algorithm to a 4-user system, over 1000 random users' positions and for different Rx's heights. By using a small number of PSO evaluations to optimize the FOVs, the proposed algorithm allows fast adaptation to the users' locations, to improve coverage and throughput performance. In addition, to manage the scenarios with user mobility that may require a fast adaptation of the Rx's FOVs to the position changes, we propose to use the last optimized FOVs for algorithm initialization, in order to allow a faster convergence to the optimal solutions. This approach is tested over scenarios generated based on the random way-point model for simulating the user mobility. Figure 4.1 illustrates the idea of reducing the correlation in the network channel matrix by optimization of the FOVs.

The rest of the chapter is organized as follows: Section 4.2 presents the system model, Section 4.3 introduces the proposed optimization algorithm, and Section 4.4 shows the numerical results. Finally Section 4.5 concludes the chapter.

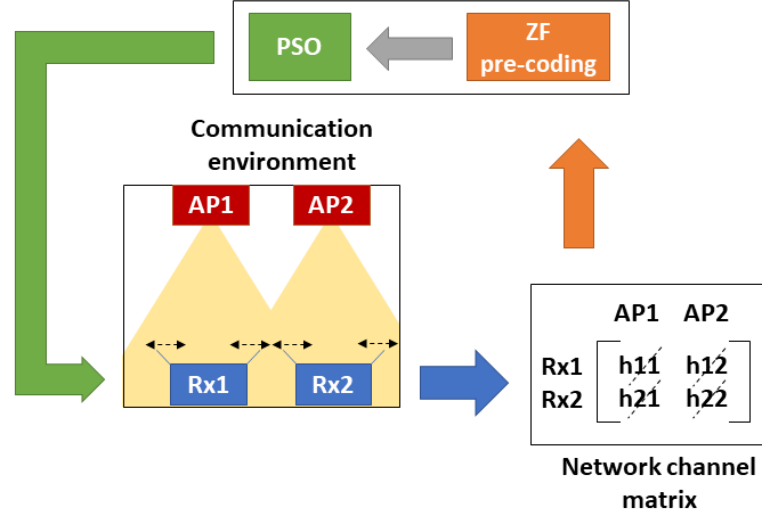


Figure 4.1 — Illustration of the proposed FOV optimization to reduce the correlation in the network channel matrix for the case of two APs and two Rxs. By tuning the FOVs, the entries of the network channel matrix are controlled.

4.2 System model

Figure 4.2 illustrates the considered system, where APs are connected to a central control unit for exchanging information (e.g., the CSI), handling the ZF pre-coding, as well as FOV optimization. To estimate the CSI at each Rx, pilot symbols are transmitted by the APs in the downlink. In the up-link, which is assumed to be realized by IR links as discussed in Chapter 2, the estimated CSI is sent back to the APs, which is used for calculating the ZF pre-coding matrix and for FOV optimization.

In order to manipulate a PD FOV, the design in [135] is considered, where a mechanical iris is mounted on the top of the plan of the PD surface, to vary the maximum angle of reception at the Rx. An illustration for the considered FOV tuning is presented in Fig. 4.3. For practical reasons, we assume that the FOV can be only tuned to discrete values, ranging between 10° and 80° , with a step of 5° .

4.3 FOV optimization

The considered optimization problem targets decreasing the correlation in \mathbf{H} for maximization of the sum-rate given by:

$$\text{maximize} \quad \sum_{j=1}^{N_r} R_j. \quad (4.1)$$

For measuring the correlation in \mathbf{H} , the 2-norm condition number of \mathbf{H} , $\text{cond}(\mathbf{H})$, is considered, where decreasing the correlation is achieved by:

$$\text{minimize} \quad \text{cond}(\mathbf{H}). \quad (4.2)$$

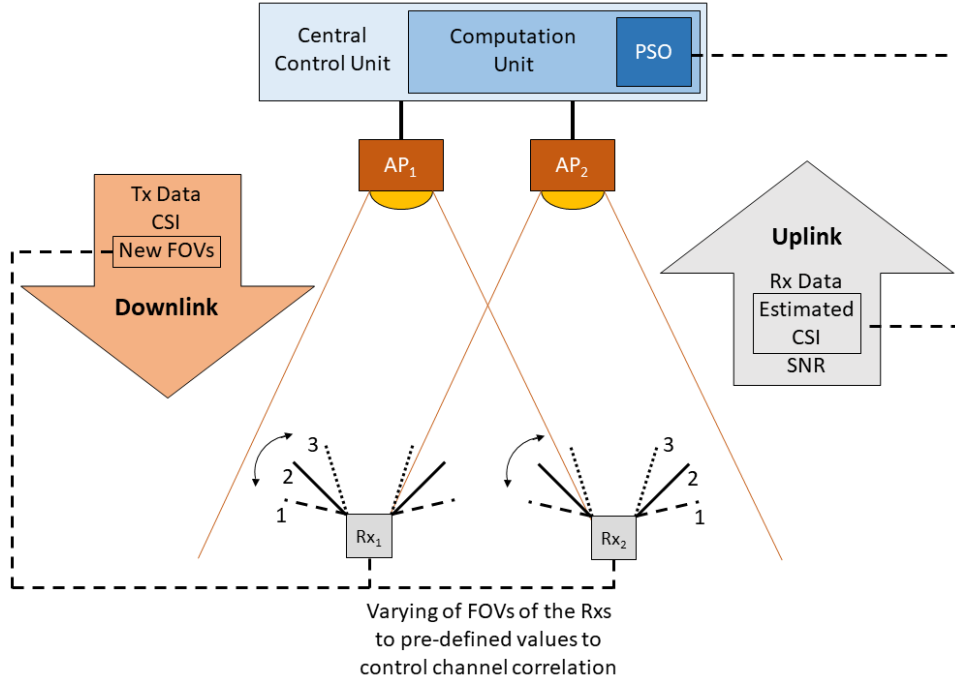


Figure 4.2—Illustration of the considered VLC network, highlighting FOV tuning that relies on the CSI of each Rx, which is estimated and transmitted via the uplink to the central control unit. The optimized FOVs' information is transmitted via the downlink to the Rxs.

The variables used for controlling the correlation are Rx FOVs that directly impacts \mathbf{H} , which are optimized using PSO given the non-linearity and the non-concavity featured in the problem.

Here we explain the proposed FOV tuning algorithm using PSO. As shown in Fig. 4.4, the algorithm starts with generating for each particle (possible solution) random positions (sets of FOVs) and velocities (rates of varying of the tested sets of FOVs in the solution space), prior to evaluating in each step (iteration) the performance of each particle (represented by a set of FOVs for all Rxs) and updating them. For evaluating the performance of a particle (i.e., the quality of the solution formed by a particular set of FOVs), the corresponding solution is converted from integer values to FOVs, which are forwarded to the Rxs in the downlink to apply them. Note that to generalize the proposed algorithm to cases where only discrete non-equally-separated FOV values are possible (e.g., $\text{FOVs} \in [10^\circ, 30^\circ, 40^\circ]$), the possible FOV values are converted to integer values, and the problem is solved as an integer programming problem. In particular, the indices of the FOVs (in ascending order of FOVs) are used as the values in the solution space, to ensure equal spacing between the possible FOVs. For FOV optimization, see Fig. 4.2, the central control unit transfers in the downlink (through the APs) the calculated FOVs by PSO to the Rxs. Following this, the channel gains achieved by the Rxs using such FOVs are sent back in the uplink to the central control unit (again, through the APs) to update the optimizer's evaluation for those FOVs using the fitness function. Based on these evaluations, PSO continues searching for new FOVs that achieve better performance by exploring possible better solutions (after updating positions and velocities of the

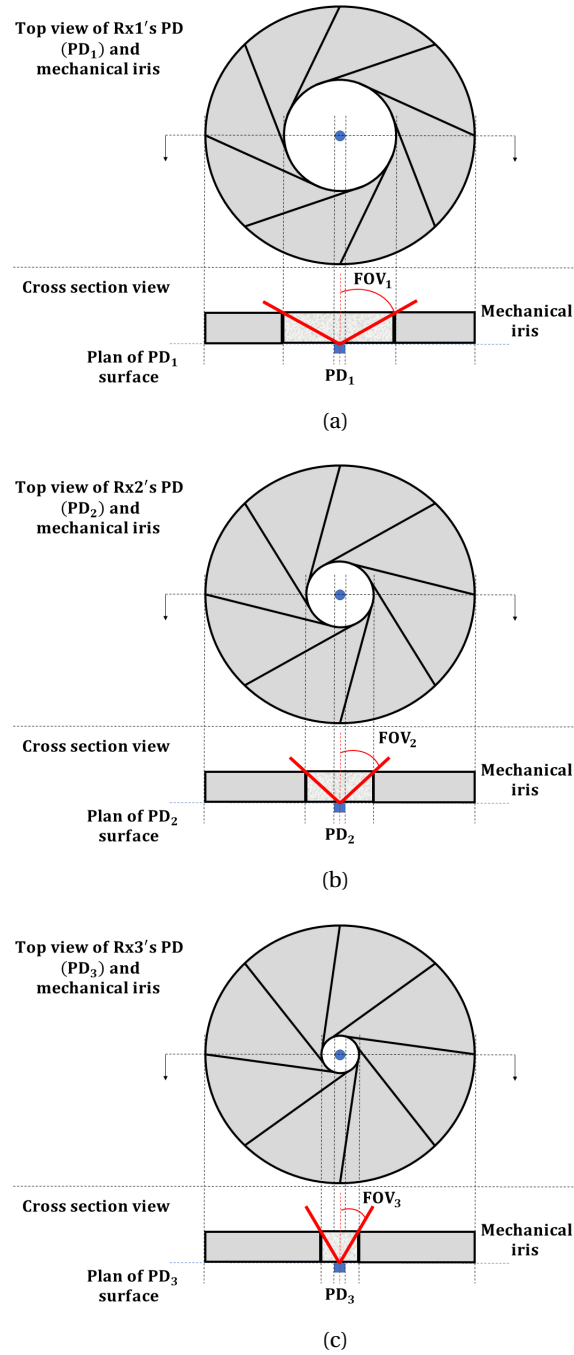


Figure 4.3 — An example of FOV tuning using mechanical iris for three Rxes, where the FOV value is (a) FOV_1 for Rx₁, (b) FOV_2 for Rx₂, and (c) FOV_3 for Rx₃, such that $FOV_1 > FOV_2 > FOV_3$.

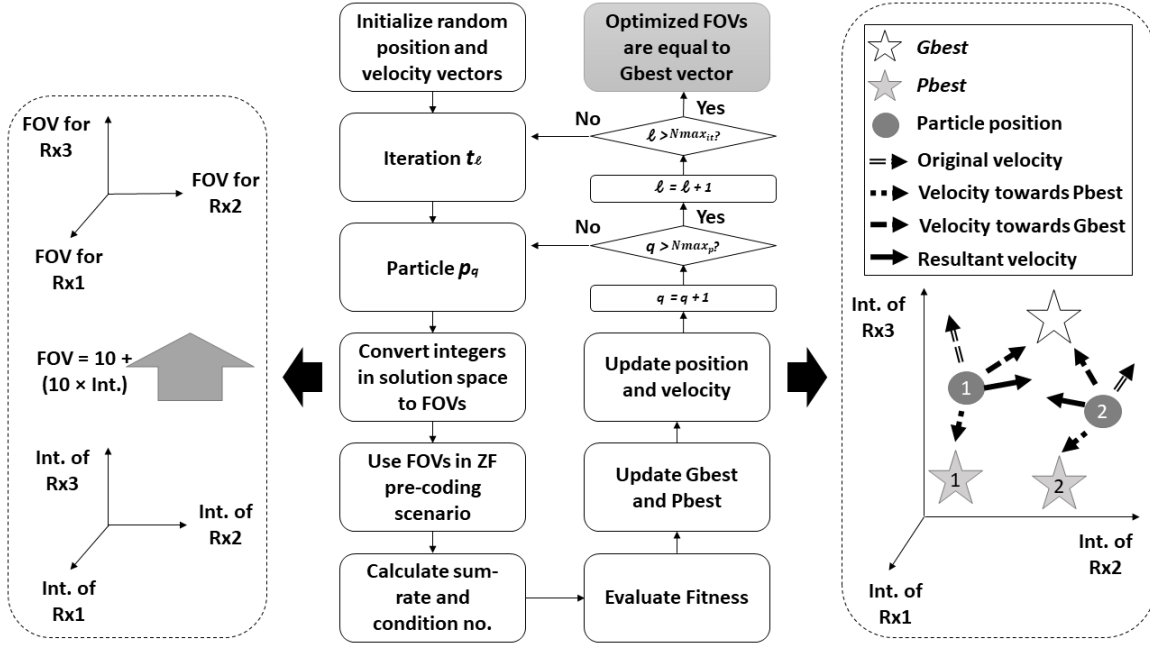


Figure 4.4— Illustration of the considered algorithm for an example of optimizing the FOVs of 3 Rxs in a ZF pre-coding scenario, where the indices ℓ and q refer to the iteration's number and the particle's number, respectively. “Int.” stands for integer. The dashed box at the left side shows how the variable values (FOVs) are extracted from integers during the optimization to solve the problem as integer programming problem, for a generalized solution in cases of having non-uniform steps between the possible FOVs. The dashed box at the right side illustrates an example of behaviour of 2 particles, under the influence of original velocity, $Pbest$, and $Gbest$.

particles), while relying on the experience of the system (after updating the $Pbest$ and $Gbest$). After evaluating all the particles over the maximum number of iterations, the global best position achieved (i.e., solution with maximum fitness evaluation) is considered as that corresponding to the optimized FOVs. Note that, the relatively low mobility in indoor VLC scenarios should allow such adaptation to channel time variations.

As stated previously, using the mechanical iris at the top of each PD, the FOV of each Rx is considered to be varied with a 5° step between 10° and 80° , thus resulting in 15 possible FOVs.¹ To evaluate the solution of PSO for our FOV tuning problem, we define a fitness function given by:

$$F_{FOV} = F_1 \times \sum_{j=1}^{N_r} R_j - F_2 \times \text{cond}(\mathbf{H}) - (F_3 \times N_0), \quad (4.3)$$

where N_0 is the number of users with no LOS component received from any AP, and F_1 , F_2 , and F_3 are the weights given to the 1st, 2nd, and 3rd terms, respectively. The 1st term ensures promoting solutions with higher sum-rates, which are calculated using equation (2.16), the 2nd term

¹Note that the speed of such variation of the FOV highly depends on the parameters of the mechanical iris, as well as the tools used for controlling it, which is beyond the scope of this optimization study.

downgrades solutions resulting in high condition number for network channel matrix, and the 3rd term guarantees that the solutions resulting in users with LOS blockage are excluded. This can be achieved by assigning F_3 a large value compared to the 1st and the 2nd terms, so that for any value of the sum-rate and condition number achieved by a solution, having a user with no LOS results in a bad evaluation of the solution (i.e., downgrading the considered fitness function). This point is explained in more detail in the next section.

4.4 Performance analysis

Here we present the numerical results of the comparison of the network performance when using non-optimized FOVs and optimized FOVs using PSO. We consider 4 Rxs in the VLC network, handled by ZF pre-coding, where concentrators are considered at the Rx side, and the channel gain of the LOS link between any AP and Rx is given by equation (2.2). Over 1000 random user positions are considered with different Rx heights, denoted by Z_{Rx} , but with the same orientation, i.e., all Rxs are pointing up to the ceiling. In each scenario, 4 LED luminaires (APs) are assumed, connected to the central control unit. Table 4.1 provides the simulation parameters considered.

The sum-rate values (corresponding to the 1st term in (4.3)) are calculated for a bandwidth of 10 MHz. Also, the 2-norm condition numbers in the considered random user positions (corresponding to the 2nd term in (4.3)) reached orders of 10^3 . Following the discussions at the end of the previous section, we hence set the constants F_1 , F_2 , and F_3 in (4.3) to 1, 10^5 , and 10^{10} , respectively, in order to guarantee that the 3rd term in (4.3) is always dominating, regardless of the values of the first two terms, while ensuring that the solutions with very large 2-norm condition numbers are downgraded. In addition, in cases of solutions with LOS blockage, we consider that sum-rates of such solutions (particles) are nullified, to be further downgraded.

For PSO parameters in (2.17), w^ℓ is varied between 0.9 and 0.4 throughout the simulations [118], while for a better management of particles in the solution space, c_p^l starts with the value of 2.5 and decreases to 0.5 at the end of iterations, whereas c_G^l is increased from 0.5 to reach 2.5. This ensures having (i) the maximum reliance on $Pbest$ at the start of optimization (for a better exploration of the search space); and (ii) the maximum reliance on $Gbest$ at the end of optimization (for a better convergence to the optimal solution) [119].

4.4.1 Performance over different optimization parameters

To choose the best combination of particles and iterations for a given total number of evaluations of $N_{max_p} \times N_{max_{it}}$, Table 4.2 compares the average network sum-rate and the number of LOS blockage cases for different values of N_{max_p} and $N_{max_{it}}$, for 1000 random user positions with random Rxs' heights Z_{Rx} between 0.85 m and 1.35 m. The 1000 random positions are picked from 1250 random positions, with random elevation and azimuth angles for the Rxs' within the range of $(0^\circ - 45^\circ)$ and $(0^\circ - 180^\circ)$, respectively, such that they guarantee LOS coverage at Rxs' FOVs of 80° .

Table 4.1 — Simulation parameters.

| Parameter | Value |
|--|---------------------------------------|
| Indoor environment dimension | $(7 \times 7 \times 3) \text{ m}^3$ |
| AP1 location (x, y, z) | (2.25, 2.25, 2.5) m |
| AP2 location (x, y, z) | (2.25, 4.75, 2.5) m |
| AP3 location (x, y, z) | (4.75, 2.25, 2.5) m |
| AP4 location (x, y, z) | (4.75, 4.75, 2.5) m |
| LED luminaire Lamertian order m | 1 |
| Number of LED chips per luminaire | 36 [72] |
| LED conversion efficiency S | 0.44 W/A [72] |
| PD responsivity R | 0.4 A/W [47] |
| PD area | 1 cm^2 [69] |
| Refractive index of optical concentrator | 1.5 [69] |
| System bandwidth B | 10 MHz |
| Equivalent Rx noise power spectral density | $10^{-21} \text{ A}^2/\text{Hz}$ [47] |

Table 4.2 — Comparison between different combinations of number of particles (N_{\max_p}) and iterations ($N_{\max_{it}}$) over average sum-rate and LOS blockage performance, for cases of random Rx heights in 4 Rx scenarios.

| Combination | Av. sum-rate (bps) $\times 10^7$ | LOS blockage |
|---------------------------------------|----------------------------------|--------------|
| $N_{\max_p} = 5, N_{\max_{it}} = 10$ | 4.19 | 25 |
| $N_{\max_p} = 10, N_{\max_{it}} = 5$ | 4.27 | 3 |
| $N_{\max_p} = 10, N_{\max_{it}} = 10$ | 4.42 | 2 |
| $N_{\max_p} = 10, N_{\max_{it}} = 20$ | 4.50 | 0 |
| $N_{\max_p} = 20, N_{\max_{it}} = 10$ | 4.60 | 0 |

This ensures the feasibility of using the proposed optimization in finding optimized solutions, given that each of the optimized FOVs has a maximum value of 80° . Note that, *LOS blockage* refers to the cases where one or more Rxs have no LOS path with any AP. Obviously, a lower LOS blockage indicates a better LOS coverage probability. Also, the sum-rate is averaged over all users' positions corresponding to LOS coverage occurrence.

Given the considered 15 possible FOVs for the Rxs, the number of evaluations required for a “parameter sweep” (i.e., trying all possible combinations of FOVs for finding optimum values, without using an optimization algorithm) for scenarios with 2, 3, and 4 Rxs, are 225, 3375, and 50625, respectively. Obviously, the considered numbers of evaluations $N_{\max_p} \times N_{\max_{it}}$ in Table 4.2 are much smaller than those needed for a parameter sweep.

As can be seen, increasing the number of evaluations from 50 to 100, and from 100 to 200, results in an improved performance in terms of average sum-rate and LOS blockage, as expected. In addition, it is noted from the cases with 50 or 200 evaluations that, having a larger number of particles than iterations (for the same number of evaluations) results in a better average sum-rate, and a lower LOS blockage (in case of 50 evaluations). This can be explained by the better exploration of the solution space before converging to the optimal solution.

4.4.2 Case study of optimized and non-optimized FOVs

To show in more detail how the FOVs and the sum-rate performance vary over iterations throughout the proposed optimization, we consider in Fig. 4.5 the performance of a certain scenario, where 4 Rxs with height of 0.85 m are located at (x, y) of (4.58, 0.32), (5.08, 4.03), (3.63, 5.47), and (1.49, 1.58). Figure 4.5(b) shows the fitness function calculated using (4.3) at each iteration. In the blue boxes, are indicated the FOVs, the sum-rates, and the condition numbers of \mathbf{H} at every change of the fitness value, representing the most optimal performance achieved at that iteration. Also, the red boxes indicate the sum-rates achieved in cases of fixed FOVs of 50° , 70° , and 90° . The plot shows an improvement in the quality of the solution due to the further exploration of the solution space, where PSO converges to the optimal solution at iteration 6.

We note from the data provided in the red boxes that decreasing the FOV in general should improve the performance, however, this remains dependent on the correlation of the network channel matrix. This can be verified from the slight decrease in the 2-norm condition number and the small increase in the network sum-rate by increasing the FOV from 70° to 90° . This elucidates the complexity of the problem, and the fact that the sum-rate performance is not always improved by simply decreasing the FOVs.

4.4.3 Performance over random Rx locations

Using the best combination of N_{\max_p} and $N_{\max_{it}}$ from Table 4.2 (i.e., $N_{\max_p} = 20$ and $N_{\max_{it}} = 10$), we compare in Table 4.3 the LOS blockage occurrence and the average sum-rate for the cases of non-optimized and optimized FOVs for 4 Rxs. Comparison is carried out over 1000 random scenarios. Non-optimized FOV values of 50° , 60° , 70° , 80° , and 90° are considered, however, the results of LOS blockage for FOVs of 80° and 90° were excluded from the table as all Rxs have LOS coverage over all scenarios. For the same reason of LOS blockage, the average sum-rate results for FOVs of 50° , 60° , and 70° were excluded.

It is observed that increasing the FOV decreases the risk of LOS blockage. However, in general, this comes at the expense of increased homogeneity between users' channel gains, thus a performance degradation due to higher probability of increased correlation in the network channel matrix (which is apparent only for the highly constrained case of random Rxs' orientations for the large FOVs of 80° and 90°). Also, considering random Rxs' orientations in addition to random Rxs' heights led to a degraded sum-rate performance, due to lower number of solutions that satisfy LOS

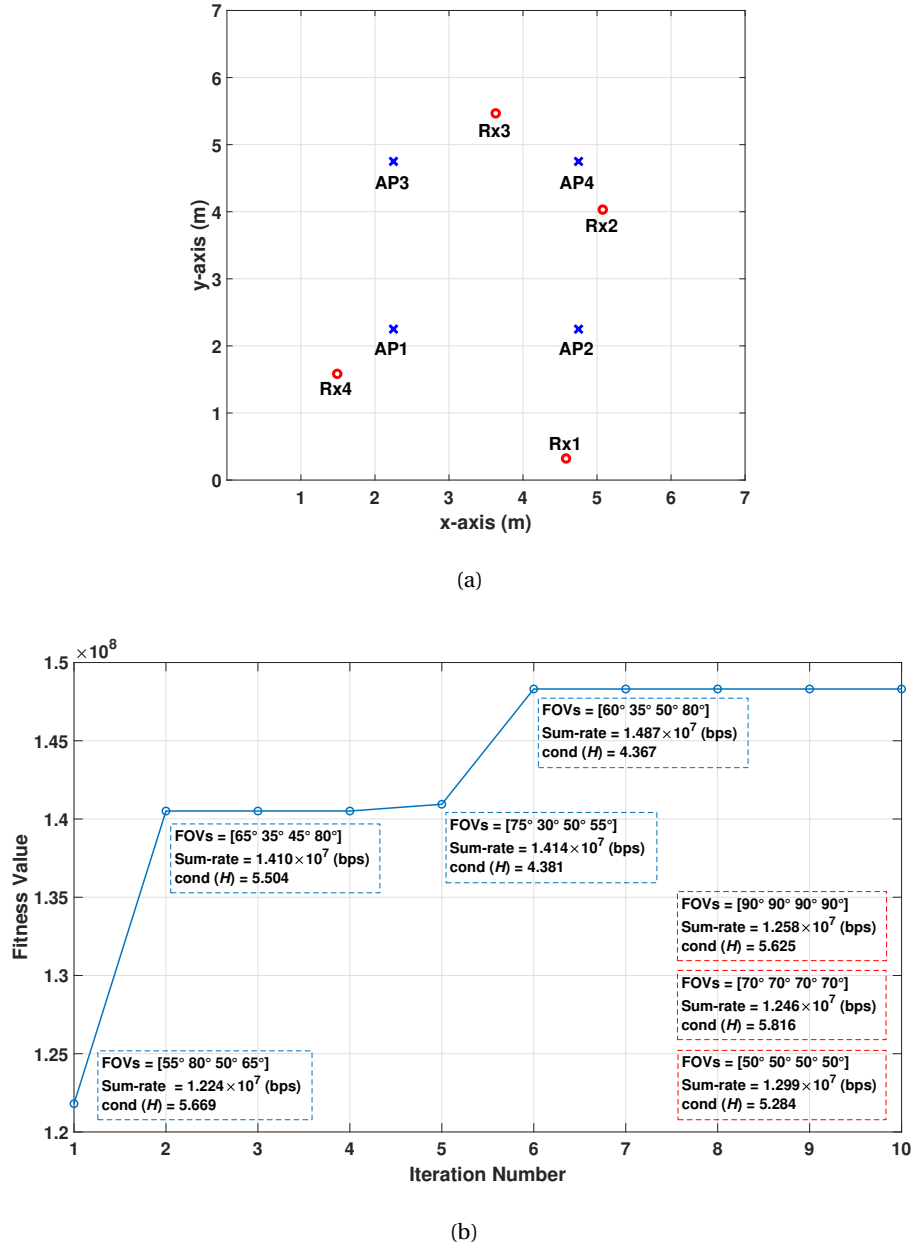


Figure 4.5 — Comparison between optimized and non-optimized FOVs for a 4 Rx - 4 AP scenario. (a): Top view for the locations of the Rxs and the APs with heights of 0.85 m and 2.5 m, respectively. (b): Fitness value versus optimization's iterations. The dashed blue boxes represent the optimized FOVs over changes in fitness and their corresponding sum-rates. The dashed red boxes correspond to the non-optimized FOVs (50°, 70°, and 90°).

Table 4.3 — Number of scenarios with at least 1 Rx with no LOS coverage and average sum-rate performance for optimized (Opt.) and non-optimized fixed FOVs, for fixed and random Z_{Rx} between 0.85 and 1.35 m, and random Rx's orientations.

| FOV | LOS blockage | | | |
|--------------------------------------|-------------------|-------------------|-----------------|---------------------|
| | $Z_{Rx} = 0.85$ m | $Z_{Rx} = 1.15$ m | Random Z_{Rx} | Random orientations |
| 50° | 668 | 873 | 840 | 786 |
| 60° | 30 | 268 | 257 | 491 |
| 70° | 0 | 0 | 0 | 194 |
| Opt. | 0 | 0 | 0 | 15 |
| Average sum-rate (bps) $\times 10^7$ | | | | |
| 80° | 3.24 | 3.06 | 3.10 | 3.06 |
| 90° | 3.24 | 3.06 | 3.10 | 2.88 |
| Opt. | 5.18 | 4.50 | 4.60 | 4.46 |

coverage. Moreover, increasing the Rx's height (i.e., decreasing the path length between the Tx and the Rx) increases the probability of LOS blockage, due to the decrease in the area covered on the AP plane by the Rx's FOV. On the other hand, irrespective of the considered Rx's heights, the proposed FOV optimization shows a robust performance, with very limited LOS blockage occurrence. It is worth mentioning that, even by decreasing the number of evaluations to 50 (see Table 4.2), the achieved performance with PSO was still better than the cases with non-optimized FOVs.

Similar observations can be made by considering the network average sum-rate, where the proposed approach outperforms the case of non-optimized FOVs. This advantage results from the adaptation of every Rx to users' positions to decrease the correlation in the network channel matrix. Increasing the Rx's heights results in an average sum-rate degradation, because of higher correlation between users' channel gains, as a result of shorter transmission path lengths.

4.4.4 Performance in the case of user mobility

To further decrease the number of evaluations in the case of changing users' positions, we propose to forward the most recent optimized FOVs as initial positions for PSO, for a faster convergence. To prevent particles from converging to sub-optimal solutions because of insufficient exploration of the solution space, we propose to vary these initial values by a random factor between 0 and 50% for each particle, in order to increase the spread of the particles in the solution space. We refer to this approach as “memory-assisted” optimization. The efficiency of this approach was investigated on 1000 scenarios generated by the random way-point model, simulating the mobility of 4 Rx's with velocities varying between 0.1 and 0.5 m/sec, and a time interval of 5 sec between two successive positions. The comparison is carried out over Rx's heights of 0.85 m and 1.15 m, and for

Table 4.4 — LOS blockage and average sum-rate performance for different cases of optimized and non-optimized FOVs for 1000 generated positions of 4 Rxs reflecting user mobility according to random way-point model.

| Z_{Rx} | Non-optimized | Memory-assisted PSO ($N_{max_p} = 10$) | | Conventional PSO ($N_{max_p} = 10$) | |
|--------------------------------------|---------------|--|---------------------|---------------------------------------|---------------------|
| | FOV = 80° | $N_{max_{it}} = 5$ | $N_{max_{it}} = 10$ | $N_{max_{it}} = 5$ | $N_{max_{it}} = 10$ |
| LOS blockage | | | | | |
| 0.85 m | 0 | 0 | 0 | 1 | 0 |
| 1.15 m | 0 | 0 | 0 | 3 | 2 |
| Average sum-rate (bps) $\times 10^7$ | | | | | |
| 0.85 m | 2.92 | 4.20 | 4.36 | 4.43 | 4.58 |
| 1.15 m | 2.76 | 3.74 | 3.86 | 3.84 | 3.97 |

different numbers of particles and iterations. Table 4.4 shows a comparison of the average sum-rate and the LOS blockage performance between the cases of conventional and memory-assisted PSO-based FOVs' optimization, as well as the case of fixed FOV of 80°. This latter corresponds to the best performance for non-optimized FOVs, as seen in Table 4.3. The results show a quite robust LOS blockage performance for the memory-assisted approach, compared with the conventional optimization. As before, for the case of conventional optimization, LOS blockage occurrence improves with increasing the number of evaluations from 50 to 100 or by decreasing the Rxs' heights. For the average sum-rate, both conventional and memory-assisted optimizations outperform the non-optimized case, while decreasing the Rxs' heights or increasing the number of evaluations results in an improved performance. However, we notice that the conventional optimization provides a better average sum-rate performance, which can be explained by a more constrained exploration of the solution space in the case of memory-assisted optimization. Indeed, the initial values are not distributed over the entire solution space as it is the case for conventional optimization.

4.5 Chapter summary

In this chapter, we proposed the optimization of the Rxs' FOVs based on PSO, for MU-MISO ZF pre-coding VLC systems. Firstly, we highlighted the trade-off between the solution quality and the number of evaluations and showed that using a sufficient number of particles is essential for an adequate exploration of the solution space. In general, for the non-optimized FOVs, decreasing the FOV improves the average sum-rate, but it also increases the risk of LOS blockage. The proposed FOV-tuning offers the best trade-off between decreasing the FOV for a better throughput performance, and increasing the FOV for a robust LOS coverage and outperforms the

non-optimized FOV approach in terms of both LOS blockage and average sum-rate performance. Lastly, we compared the performance of optimized and non-optimized FOVs for the case of user mobility, where it was shown that by using the last optimized FOVs as initial values for the PSO, a better LOS blockage performance is achieved using a smaller number of evaluations, compared with conventional optimization. However, this comes at the expense of a slightly lower average sum-rate, due to the constrained exploration of the solution space. Nevertheless, the robust performance achieved with a limited number of evaluations, makes this approach suitable for the cases of limited computational resources or relatively high user mobilities. For scenarios with still more constrained computational resources, the optimization of FOVs can be carried out only in cases where channel correlation exceeds a certain threshold.

Although the proposed FOV optimization improved the ZF pre-coding performance in VLC networks, the number of users handled cannot exceed the number of APs. To handle a larger number of users, we consider rather classical approach of MA techniques. In the next chapter, we first investigate the suitability of OFDMA and NOMA schemes for handling a potentially large number of users with high data rate, as discussed in Chapter 2.

Chapter 5

Performance Comparison Between OFDMA and NOMA

Contents

| | |
|---------------------------------------|-----------|
| 5.1 Introduction | 55 |
| 5.2 Performance analysis | 56 |
| 5.2.1 OFDMA-based signal transmission | 56 |
| 5.2.2 NOMA-based signal transmission | 56 |
| 5.3 Performance comparison | 59 |
| 5.4 Chapter summary | 63 |

5.1 Introduction

To handle interference in case of higher user densities than those considered in Chapters 3 and 4, i.e., when the number of user devices exceeds the number of APs, we consider the use of MA techniques. As we concluded in Chapter 2 that OFDMA and NOMA have the potential to handle a large number of users with high data rate demands, we compare in this chapter the performance of OFDMA and NOMA over different multi-cell scenarios. Note that, comparative studies of OFDMA and OFDM-based NOMA were presented in [47, 136] for the case of single-cell scenarios, where the advantage of the latter scheme in terms of network throughput was demonstrated, in particular, for increased number of users.

In this chapter, we start by providing analysis for both of OFDMA and NOMA schemes in Section 5.2, before comparing their performance over different scenarios in Section 5.3. Showing the advantages of NOMA over OFDMA, we further discuss some developments on the design of NOMA based VLC networks, before concluding the chapter in Section 5.4.

5.2 Performance analysis

5.2.1 OFDMA-based signal transmission

In OFDMA, the spectrum resources (i.e., subcarriers) are shared between the OFDM-modulated user signals. For ICI mitigation, resource management using either of *strict* or *soft* FFR can be considered, as explained in Chapter 2.

In order to compare with NOMA, we consider OFDMA with strict FFR resource management, where we determine the bandwidth allocation to CCUs and CEUs based on the ratio of the number of CCUs to the total number of users, that we denote by Υ , i.e.,

$$\Upsilon = \frac{\text{No. of CCUs}}{\text{No. of CCUs} + \text{No. of CEUs}}. \quad (5.1)$$

Then, the allocated bandwidth to CCUs is [87]:

$$\text{BW}_{\text{CCU}} = \Upsilon B, \quad (5.2)$$

Note that a different approach was proposed in [87], where a certain non-overlapped area of the total cell coverage area is considered to include CEUs (instead of considering CEUs in the intersecting areas between cells).

Based on (5.2), and assuming the use of an optical concentrator at the Rx, we calculate the channel gain using (2.2). Then, assuming each AP allocates equal power to the corresponding users, the signal-to-interference-plus-noise ratio (SINR) for Rx_j is given by:

$$\text{SINR}_{\text{OFDMA}_j} = \frac{(h_{ij} \sqrt{P_e K_j})^2}{\sigma_j^2}, \quad (5.3)$$

where K_j denotes the percentage of power allocated to Rx_j , and σ_j^2 stands for the noise variance at Rx_j . Denoting the allocated bandwidth to Rx_j by B_j , and assuming DCO-OFDM signalling, the maximum achievable rate for Rx_j is then:

$$R_{\text{OFDMA}_j} = \frac{B_j}{2} \log_2(1 + \text{SINR}_{\text{OFDMA}_j}). \quad (5.4)$$

5.2.2 NOMA-based signal transmission

As explained in Subsection 2.3.2.5, NOMA is based on multiplexing users' signals in the power domain at the Tx using superposition coding [137]. At the Rx side, SIC is performed for signal detection in order to mitigate the interference arising from the other users' signals [136]. An important point is that, in order to provide a homogeneous level of performance to all users, regardless of their corresponding channel gains, PA among users should be done carefully. For this, at the AP, users are ranked based on their channel gains, and their signals are assigned adequate PA weights accordingly; i.e., users with lower channel gains are allocated a higher power. At the Rx, users with

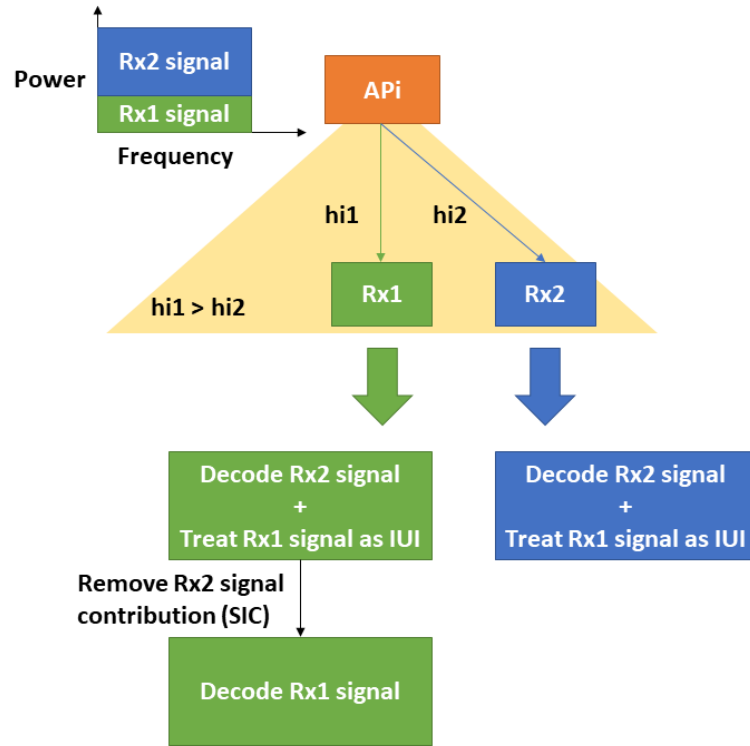


Figure 5.1 — NOMA signal transmission using superposition coding and reception using SIC in a 2-user example.

lower channel gains decode their data before the others. Initially, SIC is performed to (ideally) cancel the interference from already-detected signals (i.e., users with lower channel gains). The corresponding user's signal is then detected while considering the other remaining undesired signals as interference. To perform SIC, the CSI of the corresponding users is required. Note, for CSI estimation at each Rx, pilot symbols are transmitted in the downlink by the APs. In the uplink, the Rxs send back the estimated CSI to the APs, which can be realized by IR links as discussed in Chapter 2, Subsection 2.2.5. Figure 5.1 shows an illustration of transmitting and receiving NOMA signal in cell with 2 users. Considering AP_i as Tx and assuming perfect CSI knowledge at all users, the received signal at U_j is given by [138]:

$$r_{ij} = a_{ij} \sqrt{P_e} h_{ij} d_j + \sum_{k=1}^{j-1} a_{ik} \sqrt{P_e} h_{ij} d_k + \sum_{k=j+1}^{N_r} a_{ik} \sqrt{P_e} h_{ij} d_k + z_j, \quad (5.5)$$

where a_{ij} denotes the PA weight used by AP_i for U_j . The first term in (5.5) represents the desired signal for U_j , the second term denotes the interference that could be (ideally) removed using SIC (for $k < j$), and the third term represents the residual interference after SIC (for $k > j$). For the first

user, the detection is done directly. For the succeeding users, SIC detection is performed before signal detection using the CSI of the preceding users.

The performance of NOMA depends in particular on the PA to different users at the AP, which has been investigated in the recent literature. Though other PA scheme have been proposed recently which aim to maximize total throughput, such as the gain ratio PA proposed in [138], here due to its low complexity, a static PA approach is considered which consists in sorting users based on their channel gains and then assigning them power by considering a certain PA coefficient, regardless of the actual channel gains [139]. Using static PA for AP_{*i*} and *U_j*, we have:

$$a_{ij}^2 = \alpha a_{i,j-1}^2, \quad (5.6)$$

where α is the PA factor, representing the ratio between the allocated power to a given user and that to the preceding one in the decoding order. Clearly, $\sum_{j=1}^{N_r} a_{ij}^2 = 1$, to ensure a fixed normalized electrical transmit power [47]. With this formulation, the SINR for *U_j* is given by:

$$\text{SINR}_{\text{NOMA},U_j} = \frac{h_{ij}^2 P_e a_{ij}^2}{I_{\text{ICI}} + h_{ij}^2 P_e \sum_{k>j} a_{kj}^2 + \sigma_n^2}, \quad (5.7)$$

where I_{ICI} denotes interference due to ICI. Following the consideration of optical concentrator at the Rx, the channel gain h_{ij} is calculated using (2.2). The upper bound on the achieved rate for *U_j* is then calculated as follows [136]:

$$R_{\text{NOMA},U_j} = \frac{B}{2} \log_2 (1 + \text{SINR}_{\text{NOMA},U_j}) \quad (\text{bps}), \quad (5.8)$$

where the assumption of DCO-OFDM signaling is made.

To assess NOMA performance with respect to ICI, two NOMA schemes can be considered, which differ in the way of associating CEUs to the APs, inspired by [95].

In the first scheme, denoted NOMA-A, CEUs are associated with all APs that cover its location, while implicitly assuming that each CEU can separate the signals sent from the different associated APs (see [95]). Ideally, this results in less interference for CEUs, since they can use SIC to decrease the interference arising from the signals received from the different APs. However, this comes at the expense of increased network complexity since each CEU may require the CSI of other users in the corresponding cells (depending on the decoding order). In addition, this increases the user density for the APs [95].

In the second scheme, denoted NOMA-B, each CEU is associated with only the AP that corresponds to the strongest channel gain. This results in decreased cell density at the APs and decreased network complexity because CEUs will need the CSI of users of only one cell. However, CEUs in NOMA-B suffer from increased interference, as compared to NOMA-A, arising from the received signals of the other APs [95].

With a higher complexity compared with NOMA-B, NOMA-A mostly offers improved performance in terms of fairness. In the following comparison, NOMA-B is considered, and is referred to as NOMA for simplicity.

Table 5.1 — Simulation parameters.

| Parameter | Value |
|--|---|
| Indoor environment dimension | $(14 \text{ m} \times 14 \text{ m} \times 3 \text{ m}) \text{ m}^3$ |
| AP1 location (x, y, z) | $(4.5, 4.5, 2.5) \text{ m}$ |
| AP2 location (x, y, z) | $(4.5, 9.5, 2.5) \text{ m}$ |
| AP3 location (x, y, z) | $(9.5, 4.5, 2.5) \text{ m}$ |
| AP4 location (x, y, z) | $(9.5, 9.5, 2.5) \text{ m}$ |
| Current per LED luminaire | 7.2 A |
| Rx FOV | 90 deg. |
| Lamertian order of LED m | 1 |
| LED conversion efficiency S | 0.44 W/A [72] |
| PD responsivity R | 0.4 A/W [47] |
| PD area | 1 cm^2 [69] |
| Rx FOV | 90° |
| Refractive index of optical concentrator | 1.5 [69] |
| System bandwidth B | 10 MHz |
| Equivalent Rx noise power spectral density | $10^{-21} \text{ A}^2/\text{Hz}$ [47] |
| PA coefficient α | 0.3 |

5.3 Performance comparison

In the considered scenarios, an LED luminaire serving as AP handles the Rxs in its cell. A central control unit connects the APs, and is responsible for exchanging the channel information of all users between APs, classifying users into CEUs or CCUs according to the channel information, and determining the bandwidth allocated to each user. For both OFDMA and NOMA schemes, CEUs are associated with the AP from which they receive the strongest signal; this way, the signals of other APs are considered as interference. This results in penalizing CEUs in the NOMA approach due to SINR degradation. By OFDMA, however, CEUs do not suffer from ICI, because the interfering signals are received on different frequency bands and, furthermore, every CEU is associated with the AP corresponding to the highest channel gain. Table 5.1 summarizes the simulation parameters that we consider. Notice that we have assumed the maximum FOV of 90° as we consider a large room dimension with only 4 APs, so that Rxs can have a LOS link with the AP at any location inside a cell. For a larger number of APs, i.e., reduced cell size, a smaller FOV can be used.

Figure 5.2 shows the three considered scenarios with increased complexity from Scenario 1 to 3. Scenario 1 is composed of 4 CCUs and 4 CEUs such that each AP has 1 CCU and 2 CEUs in its coverage area. For Scenario 2, with a total of 12 users, we consider 8 CCUs and 4 CEUs, where each AP has 2 CCUs and 2 CEUs in its coverage area. For Scenario 3 with a total of 16 users, we consider 12 CCUs and 4 CEUs, while 3 CCUs and 2 CEUs are served by each AP. All Rxs are considered to be

placed at 0.85 m above the floor level.

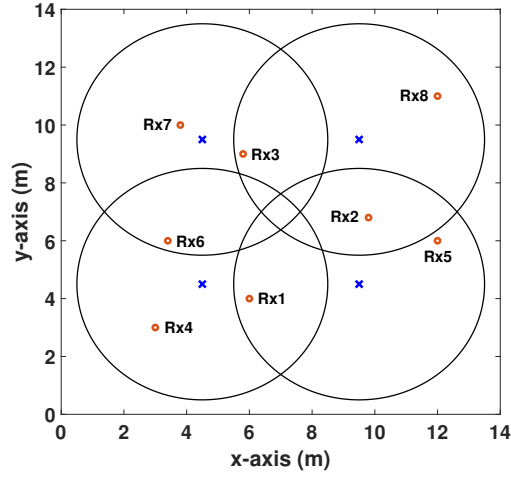
Figure 5.3 presents the maximum achievable throughput for the users in the three considered scenarios. For OFDMA, we observe less dissimilarity (or in other words, more homogeneity) in the users' performance, compared to NOMA. This results from employing FFR in the OFDMA approach for ICI mitigation, making CEUs' performance close to that of CCUs. Indeed, for OFDMA, users' performances mostly depend on their channel gains, the size of the sub-bands allocated to them, and the power allocated to these sub-bands. On the other hand, for the NOMA approach, users' performances largely depend on their channel gain, their decoding order (which determines the amount of interference canceled by SIC), and the PA technique used. In fact, although this PA corresponds to the channel gains of the users, they experience different levels of interference. In addition, for NOMA, CEUs suffer from ICI because of receiving signals from more than one AP.

We have further contrasted in Fig. 5.4 the sum-rate (i.e., the sum of maximum achievable throughputs) of CEUs and the ensemble of users for the two cases of NOMA and OFDMA signaling and the three considered scenarios of Fig. 5.2. Considering the sum-rate of CEUs, we notice that OFDMA slightly outperforms NOMA in all scenarios, elucidating the efficacy of FFR in mitigating ICI. Meanwhile, the difference between the CEUs' sum-rates with OFDMA and NOMA is less significant in Scenarios 2 and 3, which shows that increasing the cell density degrades CEUs performance in OFDMA, compared to NOMA. On the other hand, when considering the total network sum-rate, we notice that for all scenarios, NOMA outperforms OFDMA, which shows the merit of the former in dealing with multi-cell VLC networks. This clear advantage can be attributed to partitioning bandwidth resources among users in OFDMA, whereas in NOMA, users have access to the whole bandwidth all the time. Based on the comparison results, we consider further development of NOMA in the following two chapters.

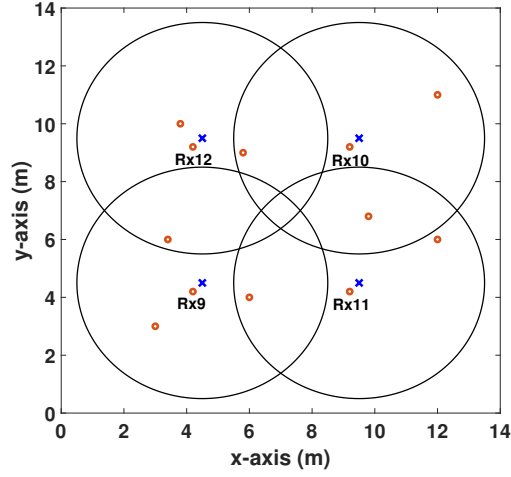
To address ICI in multi-cell NOMA VLC networks, while improving the performance of users, we propose two NOMA-based solutions in the next 2 chapters.

As noticed in the presented above, despite the merits of NOMA in terms of sum-rate, NOMA users performance could vary largely, resulting in a low fairness, due to the variations in the channel gains, the power allocated to users signals, and the amount of IUI experienced by each user (i.e., according to the decoding order). For this reason, to assess the performance of the developed NOMA schemes in the next chapters, in addition to the network sum-rate, we will consider the fairness criterion. To calculate the sum-rate, we will use (5.7) and (5.8) to calculate the SINR and the achievable throughput for NOMA users, respectively. Concerning the fairness metric, the *Jain's fairness index*, denoted FI, will be used to provide an indication of the homogeneity of users performances across the network [140], which has the advantage of being a simple quantitative measure [141]. For given N_r users, FI is defined as

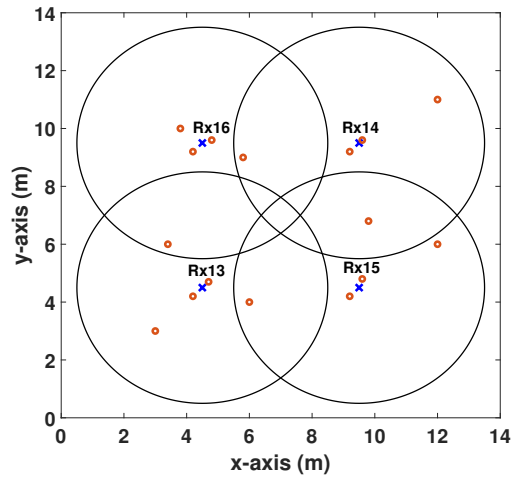
$$FI = \frac{\left(\sum_{j=1}^{N_r} R_j \right)^2}{N_r \sum_{j=1}^{N_r} R_j^2}, \quad (5.9)$$



(a) Top view for Scenario 1

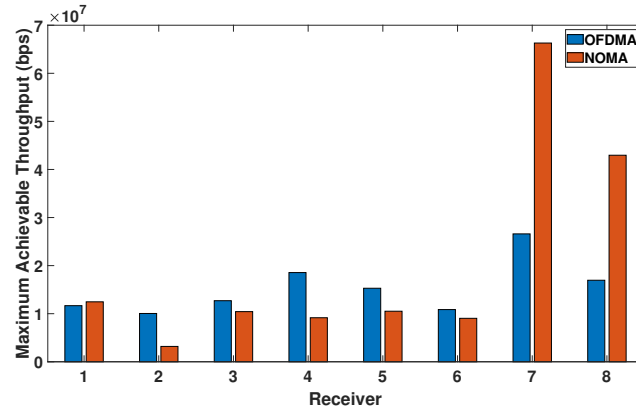


(b) Top view for Scenario 2

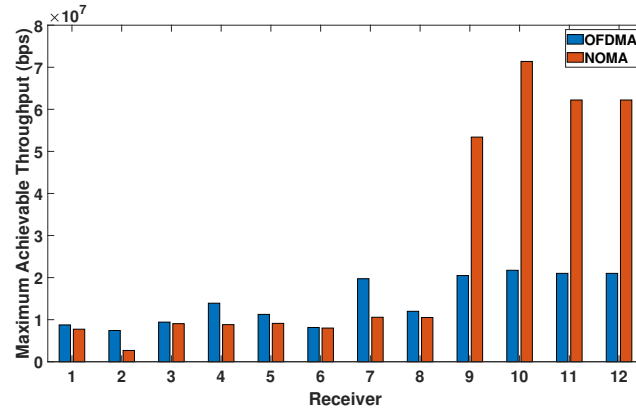


(c) Top view for Scenario 3

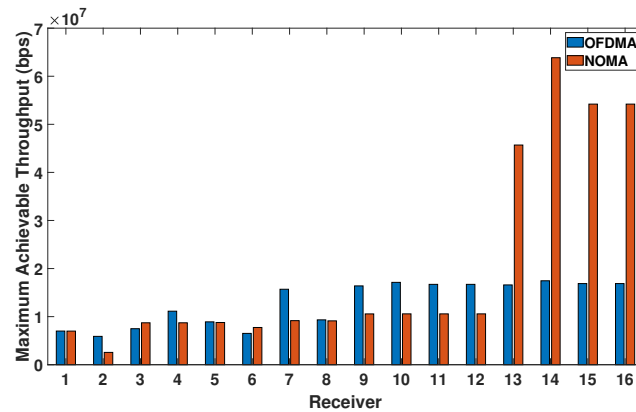
Figure 5.2 — Illustration of the considered scenarios, where \times and \circ show APs and users locations, respectively. Scenario 2 has four additional users with respect to Scenario 1, and Scenario 3 has four additional users with respect to Scenario 2, whose locations are indicated on Figs. 5.2(b) and 5.2(c), respectively.



(a) Scenario 1



(b) Scenario 2



(c) Scenario 3

Figure 5.3 — Contrasting users' maximum achievable throughput using NOMA and OFDMA approaches for the scenarios presented in Fig. 5.2.

where R_j is the upper bound on the throughput of U_j . When all users achieve the same upper bound on their data rate, the denominator equals $N_r(N_r R_j^2)$, resulting in $FI = 1$. As the difference between these bounds increases, FI decreases. Indeed, the interest of considering FI in our study

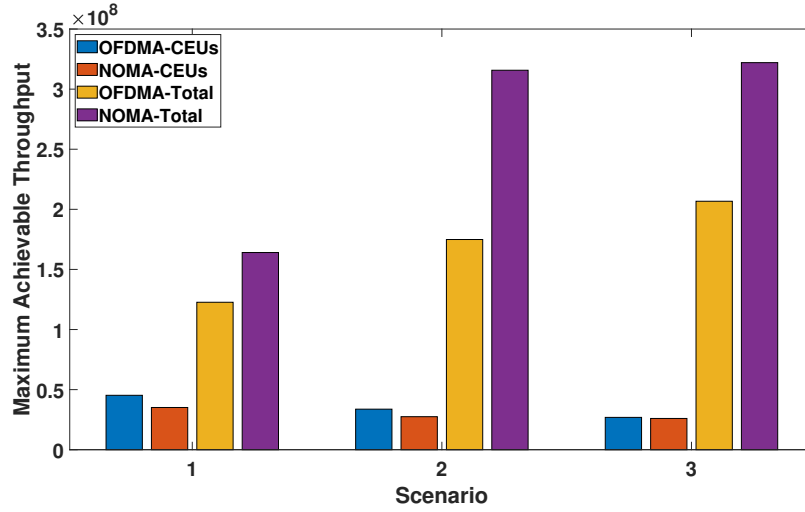


Figure 5.4 — Comparison between the sum-rates of the CEUs and the total network using NOMA and OFDMA approaches for the three considered scenarios.

is that it jointly considers the homogeneity of data rates of both CCUs and CEUs.

5.4 Chapter summary

In this chapter, we investigated appropriate MA techniques for large-space multi-cell VLC networks. Focusing on the most relevant techniques, i.e., OFDMA and NOMA, we contrasted their performance for three scenarios of different complexities. We showed that, for all considered scenarios, NOMA outperforms OFDMA in terms of the total network sum-rate, which is similar to the conclusions of the recent literature on single cell networks. However, we specifically showed that OFDMA outperforms NOMA in terms of the total achievable throughput of CEUs in a multi-cell network.

Note that, the improvement in network sum-rate using NOMA comes at the expense of decreased homogeneity of users' performance. This results from the difference in the allocated power and in the interference level experienced by each user (depending on its decoding order and ICI). Although OFDMA shows a better performance for CEUs due to interference mitigation using FFR, increasing user density in the cells reduces the performance gain with respect to NOMA. Based on the comparison results, NOMA will be considered for further development in the next chapters in terms of interference mitigation, sum-rate, and fairness performance.

Chapter 6

Hybrid NOMA-ZF pre-coding for VLC Networks

Contents

| | |
|---|-----------|
| 6.1 Introduction | 65 |
| 6.2 Hybrid NOMA-ZFP | 66 |
| 6.2.1 Concept | 66 |
| 6.2.2 NOMA-ZFP schemes | 68 |
| 6.3 Performance study of hybrid NOMA-ZFP schemes | 69 |
| 6.3.1 Main assumptions and considered scenarios | 70 |
| 6.3.2 Performance study | 73 |
| 6.3.3 Computational complexity and network latency | 79 |
| 6.4 Chapter summary | 81 |

6.1 Introduction

Following the comparison results presented in Chapter 5, we propose in this chapter NOMA-based schemes for MU multi-cell VLC networks which combine NOMA for IUI management and MISO ZF pre-coding for ICI management. The main idea is to allow CCUs to reduce IUI through SIC detection in a NOMA scheme, while allowing CEUs to remove ICI based on ZF pre-coding. As highlighted in Chapter 2, compared to other linear pre-coding schemes, ZF pre-coding offers simplicity while providing good performance at high SNR, which is typically the case for indoor VLC networks [75–77]. More specifically, in this *hybrid* approach, termed here *NOMA-ZFP*, the CCUs in a given cell are associated with the corresponding AP, and NOMA signaling is applied to manage them. The signals for the CEUs are first pre-coded and then broadcast from the neighboring APs as the last-priority user in the NOMA scheme, i.e., by allocating to them the smallest portion of the transmit power. At the Rx side, CEUs detect their signals after removing the interference arising

from the CCUs present in the neighboring cells using SIC. Our results show that this approach results in a performance improvement as compared to the case where either NOMA or MISO ZF pre-coding alone are used to manage all users, especially for increased user density within the cells. Moreover, this approach potentially reduces the number of handovers in the case of mobile users because CEUs are managed without a requirement to switch the AP (for instance, compared to the case where a CEU is handled by the AP from which it receives the strongest signal). Numerical results presented here demonstrate the advantage of NOMA-ZFP in terms of sum-rate and fairness as compared with the basic NOMA in different link scenarios. In summary, the advantages of the proposed hybrid NOMA-ZFP schemes include:

- suppressing IUI for CEUs through SIC detection of the corresponding CCUs' signals, and removing ICI of the other CEUs' signals through ZF pre-coding;
- serving CEUs while dedicating a relatively small portion of the APs' powers to them;
- potentially reducing the number of handovers for moving users.

Note that what makes the proposed hybrid scheme particularly suitable for VLC networks (as compared with RF cellular networks) is that these networks should typically handle a low number of users in their coverage area. As a result, the assumption of having the number of CEUs smaller than or equal to the number of APs (which is the condition for using ZF pre-coding) is rather reasonable.

In the sequel, we describe the proposed hybrid NOMA-ZFP scheme in Section 6.2, and the results of comparing NOMA and hybrid NOMA-ZFP schemes in Section 6.3. Then Section 6.4 concludes the chapter.

6.2 Hybrid NOMA-ZFP

6.2.1 Concept

This section introduces the proposed hybrid NOMA-ZFP approach for a multi-cell VLC network, which reduces IUI for CCUs and ICI for CEUs. Firstly, cell boundaries are defined, before the central control unit classifies the existing users into CCUs and CEUs. This is done based on the CSI of all users and according to a predefined minimum threshold channel gain [95], which is set to 9.74×10^{-7} here, corresponding to a 2 m cell radius. The signals from CCUs are coordinated by NOMA by the corresponding APs. Then, ZF pre-coding is employed for the CEU signals, where the resulting signal is broadcast by all neighboring APs. To accomplish this, the ensemble of CEUs is treated as a single "compound user" in the NOMA scheme while allocating to them a relatively low power. Figure 6.1 shows an illustration of the proposed hybrid NOMA-ZFP scheme for the case of a four-cell network.

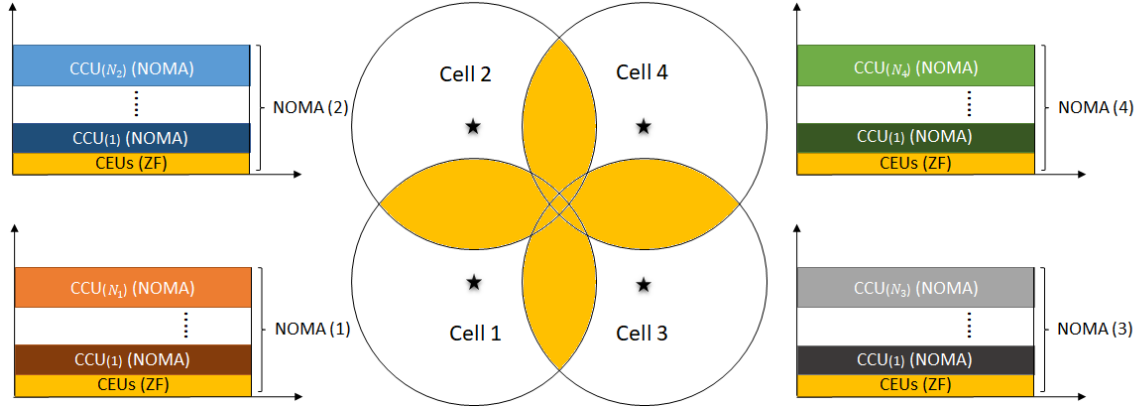


Figure 6.1 — Illustration for the proposed hybrid NOMA-ZFP scheme for a 4-cell scenario. CEU locations correspond to the yellow colored areas, i.e., cell intersections. For instance, N_1 denotes the number of CCUs in Cell 1.

At the Rx side, the signal of CCUs will be marginally impacted by the interference arising from the CEUs as a relatively small portion of the power is allocated to CEUs. On the other hand, CEUs will detect their desired signals after subtracting the CCUs' signals using SIC, assuming that the CSI of these latter is provided for CEUs. It is important to mention that in the application of ZF pre-coding in NOMA-ZFP, the number of CEUs must not exceed the number of related APs. Notice that this constraint is more reasonable than in earlier MISO ZF pre-coding approaches [69, 71–73, 142], which require more luminaires than users. Note that in the cases where the number of CEUs is larger than the number N_t of APs, N_t CEUs will be handled by ZFP and the remaining ones by NOMA (along with the CCUs). Obviously, the CEUs handled by NOMA will suffer from a larger ICI in this way.

Let $N_{\text{CCU},i}$ and N_{CEU} denote the number of CCUs in the i^{th} cell and the total number of CEUs in the network, respectively. Also, let $a_{\text{CCU},i}^2$ and $a_{\text{CEU},i}^2$ denote the total allocated portion of power to CCUs and to CEUs by AP_i , respectively, where $a_{\text{CCU},i}^2 + a_{\text{CEU},i}^2 = 1$. Then, the sum of PA weights for NOMA users cannot exceed $a_{\text{CCU},i}^2$, that is,

$$\sum_{k=1}^{N_{\text{CCU},i}} a_{ik}^2 \leq a_{\text{CCU},i}^2, \quad (6.1)$$

where a_{ik}^2 is the NOMA PA weight used at AP_i for the k^{th} CCU. Similarly, the sum of the pre-coding weights per AP_i cannot be larger than $a_{\text{CEU},i} \sqrt{P_e}$, that is,

$$\sum_{k=1}^{N_{\text{CEU}}} |w_{ik}| \leq a_{\text{CEU},i} \sqrt{P_e}. \quad (6.2)$$

Note that the conditions of (6.1) and (6.2) can also be considered to be related to the illumination constraints, determined by P_e . Also, note that in the case where no CCU is present in a cell (say, Cell i), the entire AP power is allocated to the CEUs, i.e., $a_{\text{CEU},i} = 1$. Similarly, when there is no CEU in the network, the entire AP power is allocated to CCUs, i.e., $a_{\text{CCU},i} = 1$.

Given that NOMA-ZFP scheme relies basically on the conventional NOMA, we provide in the following the formulation of the received signal based on NOMA signalling provided in Subsection 5.2.2¹. For user U_j with NOMA-ZFP signalling, the received signal is given by:

$$r_j = \sum_{i=1}^{N_t} \sum_{k=1}^{N_{\text{CCU},i}+1} a_{ik} \sqrt{P_e} h_{ij} d_k + z_j, \quad (6.3)$$

where the AP_{*i*} handles the signal of $N_{\text{CCU},i}$ CCUs plus that of all CEUs (remember that the signal for CEUs is transmitted as the highest decoding order user in the NOMA scheme). We can rewrite (6.3) in the following form:

$$r_j = \sum_{i=1}^{N_t} \sum_{k=1}^{N_{\text{CCU},i}} a_{ik} \sqrt{P_e} h_{ij} d_k + \sum_{i=1}^{N_t} h_{ij} x_i + z_j, \quad (6.4)$$

where the first and the second terms represent the CCU and the CEU signals, respectively, and x_i is the CEUs ZF pre-coded signal sent by AP_{*i*}:

$$x_i = \sum_{k=1}^{N_{\text{CEU}}} w_{ik} d_k, \quad (6.5)$$

where d_k is the k^{th} CEU symbol and w_{ik} is the corresponding ZF pre-coding weight. Note that, according to (6.2), x_i is bounded by $a_{\text{CEU},i} \sqrt{P_e}$, which in fact sets a power limitation on CEUs. Using (2.8), we can write (6.4) as follows.

$$\begin{aligned} r_j = & \sum_{i=1}^{N_t} \sum_{k=1}^{N_{\text{CCU},i}} a_{ik} \sqrt{P_e} h_{ij} d_k \\ & + \left(\mathbf{h}_j^T \mathbf{w}_j^T d_j + \sum_{k \neq j} \mathbf{h}_j^T \mathbf{w}_k^T d_k \right) + z_j. \end{aligned} \quad (6.6)$$

If U_j is a CCU served by a given AP, the first term in (6.6) will include the desired signal and the ICI (here, the signals from other APs can be ignored as they are likely too weak), whereas the second term will represent the interference from CEU signals. On the other hand, if U_j is a CEU, the first term in (6.6) will represent the interference arising from CCUs (which is ideally removed by SIC), whereas the second term will include the desired signal (given that the interference of other CEUs is removed with ZF pre-coding).

6.2.2 NOMA-ZFP schemes

We propose and investigate two hybrid schemes, which differ in the criterion used for calculating the pre-coding weight matrix \mathbf{W} . From (2.9) and (6.6), the received signal vector of all CEUs in NOMA-ZFP is given by $\mathbf{r} = \mathbf{H} \mathbf{W} \mathbf{d} + \mathbf{z}$, where \mathbf{W} is calculated from (2.10). Let us define vector $\boldsymbol{\mu}$ and matrix \mathbf{A} as follows:

$$\boldsymbol{\mu} = [\mu_1, \dots, \mu_{N_{\text{CEU}}}] = \left[\frac{\gamma_1}{\sigma_1}, \dots, \frac{\gamma_{N_{\text{CEU}}}}{\sigma_{N_{\text{CEU}}}} \right], \quad (6.7)$$

¹Note that, in this chapter, the dependence of r_j on AP_{*i*} is implicit. This allows us to use the same notation for the case of hybrid schemes.

$$\mathbf{A} = \text{abs}\left(\mathbf{H}^T (\mathbf{H}\mathbf{H}^T)^{-1}\right) \text{diag}(\boldsymbol{\sigma}), \quad (6.8)$$

such that

$$\mathbf{A}\boldsymbol{\mu} \leq \mathbf{F}_{\text{CEU}}; \quad \boldsymbol{\mu} \geq \mathbf{0}. \quad (6.9)$$

Here, $\mathbf{0}$ represents an all-zero vector, and

$$\mathbf{F}_{\text{CEU}} = \left[a_{\text{CEU},1} \sqrt{P_e}, \dots, a_{\text{CEU},N_t} \sqrt{P_e} \right]. \quad (6.10)$$

In the first approach that we propose, termed *NOMA-ZFP-A*, the objective is to maximize the minimum achievable rate for CEUs that is a function of $\boldsymbol{\mu}$. This is referred to as the max-min fairness criterion in [69]:

$$\text{maximize} \quad \log_2(1 + \mu_{\min}^2), \quad (6.11)$$

where μ_{\min} corresponds to the smallest entry in vector $\boldsymbol{\mu}$, which can be obtained as:

$$\mu_{\min} = \frac{\min(\mathbf{F}_{\text{CEU}})}{\max(\mathbf{A}\mathbf{1})} \quad \text{subject to (6.9)}. \quad (6.12)$$

By optimizing μ_{\min} from (6.11), the optimum $\boldsymbol{\mu}$ will equal $\mu_{\min} \mathbf{1}$, where $\mathbf{1}$ is the vector with all entries equal to one. In (6.12), the relationship of μ_{\min} to $\min(\mathbf{F}_{\text{CEU}})$ can be explained as to satisfy the lowest illumination constraint for CEU signals among all APs, and its relationship to $\max(\mathbf{A}\mathbf{1})$ is to guarantee the largest \mathbf{W} for any AP transmission while satisfying (6.2). Note that our proposed solution is more general, compared with [69, Eq.(28)]. Indeed, the solution of (6.11)-(6.12) accounts for the cases where APs have different power constraints on the ZF pre-coding weights (see (6.2)), by considering the minimum bound among all APs in the nominator of (6.12). In contrast, the solution proposed in [69] considers APs with the same power constraint on the pre-coding weights.

In the second approach, denoted by *NOMA-ZFP-B*, the target is the optimization of $\boldsymbol{\mu}$, subject to the constraint in (6.9), by maximizing the achievable throughput of CEUs [69]. Again, as CEU throughputs are function of their SNR (related to $\boldsymbol{\mu}$), the optimization is achieved by:

$$\text{maximize} \quad \log_2(\det(\mathbf{I} + \text{diag}(\boldsymbol{\mu} \odot \boldsymbol{\mu}))), \quad (6.13)$$

where \odot denotes the Hadamard product. To avoid a non-concave objective function [142] while solving the problem as a standard determinant maximization, we simplify (6.13) to the following form, as considered in [69]:

$$\text{maximize} \quad \det(\mathbf{I} + \text{diag}(\boldsymbol{\mu})). \quad (6.14)$$

To solve (6.14), we use the CVX package [143, 144] for convex optimization, similar to [69]. After calculating $\boldsymbol{\mu}$, we can calculate γ from (6.7), and subsequently \mathbf{W} can be obtained using (2.10).

6.3 Performance study of hybrid NOMA-ZFP schemes

To highlight the performance of the proposed MA scheme, numerical results are presented for the case of a four-cell VLC network, as illustrated in Fig. 6.1.

Table 6.1 — Simulation parameters.

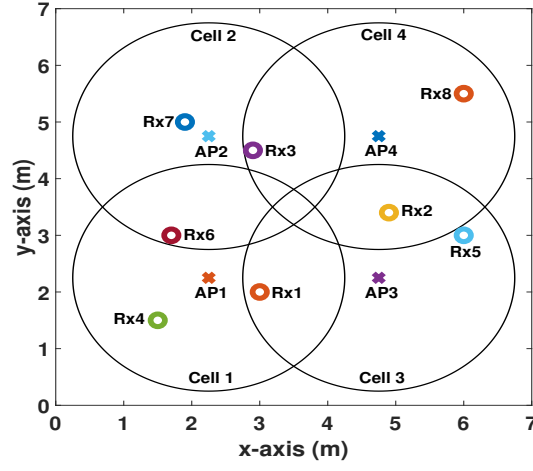
| Parameter | Value |
|--|---|
| Room dimension | $(7 \text{ m} \times 7 \text{ m} \times 3 \text{ m}) \text{ m}^3$ |
| LED luminaire Lamertian order m | 1 |
| Number of LED chips per luminaire | 36 [72] |
| LED conversion efficiency S | 0.44 W/A [72] |
| PD responsivity R | 0.4 A/W [47] |
| PD area | 1 cm^2 [69] |
| Rx's FOV | 62° . [69] |
| Refractive index of optical concentrator | 1.5 [69] |
| System bandwidth B | 10 MHz |
| Equivalent Rx noise power spectral density | $10^{-21} \text{ A}^2/\text{Hz}$ [47] |

Compared with NOMA-ZFP-B, NOMA-ZFP-A has a much lower computational complexity for calculating \mathbf{W} . Given the aforementioned optimization criteria, we expect that NOMA-ZFP-A provides a better FI (especially for relatively low SNRs), whereas NOMA-ZFP-B should provide a higher sum-rate (see Subsection 6.3.2).

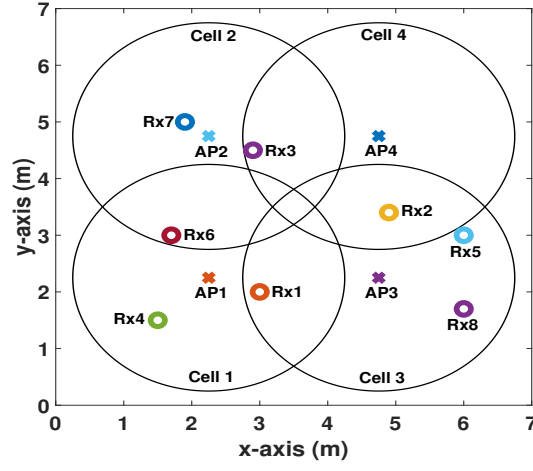
6.3.1 Main assumptions and considered scenarios

In the considered configuration, within each cell, an LED luminaire acting as AP is placed at the center. The total number of users is set to 8 and different scenarios are considered with respect to their positions inside the room. The Rx's are assumed to be placed at 0.85 m above the floor level. Table 6.1 summarizes the simulation parameters. Assuming the use of optical concentrator at the Rx, the channel gain is then calculated using equation (2.2). Note that, though the presented numerical results depend on the particular parameters chosen, higher data rates can be possible with wider bandwidth LEDs or greater Tx power. The presented analysis and conclusions can be generalized to other scenarios.

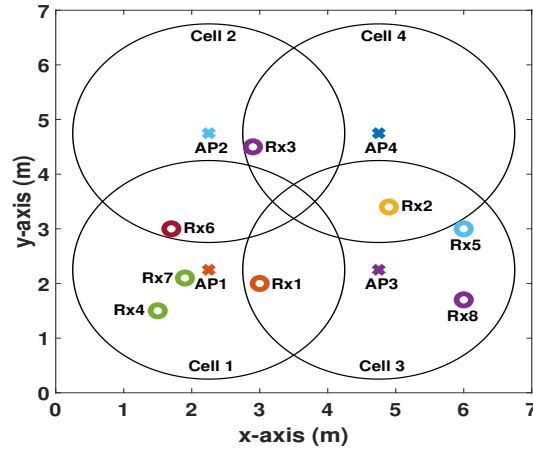
Figure 6.2 illustrates the three scenarios considered, showing the specific locations of the users and the APs, and the cell boundaries. Note that we will present later at the end of Subsection 6.3.2 a more general study by considering 100 randomly generated scenarios. In all considered scenarios, there is a single CEU in the coverage area of two adjacent cells. In Scenario 1 (in Fig. 6.2(a)), users are nearly equally distributed within the cells, such that each cell has in its coverage one CCU. In Scenario 2 (in Fig. 6.2(b)), Cell 4 has no CCU, Cell 3 has two CCUs, and the other two cells have one CCU. Lastly, in Scenario 3 (in Fig. 6.2(c)), Cells 2 and 4 have no CCUs, and the two other cells have two CCUs. The same locations and numbers of CEUs are considered for all scenarios, which are specified in Table 6.2, together with the locations of APs and those of CCUs according to the different considered scenarios. These are chosen to represent an increase in complexity from



(a) Scenario 1



(b) Scenario 2



(c) Scenario 3

Figure 6.2 — Illustration of top view of the considered scenarios: \times and \circ represent AP and user locations, respectively.

Table 6.2—Locations of APs, CCUs, and CEUs (in meter) in the considered scenarios.

| Scenario | APs locations: AP1, AP2, AP3, AP4 |
|----------|--|
| 1, 2, 3 | (2.25, 2.25, 2.5), (2.25, 4.75, 2.5), (4.75, 2.25, 2.5), (4.75, 4.75, 2.5) |
| Scenario | CCUs locations: Rx4, Rx5, Rx7, Rx8 |
| 1 | (1.5, 1.5, 0.85), (6, 3, 0.85), (1.9, 5, 0.85), (6, 5.5, 0.85) |
| 2 | (1.5, 1.5, 0.85), (6, 3, 0.85), (1.9, 5, 0.85), (6, 1.7, 0.85) |
| 3 | (1.5, 1.5, 0.85), (6, 3, 0.85), (1.9, 2.1, 0.85), (6, 1.7, 0.85) |
| Scenario | CEUs locations: Rx1, Rx2, Rx3, Rx6 |
| 1, 2, 3 | (3, 2, 0.85), (4.9, 3.4, 0.85), (2.9, 4.5, 0.85), (1.7, 3, 0.85) |

Table 6.3—Decoding order of users' signals for NOMA-A (ascending)

| Scenario | Cell 1 | Cell 2 | Cell 3 | Cell 4 |
|----------|-----------------------|-----------------|-----------------------|-----------------|
| 1 | Rx4 - Rx6 - Rx1 | Rx6 - Rx3 - Rx7 | Rx1 - Rx5 - Rx2 | Rx3 - Rx8 - Rx2 |
| 2 | Rx4 - Rx6 - Rx1 | Rx6 - Rx3 - Rx7 | Rx1 - Rx5 - Rx8 - Rx2 | Rx3 - Rx2 |
| 3 | Rx4 - Rx6 - Rx1 - Rx7 | Rx6 - Rx3 | Rx1 - Rx5 - Rx8 - Rx2 | Rx3 - Rx2 |

Scenario 1 to Scenario 3, by increasing the irregularity of users' distribution within the cells. The different locations of CCUs also allows for the investigation of the performance of the developed NOMA-ZFP algorithms in a variety of environments.

For comparing NOMA with NOMA-ZFP, we consider both of NOMA-A and NOMA-B schemes(see Subsection 5.2.2). Note that, given the advantage of NOMA-ZFP in dealing with ICI compared with conventional NOMA, in the considered scenarios we have intentionally considered CEUs as being in the coverage area of only two APs. In fact, when a CEU is placed in the intersection of three or four APs, this will result in a considerably degraded performance for NOMA-A and NOMA-B schemes. Indeed, for NOMA-A, this will increase the number of users handled by the corresponding APs, resulting in less resources available per user. For NOMA-B, those CEUs will be severely penalized due to receiving a high level of interference from the other APs. Here, we exclude such particular cases for which the hybrid approach will clearly outperform the NOMA-only approaches.

For the CCUs employing NOMA, we consider static PA with $\alpha = 0.3$, which was verified through simulations to make the best compromise between the sum-rate and FI for Scenario 1. Concerning CEUs, we impose the QoS constraint on minimum achievable user rate of 5 Mbps, which in turn gives a constraint of a minimum SNR of 1 dB. Accordingly, the PA weight α_{CEU}^2 in the hybrid scheme is set to 6%, which was calculated for Scenario 1 so as to satisfy the QoS condition.

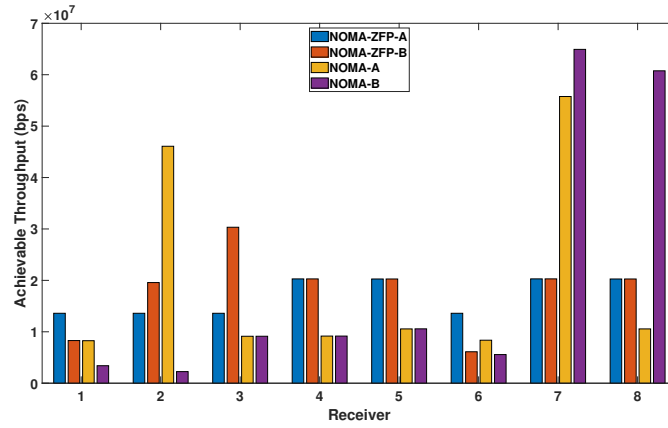
6.3.2 Performance study

Figure 6.3 shows the upper bounds on the throughput of different users in the three considered scenarios and with the four MA schemes of NOMA-A, NOMA-B, NOMA-ZFP-A, and NOMA-ZFP-B.

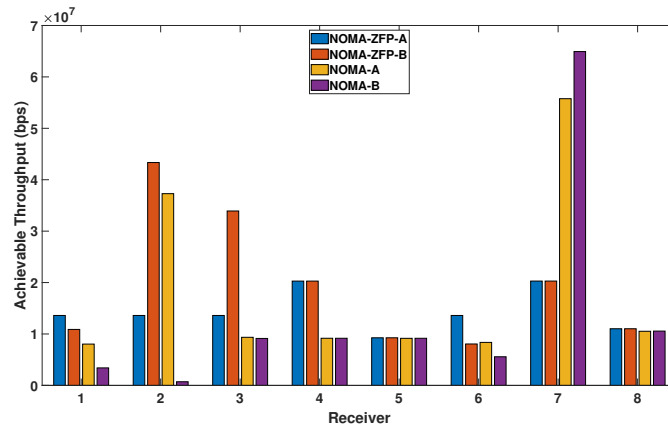
The performance of several particular users are highlighted in the following in order to provide a deeper interpretation of the results in Fig. 6.3. For the sake of clarification, Table 6.3 lists the decoding order in detecting users' signals (ascending order) for the case of NOMA-A.

- Case of Rx2: In Scenario 1, this user attains a much higher throughput with NOMA-A, compared with NOMA-B, in particular. By referring to Table 6.3, the decoding order for Rx2 in both cells 3 and 4 is the largest, which means it detects its signal after the other users and hence can remove their interference using SIC. In Scenarios 2 and 3, Rx2 achieves a higher throughput with NOMA-ZFP-B because the whole power of AP 4 is allocated to the CEUs as there is no CCU in Cell 4.
- Case of Rx7: In Scenario 1, NOMA-A and NOMA-B provide a much better performance, compared to the hybrid schemes. In particular, with NOMA-B, a smaller number of users are handled by AP 2 (compared with the NOMA-A case) and, consequently, this AP has more power resources available per user. In addition, Rx7 has the highest decoding order (permitting interference removal using SIC), resulting in the relatively high throughput for this user. For the same reasons, Rx7 has still a superior performance in Scenarios 2 and 3 with NOMA-A and NOMA-B, as compared to the hybrid schemes.
- Case of Rx8 in Scenario 1: We notice a much higher throughput for this user with NOMA-B. Here Rx2 and Rx3 are associated with the AP 3 and AP 2, respectively, which leads to allocating all the AP 4 power to Rx8. As a result, Rx8 is the only effective user in Cell 4 having no interfering users.
- Case of Rx3 in Scenario 3: This user attains almost the same throughput with NOMA-A and NOMA-B. In fact, although Rx3 is the only user in Cell 2 with NOMA-B, which leads to more received power from AP 2, this is associated with more interference from AP 4.

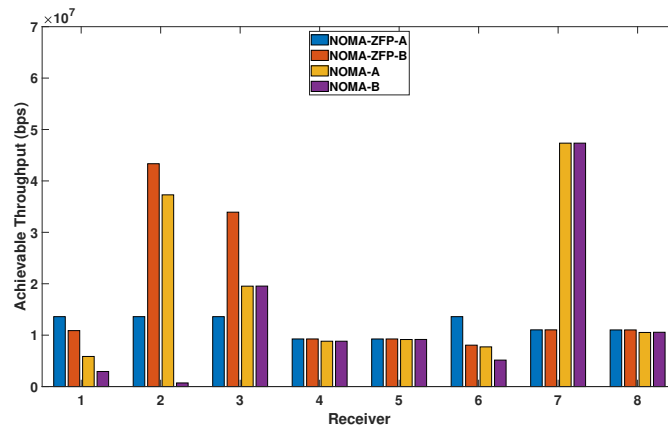
Figure 6.4 presents the FI for the achievable network throughput in the three considered scenarios. Notice that NOMA-ZFP-A and NOMA-ZFP-B outperform the two other MA schemes in all scenarios. The reason of this advantage is three-fold: (i) having a smaller number of only-NOMA-associated users in the cells (i.e., without ZF pre-coding), which allows a better utilization of the resources to achieve a better individual performance for the users; (ii) benefiting from the broadcast feature of the MU-MISO, which allows allocating a small portion of the total available power in each AP to achieve an acceptable performance for CEUs, while decreasing the interference caused by CEU signals on CCUs; and (iii) exploiting SIC for canceling the interference arising from CCU signals on CEUs. Meanwhile, notice an improved performance in terms of fairness for NOMA-



(a) Scenario 1



(b) Scenario 2



(c) Scenario 3

Figure 6.3 — Upper bounds on the achieved rates for the users with NOMA-A, NOMA-B, NOMA-ZFP-A, and NOMA-ZFP-B schemes for the three considered scenarios in Fig. 6.2;

$$P_o = 1.584 \text{ W.}$$

ZFP-A, as compared with NOMA-ZFP-B for all scenarios, which is due to the optimization criterion used for the former, as described in Subsection 6.2.2. Also, NOMA-A outperforms NOMA-B since it ensures a more uniform performance for the users by decreasing the ICI effect for CEUs.

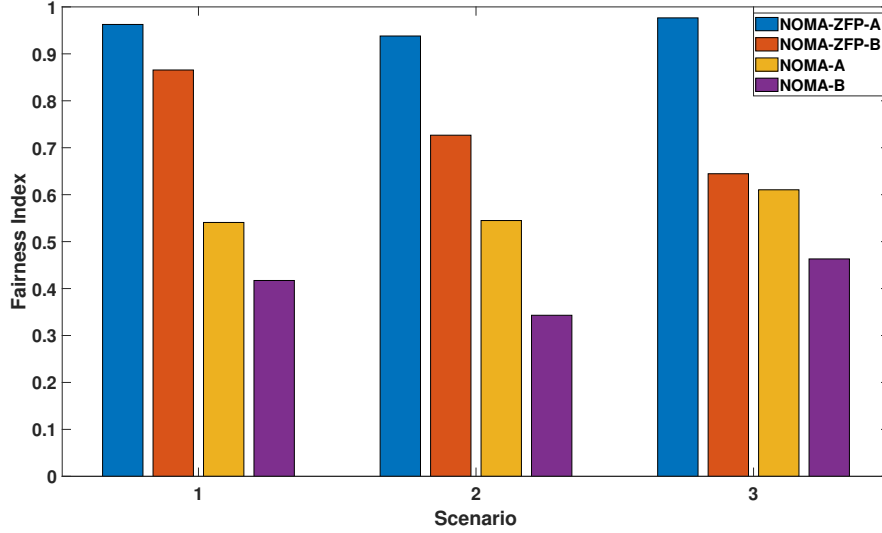


Figure 6.4 — Network FI comparison for the considered MA schemes; $P_o = 1.584$ W.

We have further compared the total network throughput, i.e., sum-rate, of the four MA schemes in Fig. 6.5 for the three scenarios, which is calculated using (2.16) and (5.8). Notice that NOMA-B has the maximum performance in Scenario 1 since every Rx is associated with only one AP (see Fig. 6.2), which globally results in increased power per user for each AP. The opposite situation arises in Scenarios 2 and 3 where the association with only one AP penalizes NOMA-B. For instance, Cell 4 has no CCU to serve and the CEUs are associated with the nearest AP, which results in wasting the resources of AP 4. We notice that NOMA-ZFP-B offers a better performance for Scenario 2, compared with NOMA-A, whereas the latter outperforms it for Scenarios 1 and 3. Indeed, the users corresponding to the highest channel gains in NOMA-A are allocated the smallest PA weight. These users benefit from SIC for removing the interference, which is not the case with NOMA-ZFP-B. Among NOMA-ZFP-A and NOMA-ZFP-B, the latter provides a superior performance in all scenarios, which is due to the optimization criterion used for calculating the pre-coding weights \mathbf{W} .

For the sake of completeness and to better see the advantage of the ZFP-based schemes, we have contrasted in Fig. 6.6 the total achievable data rates for the CEUs. As expected, NOMA-B offers the worst performance, because with this scheme, CEUs are affected by the interference they receive from the other APs (other than their main AP), resulting in degraded SINR and hence decreased throughput. We notice that in Scenarios 2 and 3, NOMA-ZFP-B offers the best performance. In fact, while ensuring a target performance for CEUs (here we imposed the QoS requirement of at least 5 Mbps data rate per user) using a fraction of the available power in each AP (see Subsection 6.3.1), NOMA-ZFP-B benefits from the broadcast feature of the MU-MISO, while min-

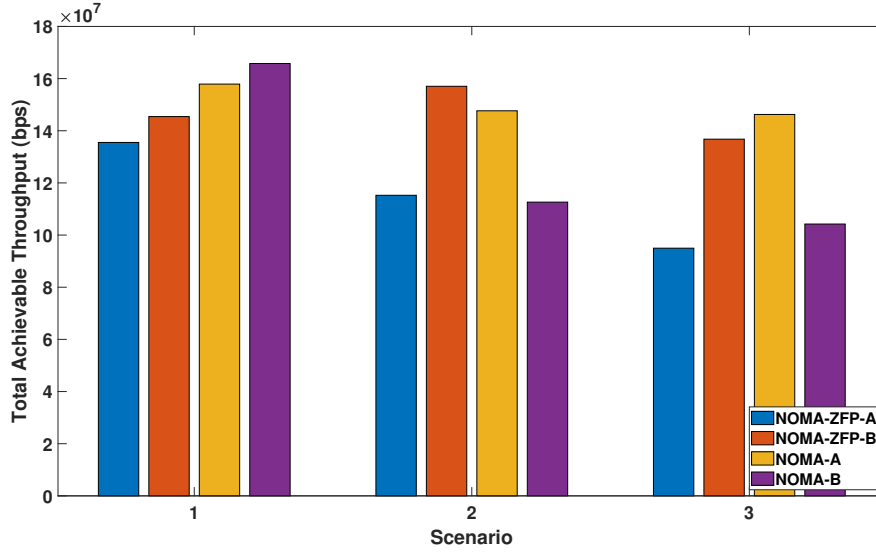


Figure 6.5 — Network sum-rate comparison for the considered MA schemes; $P_o = 1.584$ W.

imizing the interference caused by the CCUs signals using SIC. For Scenario 1, however, NOMA-A outperforms NOMA-ZFP-B, because the former benefits from a high throughput of Rx2, due to the smallest decoding order in Cells 3 and 4 (see Table 6.3), allowing interference cancellation by SIC. Note that this is not the case for Scenarios 2 and 3 where with NOMA-ZFP-B, the entire AP 4 power is allocated to CEUs (there is no CCU in Cell 4). Also, a higher throughput is obtained with NOMA-ZFP-B, compared to NOMA-ZFP-A, which is again due to the optimization criteria considered.

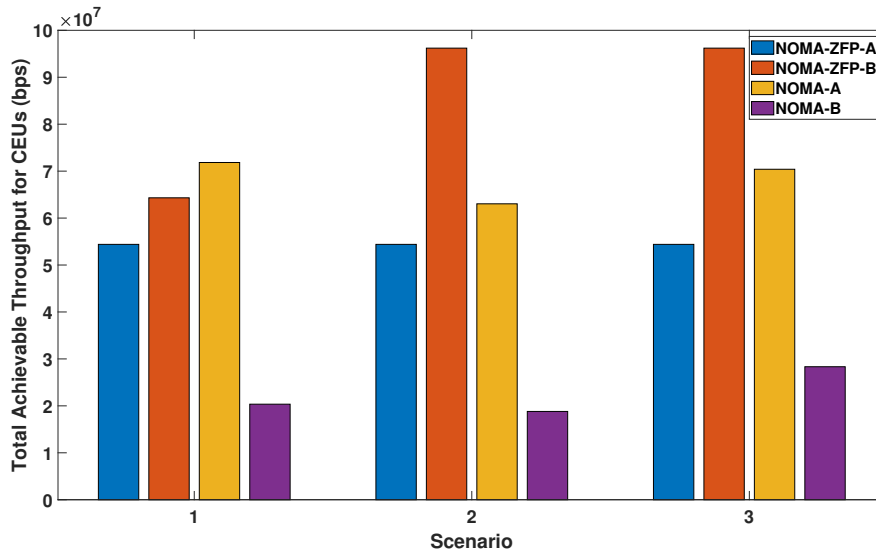


Figure 6.6 — Comparison between the total achieved throughput of CEUs for the considered MA schemes; $P_o = 1.584$ W.

Lastly, the effect of increasing the transmitted optical power P_o on the network sum-rate and

FI is considered in the three scenarios. Results are shown in Figs. 6.7 and 6.8 for $P_o = 5$ and 10 W, while (as before) we have considered allocating 6% of the electrical power to CEUs. Note that the increase in P_o can be achieved by adding more LEDs to a luminaire, for instance. Indeed, we expect that with increased P_o , better performance can be achieved for CEUs (as they perform SIC for interference cancellation), and the proposed hybrid schemes become even more advantageous. Notice from Fig. 6.7 that, with increased P_o , NOMA-ZFP-B outperforms NOMA-A and NOMA-B in all scenarios regarding the network sum-rate, and that the performance of NOMA-ZFP-A also improves with respect to these latter. Furthermore, from Fig. 6.8, at higher values of P_o , the hybrid schemes outperform NOMA-A and NOMA-B in all scenarios regarding FI. Note that similar conclusions can be drawn for the case of changing the Rx height, which will affect the received power.

In all previously-presented results, we considered the three special scenarios of Fig. 6.2. Although the rationale behind considering these cases was explained (see Subsection 6.3.1), it would be interesting to see the performance of the proposed hybrid methods on average. For this purpose, we have considered randomly generated users' locations within the 4-cell room (of the same dimensions as in Fig. 6.2). The optical power corresponding to each AP is set to $P_o = 1.584$ W. The average sum-rate and FI are presented in Table 6.4, which correspond to a total of 100 scenarios (selected among about 1000 randomly-generated locations for eight users), satisfying the existence of four CEUs, with each CEU being in the coverage area of only two APs. From these results, we notice that, in general, the proposed hybrid schemes outperform the NOMA-based ones in average FI, whereas the latter achieve a better average sum-rate performance. Also, NOMA-ZFP-B outperforms NOMA-ZFP-A in average sum-rate, as shown in the already-presented results (see Figs. 6.5 and 6.7). Concerning the average FI, these results attest the same trend in Figs. 6.4 and 6.8, i.e., NOMA-ZFP-A achieves the best performance, followed by NOMA-ZFP-B, while NOMA-A outperforming NOMA-B.

Table 6.4 — Sum-rate and FI performance averaged over 100 random scenarios

| | NOMA-ZFP-A | NOMA-ZFP-B | NOMA-A | NOMA-B |
|------------------------|--------------------|--------------------|--------------------|--------------------|
| Average sum-rate (bps) | 1.12×10^8 | 1.41×10^8 | 1.67×10^8 | 1.79×10^8 |
| Average FI | 0.83 | 0.75 | 0.52 | 0.46 |

To study the relationship between the network sum-rate and fairness for NOMA-ZFP-A and -B schemes, we have shown in Fig. 6.9 the effect of varying the percentage of the power allocated to CEUs (i.e., a_{CEU}^2) on the average total achievable throughput of CCUs and CEUs, as well as on the average network sum-rate and fairness. To obtain these results, 100 random scenarios were considered with the same conditions as for the results presented in Table 6.4. The results of Fig. 6.9(a) are in accordance with those in Figs. 6.5 and 6.6, where we notice that, with decrease in a_{CEU}^2 , the average throughput of CEUs degrades, unlike that of CCUs. The presented plots have almost the same slope for the two NOMA-ZFP schemes. However, we have a higher throughput for CEUs for

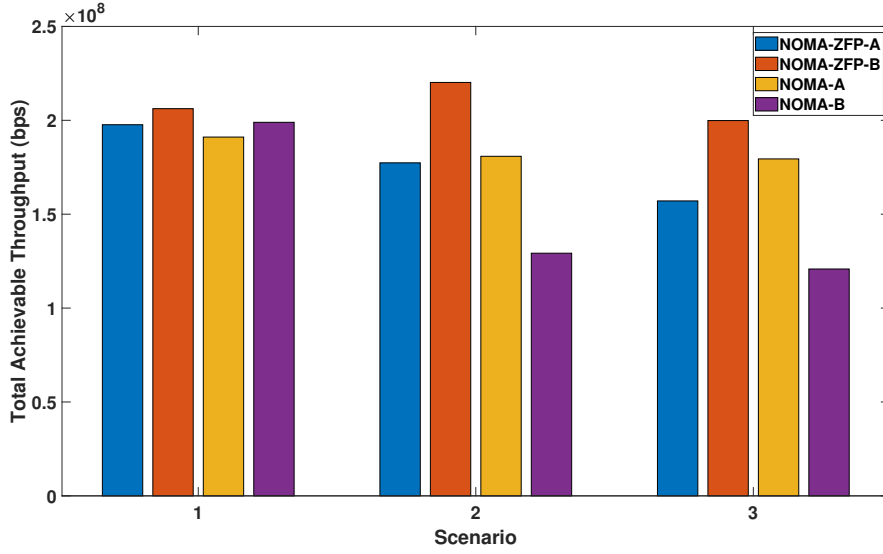
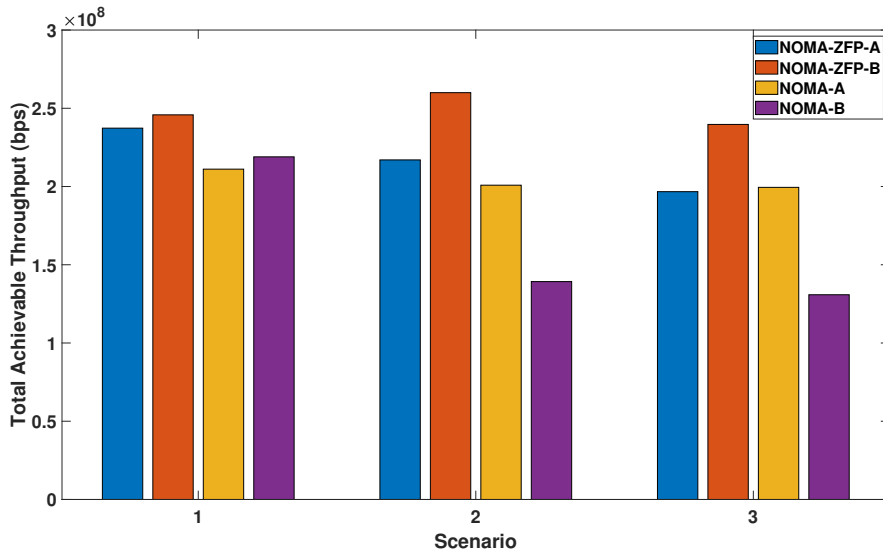
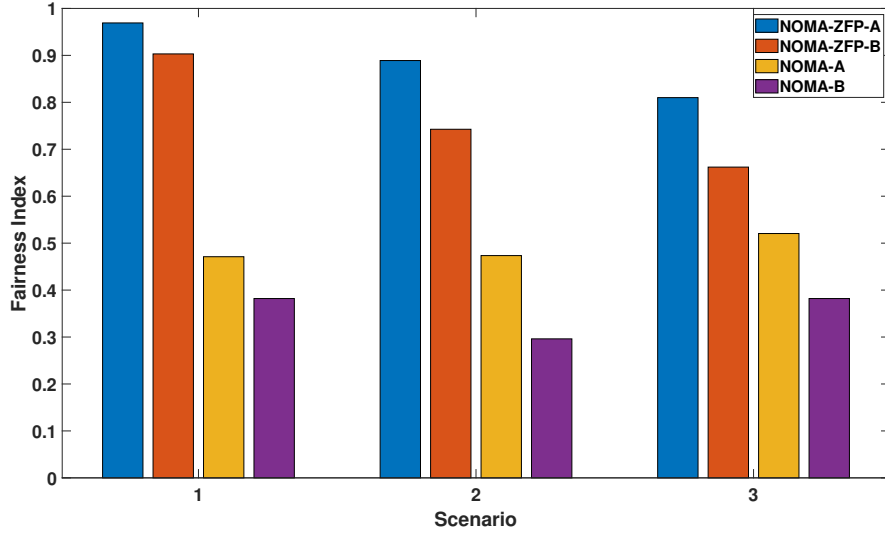
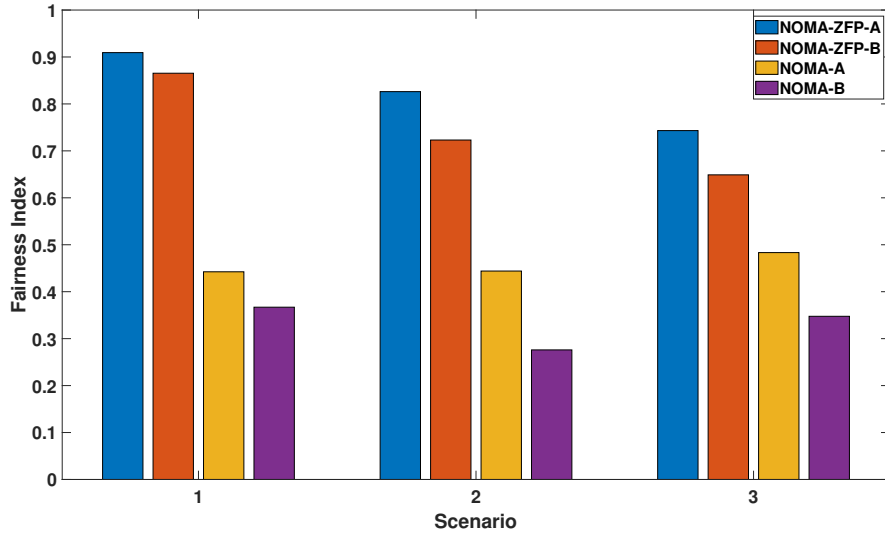
(a) $P_o = 5 \text{ W}$ (b) $P_o = 10 \text{ W}$

Figure 6.7—Comparison of network sum-rate for the different MA schemes for transmitted optical powers of 5 and 10 W.

NOMA-ZFP-B, which is due to the considered criteria for calculating \mathbf{W} (see Subsection 6.2.2). Considering now Fig. 6.9(b), we see a decrease in the average network sum-rate with increase in a_{CEU}^2 due to the decrease in CCUs power. At the same time, this results in a better fairness, as the throughputs of CEUs approach those of CCUs. Interestingly, for NOMA-ZFP-B, there is an optimal value for a_{CEU}^2 (here, 4%) beyond which the fairness degrades, because the throughputs of CEUs dominate the sum-rate and exceed considerably those of CCUs.²

²The optimum a_{CEU}^2 is around 13% for NOMA-ZFP-A, which is not shown in Fig. 6.9 for the sake of presentation

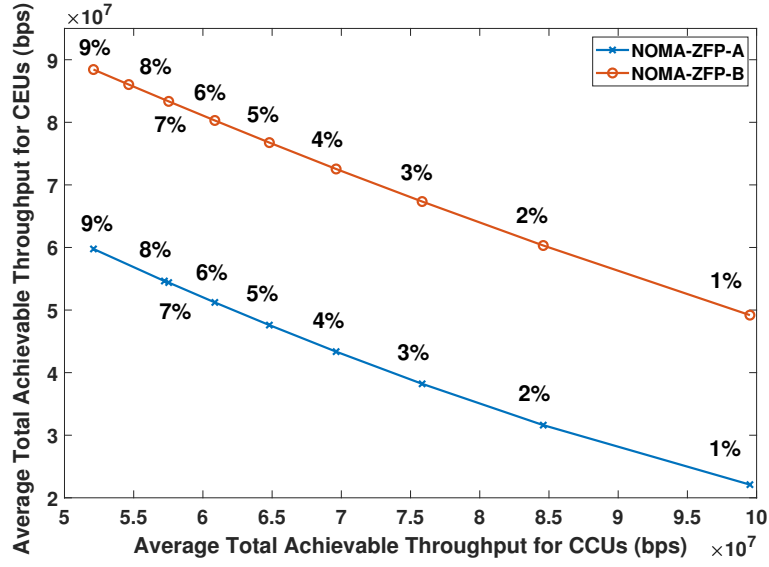
(a) $P_o = 5 \text{ W}$ (b) $P_o = 10 \text{ W}$ **Figure 6.8** — Comparison of network FI of the different MA schemes for $P_o = 5$ and 10 W .

6.3.3 Computational complexity and network latency

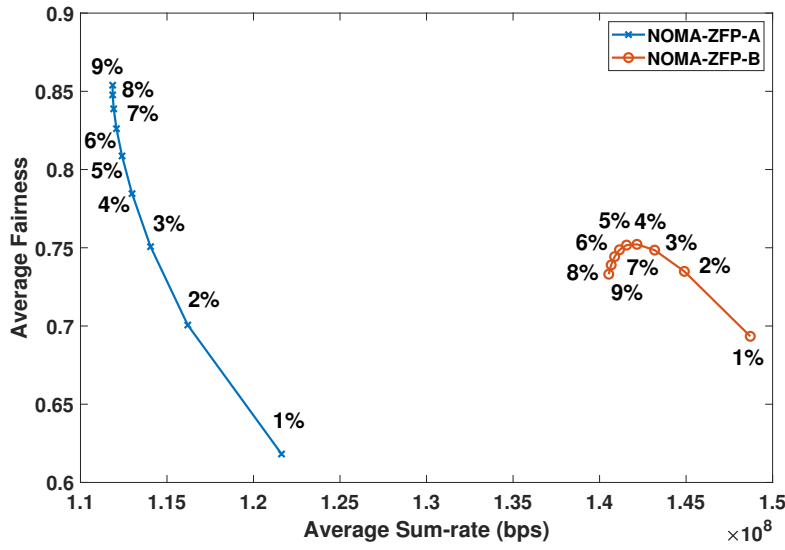
For the sake of completeness, we discuss here the computational complexity of the considered MA schemes at the Tx and the Rx, as well as the overall network latency.

As concerns the computational complexity at the Tx, for NOMA-ZFP schemes, it mainly depends on:

clarity. This optimum is smaller for NOMA-ZFP-B due to the criterion of throughput optimization for this scheme.



(a)



(b)

Figure 6.9— Comparison between (a) average achievable throughput for CCUs and CEUs; and (b) average network sum-rate and fairness for NOMA-ZFP-A and NOMA-ZFP-B schemes, for different percentages of power allocated to CEUs, a_{CEU}^2 .

- Complexity of ZF pre-coding, which mainly concerns matrix multiplication and inversion, and is given by $O(2N_{\text{CEU}}^2 N_t + N_{\text{CEU}}^3)$ [145];
- Complexity of NOMA resource allocation (remember that here we consider the simple static PA, which is of very low complexity);
- Complexity of calculating the optimal \mathbf{W} , which depends on the target criterion (e.g.,

throughput maximization for NOMA-ZFP-B). This complexity is much higher for NOMA-ZFP-B compared to NOMA-ZFP-A, since the former uses convex optimization for calculating \mathbf{W} , with complexity varying depending on the number of iterations needed for the interior point method to converge to the solution in CVX;

- Complexity of acquiring CSI, where NOMA-ZFP schemes add more complexity to the system.

For NOMA schemes, the computational complexity depends on the resource allocation process. In the considered NOMA and NOMA-ZFP schemes, the complexity of NOMA resource allocation is negligible, as only static PA is considered. For this reason, the computational complexity of NOMA schemes is much lower than that of NOMA-ZFP schemes. In addition, NOMA-B has a lower complexity than NOMA-A, as the complexity of resource allocation increases by increased number of users.

Concerning the computational complexity at the Rx side, for NOMA-ZFP schemes, it mainly depends on the complexity of SIC detection. The number of SIC steps needed for both NOMA-ZFP-A and NOMA-ZFP-B equals $\sum_{i=1}^{N_t} \sum_{k=1}^{N_{\text{CCU},i}-1} k + N_{\text{CEU}} \sum_{i=1}^{N_t} N_{\text{CCU},i}$, where the first and the second terms denote the number of SIC steps needed by CCUs and CEUs, respectively. For NOMA schemes, the number of SIC steps equals $\sum_{i=1}^{N_t} \sum_{k=1}^{N_{r,i}-1} k$, where $N_{r,i}$ is the number of users handled by AP_{*i*}. In general, we have a larger $N_{r,i}$ for NOMA-A due to handling of each CEU by multiple APs, resulting in a higher complexity, compared with NOMA-B. Here again, NOMA-ZFP schemes have a higher complexity, compared to NOMA.

Concerning network latency, whatever the MA scheme, the main factors include Tx/Rx computational complexity, handovers, and CSI requirement. Although NOMA-ZFP schemes have a higher computational complexity, they have a significant advantage over NOMA in terms of handovers. This is because handling of CEU signals by ZF pre-coding decreases the handover rate in the network. Lastly, for both NOMA and NOMA-ZFP schemes, the CSI of all users is required by the corresponding APs. The main difference is that in NOMA-ZFP, CEUs require the CSI of the users in all cells, which requires the exchange of CSI between all APs through the central control unit, involving hence a slight additional latency.

6.4 Chapter summary

In this chapter, two novel hybrid NOMA-ZFP schemes are proposed for multi-cell VLC networks. The proposed schemes are based on using NOMA for handling CCUs while exploiting the MU-MISO structure of the VLC networks with multiple luminaires (acting as APs) to serve CEUs using ZF pre-coding. Using the proposed MA schemes, a relatively small fraction of the total available power at the APs is allocated to CEUs, causing rather low interference on CCUs, and allowing reduced complexity of NOMA signaling for CCUs. These schemes are compared with two available NOMA schemes in the literature considering three MA scenarios with different complexity and irregularity of the user distribution within the cells. The advantages of NOMA-ZFP are demon-

strated in terms of sum-rate (i.e., the upper bound on the total network achievable data rate) and fairness, in particular, in relatively high-SNR regimes.

Among the two proposed hybrid solutions, NOMA-ZFP-B has a much higher computational complexity because of the requirement for convex optimization to compute the pre-coding coefficients \mathbf{W} . NOMA-ZFP-A, however, can be considered to make a good compromise between performance and complexity. Based on the results presented for relatively low and high optical powers, the proposed hybrid schemes can be considered as good candidates for applications using light dimming as they offer a robust performance (in terms of both network fairness and sum-rate) over a wide range of transmit optical powers.

The performance improvement of the proposed hybrid schemes is achieved at the price of an increased overall complexity of the network, as compared to the classical NOMA schemes, since it necessitates the cooperation of the APs (via the central control unit) in handling CEUs. In particular, the CSI of all CEUs should be provided at the APs in order to do pre-coding. In addition, the CSI of all CCUs in the neighboring cells is required for the CEUs to perform SIC to remove the corresponding IUI before detecting their own signal. In order to reduce the computational load at the APs, CSIs of all CCUs and CEUs can be sent from the APs to the central control unit, where the processing of the different users signals will be done. Note that, since CEUs rely on ZF pre-coding for accessing their signals, their performance can be affected by the correlation between the CEUs' channels.

Lastly, for very large indoor spaces, broadcasting the signals for CEUs from all APs does not appear to be efficient. Indeed, APs that are too far from the actual CEU position, will likely have a negligible impact on the user. Therefore, to reduce the network complexity under such conditions, a more appropriate methodology consists of broadcasting the CEUs' signals by only neighboring cell APs. At the same time, the number of "broadcasting APs" should be determined based on the maximum number of CEUs that have to be handled in the network, because for linear ZF pre-coding we have the strict condition that the number of TxS (i.e., APs) should be larger than the number of RxS (i.e., CEUs).

Although the proposed hybrid NOMA-ZFP offered robust ICI mitigation, the number of efficiently handled CEUs is limited by the number of APs, due to the constraints of ZF pre-coding. To handle larger number of CEUs, we propose scheduling of the APs transmission in the next chapter.

Chapter 7

Time-Sliced NOMA for Multi-Cell VLC Networks

Contents

| | |
|---|-----------|
| 7.1 Introduction | 83 |
| 7.2 System model | 85 |
| 7.3 TS-NOMA signaling | 85 |
| 7.3.1 Concept | 85 |
| 7.3.2 TS-NOMA schemes | 87 |
| 7.3.2.1 No dimming, $\delta = 1$ | 87 |
| 7.3.2.2 $\delta > \delta_{\max}$ | 88 |
| 7.3.2.3 $\delta \leq \delta_{\max}$ | 88 |
| 7.3.3 Time-slot fixing strategies | 88 |
| 7.4 Performance analysis | 89 |
| 7.4.1 Main assumptions and considered scenarios | 89 |
| 7.4.2 Numerical results | 90 |
| 7.5 Chapter summary | 93 |

7.1 Introduction

As shown in the previous chapter, although NOMA-ZFP schemes allow an improved network performance, as compared with NOMA, the number of CEUs that can be handled by the network is limited to the number of APs. For larger user densities, and hence, potentially a larger number of CEUs, adequate MA schemes should be designed. We propose in this chapter scheduling of APs' transmission in the NOMA-based VLC network. In the proposed solution, particular attention is also devoted to supporting light dimming.

In fact, as VLC can support both illumination and communication requirements, the possibility of controlling LED illumination by dimming is an important issue. Indeed, light dimming offers the advantages of energy saving and LED heating reduction, hence helping in extending LEDs lifespan [146]. Actually, dimming is an important feature in indoor lighting that allows adapting LED illumination to background luminosity conditions or aesthetic fancies. Note that, human eye perceives the average light intensity [147, 148], where the illumination level impacts the user visual experience and work efficiency [149, 150].

Dimming schemes can be classified to analog (by controlling the illumination level by varying the LED's current) [151, 152], and digital (by varying illumination level by changing the duty cycle of the LED's transmission) [153–155]. Although analog dimming is simpler to realize, digital dimming is preferred as it is less prone to chromaticity shifts, and offers more linearity in controlling light intensity [148]. For NOMA-based VLC networks, dimming solutions have been considered in [48, 156] but the use in multi-cell VLC networks has not been addressed.

As mentioned above, here we consider NOMA as the MA scheme. In NOMA-based VLC networks, there is an obvious need for reducing the number of users in SIC detection. The reason is two fold: (i) the users with high decoding order (i.e., low detection priority) require the CSI of the preceding users; (ii) the users with low decoding order (i.e., high detection priority) suffer from IUI arising from the higher decoding-order users. Our aim in this chapter is to propose a NOMA-based scheme with reduced detection complexity, compared to the conventional NOMA, while enabling efficient ICI mitigation as well as light dimming. These advantages are obtained at the cost of additional synchronization requirements, as will be explained later in this chapter. We call our proposed scheme time-sliced NOMA (TS-NOMA), which adds a temporal dimension to the conventional NOMA. As we will describe in more detail, by TS-NOMA, CCUs and CEUs in a given cell are grouped and handled by NOMA in separate time slots. The duration and the position of these time slots are determined according to the requirements of light dimming and ICI mitigation.

Note that the idea of adding a temporal dimension to NOMA signaling has also been considered for RF networks in a few recent works. For instance, in [157], optimized PA and user scheduling for NOMA were considered for massive IoT networks. In the context of MA mobile edge computing, [158] proposed optimized time allocation for mobile users for offloading their computational workload to edge servers using NOMA signaling. Temporal fair user scheduling was also considered for NOMA signaling in [159]. Compared with these works, our proposed technique differs in considering dimming-compatible duty cycling of NOMA signals for multi-cell VLC networks. Thanks to its relatively low computational complexity, it also facilitates network real-time adaptation in the case of users mobility.

The rest of the chapter is organized as follows: Section 7.2 provides an overview of the system model. Then, we describe the TS-NOMA scheme in Section 7.3, and compare its performance with the conventional NOMA in Section 7.4. Lastly, Section 7.5 concludes the chapter.

7.2 System model

To comply with the light dimming requirement, we set the duty cycle δ of the LED emission to $\delta = \tau/T$, where τ is the transmission time over a certain period T [160]. Denoting by $P_o(t) > 0$ the LED output optical power, we define the dimming ratio γ as:

$$\gamma = \frac{1}{P} \lim_{T \rightarrow \infty} \frac{1}{T} \int_0^T P_o(t) dt, \quad 0 \leq \gamma \leq 1 \quad (7.1)$$

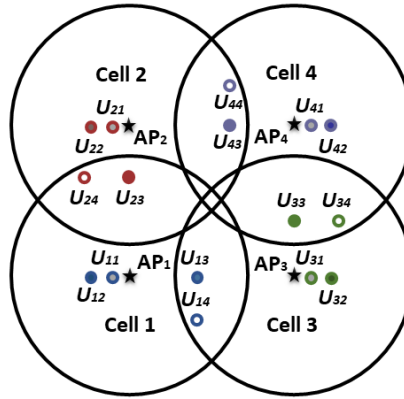
where P is the average LED optical power in the case of no dimming, i.e., for $\gamma = 1$. In fact, the dimming ratio γ (in power domain) is directly proportional to the duty cycle δ (in time domain). Note that such a dimming control by duty cycling the transmitted signal can also be applied to DCO-OFDM signaling [161, 162]. Since in this case, the signal can be modeled as a zero-mean Gaussian random process based on the central limit theorem [163], dimming is mainly controlled by the DC bias.

Throughout this work, we consider NOMA-B signalling scheme (see Subsection 5.2.2), which we refer to as NOMA throughout this chapter for simplicity. In addition, we consider the use of optical concentrator at the Rx side, such that the channel gain is given by equation (2.2).

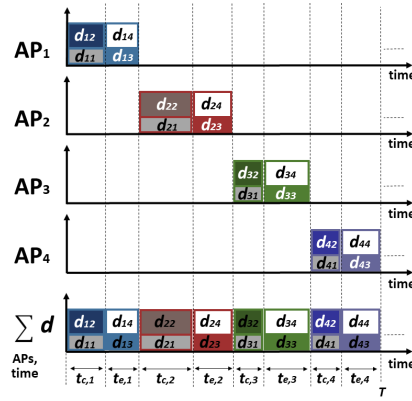
7.3 TS-NOMA signaling

7.3.1 Concept

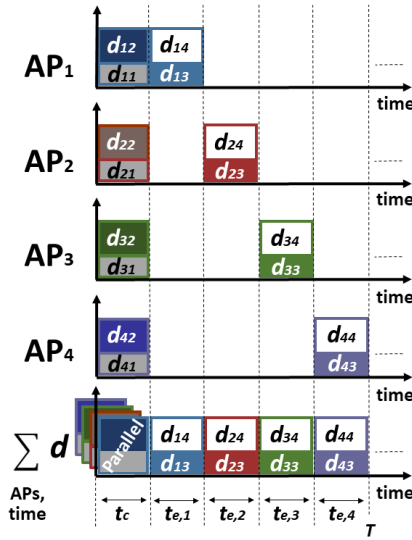
As explained in the introduction, the idea behind TS-NOMA is to adjust the duty cycle of the NOMA signal at the APs to eliminate ICI and to satisfy the light dimming requirement. Firstly, users are classified as CCU or CEU depending on their channel gains, which is done at the central control unit. Afterwards, at each AP, NOMA signaling is applied separately to signals of CEUs and CCUs, which are then transmitted in two different time slots, such that the duty cycle of the total transmission time satisfies the dimming requirement. In addition, APs are coordinated so as to guarantee no ICI, i.e., by transmitting CEU signals in different non-overlapping time slots. To clarify better the idea, consider the example of Fig. 7.1(a) where a 4-cell VLC network is shown with the AP positioned at the center of each cell, and two CCUs within each cell and two CEUs in the intersecting areas of adjacent cells. Note that we define the cell boundaries based on the users' CSI, according to a predefined threshold for channel gain [95], which is set here to 9.74×10^{-7} , corresponding to a cell radius of 2 m. The first TS-NOMA signaling method is illustrated in Fig. 7.1(b), where in addition to separating CEU signals in time, we impose that all CCU signals (from different APs) are sent in non-overlapping time slots. In the second way of TS-NOMA signaling, shown in Fig. 7.1(c), the same time slot is attributed to the CCUs in different cells. We will explain in the next subsection that the choice between these two methods depends on the dimming requirement, i.e., on the parameter δ . In Figs. 7.1(b) and 7.1(c), d_{ij} denotes the signal of user U_{ij} (U_j handled by AP_{*i*}), and $t_{c,i}$ and $t_{e,i}$ refer to the time slots attributed to CCU and CEU groups served by AP_{*i*}, respectively.



(a) Example of 4-cell network



(b) Scheme A



(c) Scheme B

Figure 7.1 — Illustration of the proposed TS-NOMA schemes. (a): top view of a 4-cell network example. (b) and (c): signal transmission timing for different users according to Scheme A and B, respectively.

We denote by c_{int} the number of coordinating APs, having intersecting coverage areas; $c_{\text{int}} = 4$ in the example of Fig. 7.1. To mitigate ICI, the transmission cycle T is divided among the c_{int} APs: each AP disposing of an interval of T/c_{int} for signal transmission, where the maximum duty cycle is $\delta_{\text{max}} = 1/c_{\text{int}}$. Note that, as CCUs are not affected by ICI, their signals could be transmitted in parallel by all the APs, as considered in Fig. 7.1(c). However, in this case, they must use the same $t_{c,i}$, hence having less flexibility, as compared with Fig. 7.1(b).

Let us denote by $N_{c,i}$ and $N_{e,i}$ the number of CCUs and CEUs served by AP_i , respectively. Assuming perfect synchronization, and excluding the DC signal, for CCU_j handled by AP_i over time slot duration $t_{c,i}$, the received AC signal is:

$$\begin{aligned} r_{ij}(t) &= a_{ij} \sqrt{P_e} h_{ij} d_{ij} + \sum_{k=1}^{j-1} a_{ik} \sqrt{P_e} h_{ij} d_{ik} \\ &+ \sum_{k=j+1}^{N_{c,i}} a_{ik} \sqrt{P_e} h_{ij} d_{ik} + z_j. \end{aligned} \quad (7.2)$$

Similarly, for CEU_j served by AP_i in time slot $t_{e,i}$ we have:

$$\begin{aligned} r_{ij}(t) &= a_{ij} \sqrt{P_e} h_{ij} d_{ij} + \sum_{k=1}^{j-1} a_{ik} \sqrt{P_e} h_{ij} d_{ik} \\ &+ \sum_{k=j+1}^{N_{e,i}} a_{ik} \sqrt{P_e} h_{ij} d_{ik} + z_j. \end{aligned} \quad (7.3)$$

For both cases, the corresponding SINR is given by:

$$\text{SINR}_{\text{TS}, U_{ij}} = \frac{h_{ij}^2 P_e a_{ij}^2}{h_{ij}^2 P_e \sum_{k>j} a_{ik}^2 + \sigma_n^2}, \quad (7.4)$$

and the approximate maximum achievable throughput is then:

$$R_{\text{TS}, U_{ij}} = \delta_i \frac{B}{2} \log_2 (1 + \text{SINR}_{\text{TS}, U_{ij}}) \quad (\text{bps}), \quad (7.5)$$

where δ_i is the transmission duty cycle for U_{ij} corresponding to AP_i . Note that, $\delta_i = t_{c,i}/T$ if U_{ij} is a CCU, and $\delta_i = t_{e,i}/T$ if it is a CEU. Also, $(t_{c,i} + t_{e,i})/T = \delta$.

7.3.2 TS-NOMA schemes

We consider three cases for the transmission scheme, depending on all possible values for the duty cycle δ . Note that we reasonably assume the same dimming level for all APs.

7.3.2.1 No dimming, $\delta = 1$

In this case, which results in strongest lighting experience possible, both of Scheme A and B can be used. However, to maximize network capacity, parallel transmission of CCUs signals is preferred,

i.e., by Scheme B, Fig. 7.1(c). Note that, (i) in the intervals where no “signal” is transmitted, the corresponding APs still transmit the DC bias to ensure lighting; (ii) in case where there is no CEU in a cell, the corresponding CEU time slot is devoted to the transmission of CCU signals in all cells; and (iii) the absence of CCUs in a cell does not change the timing in order to avoid ICI with CCU signals from the other cells.

7.3.2.2 $\delta > \delta_{\max}$

In this case, δ that achieves dimming is larger than δ_{\max} that guarantees no ICI, so δ cannot be satisfied by using Scheme A. Using Scheme B, we transmit the signals of CCUs (which do not suffer from ICI) in parallel from all APs. This way, the time intervals for non-overlapping transmission of CEU signals can be increased. We have, $t_{c,i} + \sum_{i=1}^{c_{\text{int}}} t_{e,i} = T$. For simplicity, we consider the same $t_{e,i}$ for all APs. Since for dimming constraint we have $(t_{c,i} + t_{e,i})/T = \delta$, therefore:

$$\begin{cases} \delta_i = (1 - \delta)/(c_{\text{int}} - 1) & \text{for CEUs,} \\ \delta_i = (\delta c_{\text{int}} - 1)/(c_{\text{int}} - 1) & \text{for CCUs.} \end{cases} \quad (7.6)$$

Note, in the absence of CEUs in a cell, the corresponding time slot is used by the CCUs in the same cell to comply with the dimming condition for all APs. If there is no CCU in a cell, the timing is still not changed to avoid ICI with CCU signals from the other cells.

7.3.2.3 $\delta \leq \delta_{\max}$

Here, dimming intensity needed is lower than that in 7.3.2.3, while corresponding δ is achievable by both Schemes A and B. However, as there is no room to increase the network capacity by improving time resources utilization, sequential transmission of CCU signals is preferred, i.e., Scheme A. This allows allocating different durations for $t_{c,i}$, thus more flexibility in timing design. Similar to the previous case, if there is no CEU (CCU) in a cell, the corresponding time slot is used by the CCUs (CEUs) in the same cell.

7.3.3 Time-slot fixing strategies

For setting the different time intervals $t_{c,i}$ and $t_{e,i}$ for CCUs and CEUs, we consider six specific strategies that we will refer to as S1 to S6, as described in the following.

1. TS-NOMA-S1: As the simplest way, for all i , we use equal time slots, i.e., $t_{c,i} = t_{e,i}$, for all i . For the scheme in Fig. 7.1(c), starting from $t_{c,i} + \sum_{i=1}^{c_{\text{int}}} t_{e,i} = T$, $t_{c,i}$ and $t_{e,i}$ are given by $(T/(c_{\text{int}} + 1))$.
2. TS-NOMA-S2: We set slot durations according to the associated number of users. For Scheme A, Fig. 7.1(b), this results in $t_{c,i} = N_{c,i}/N_i$ and $t_{e,i} = N_{e,i}/N_i$. For Scheme B, Fig. 7.1(c), $t_{e,i}$ is determined by $N_{e,i}$, whereas t_c is set considering the maximum number of CCUs $N_{c,\max}$ per group among all CCU groups, i.e., $N_{c,\max} = \max(N_{c,1}, \dots, N_{c,N_t})$. This ensures setting the

largest possible t_c . We have then $t_c = N_{c,\max}/(N_{c,\max} + \sum_{i=1}^{N_t} N_{e,i})$ and $t_{e,i} = N_{e,i}/(N_{c,\max} + \sum_{i=1}^{N_t} N_{e,i})$.

3. TS-NOMA-S3: We set $t_{c,i}$ and $t_{e,i}$ according to the average channel gain for each group of CCUs and CEUs (similar to the idea of static PA in NOMA [138]). This way, for a larger average channel gain, we allocate a smaller duration to the corresponding time slot. The ratio between each two consecutive time slots ζ is a constant, called time allocation (TA) coefficient. This allows time slot allocation to be better tailored to the channel gains in every group. For Scheme B, t_c is set by considering the minimum average channel gain per group (among all CCU groups), to ensure the largest possible t_c .
4. TS-NOMA-S4: Setting slot duration is based on the same approach as in TS-NOMA-S3, while considering as criterion the average channel gain divided by the number of users in the group. This allows groups with a large number of users to be allocated a long time slot, hence, resulting in a still better fairness in the network.
5. TS-NOMA-S5: This strategy applies to the case of $\delta > \delta_{\max}$, where we use (7.6) to calculate $t_{c,i}$ and $t_{e,i}$, to satisfy dimming and mitigate ICI.
6. TS-NOMA-S6: For the case of $\delta \leq \delta_{\max}$, users are served as in conventional NOMA, while avoiding parallel transmission of APs (i.e., to avoid ICI).

Note that the described strategies should be selected depending on the required dimming, or in other words, δ . For $\delta = 1$, TS-NOMA-S1, -S2, -S3, and -S4 can be used. For $\delta \leq \delta_{\max}$, these four strategies, as well as TS-NOMA-S6 can be used where $t_{c,i}$ and $t_{e,i}$ are calculated separately in each cell. For $\delta > \delta_{\max}$, only TS-NOMA-S5 can be used. In fact, TS-NOMA-S1 to -S4 do not satisfy the constraints of dimming and ICI mitigation in this case, and therefore cannot be used.

7.4 Performance analysis

Here, we compare the performance of the proposed scheme with conventional NOMA for a set of network configurations.

7.4.1 Main assumptions and considered scenarios

We consider a 4-cell network, as in Fig. 7.1(a), with different number of CCUs and CEUs in the cells. APs are positioned at the center of the cells and the emitted optical power from each AP is set to $P_o = 1.584$ W as in [74]. The considered heights of the APs and the RxS are 2.5 and 0.85 m, respectively. Three different scenarios are considered, called Scenarios 1, 2, and 3, for which we set N_r to 8, 12, and 16, and the corresponding number of CEUs to 4, 4, and 8, respectively. These represent an increased level of IUI and ICI in the case of conventional NOMA. For each scenario,

Table 7.1 — Simulation parameters.

| Parameter | Value |
|--|---|
| Room dimension | $(7 \text{ m} \times 7 \text{ m} \times 3 \text{ m}) \text{ m}^3$ |
| LED luminaire Lamertian order m | 1 |
| Number of LED chips per luminaire | 36 [72] |
| LED conversion efficiency S | 0.44 W/A [72] |
| PD responsivity R | 0.4 A/W [47] |
| PD area | 1 cm^2 [69] |
| Rx FOV | 62° [69] |
| Refractive index of optical concentrator | 1.5 [69] |
| System bandwidth B | 10 MHz |
| Equivalent Rx noise power spectral density | $10^{-21} \text{ A}^2/\text{Hz}$ [47] |

200 randomly generated users positions are used and the performance is averaged over these realizations.¹ Table 7.1 summarizes the simulation parameters. α is set to 0.3, which provides the best compromise between sum-rate and FI. The same value is adopted for ζ .

7.4.2 Numerical results

We have compared the sum-rate and FI performances of TS-NOMA and conventional NOMA in Fig. 7.2 for the case of no dimming, i.e., $\delta = 1$, over the three considered scenarios described in Subsection 7.4.1. We notice that, despite the ICI mitigation merits of TS-NOMA, NOMA achieves a better sum-rate, except for TS-NOMA-S4 case, which has a close performance to NOMA. The reason is that TS-NOMA-S1, -S2, and -S3 schemes have a poor sum-rate performance when a relatively large number of users are in a group, where they are allocated a relatively short time slot. The TS-NOMA-S4 strategy avoids such conditions, as described above, which results in a higher average sum-rate. As concerns FI, we notice from Fig. 7.2(b) that generally TS-NOMA schemes outperform conventional NOMA, except for TS-NOMA-S3, and for TS-NOMA-S4 in Scenario 3. The best FI are obtained for TS-NOMA-S1 and -S2, which was expected: the former equally divides the time resources among the users, whereas the latter allocates them based on the number of users in each group. For TS-NOMA-S3 and S4, FI is penalized by the large variations in the time slot duration, even for very small differences between consecutive groups, which is due to considering a constant TA coefficient here.

Overall, compared with the conventional NOMA, the presented results suggest TS-NOMA-S4 as the most appropriate scheme that makes a good compromise between sum-rate and FI, and allows

¹Note that we exclude in the simulations those scenarios for which CEUs are in coverage areas of more than two APs. Indeed, for such cases, the NOMA performance will be penalized considerably because of ICI, in contrary to TS-NOMA where CEUs of each AP are served in non-overlapping time slots

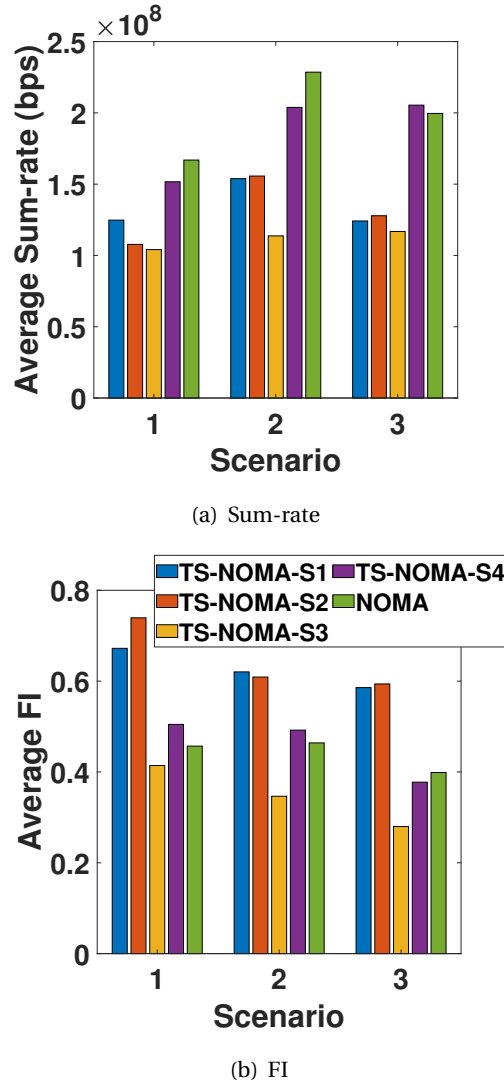


Figure 7.2 — Comparison of sum-rate and FI for TS-NOMA and NOMA for the case of no dimming ($\delta = 1$).

a reduced Rx complexity compared with conventional NOMA due to the decreased number of SIC detection steps.

Finally, Fig. 7.3 compares TS-NOMA and NOMA over sum-rate and FI, for $\delta < 1$, namely 70%, 50%, 30%, and 25% for the three considered scenarios. Given that $\delta_{\max} = 1/4$, for the three former cases where $\delta > \delta_{\max}$, we use the TS-NOMA-S5 strategy, whereas for the last case where $\delta = \delta_{\max}$, we use TS-NOMA-S4 (which achieved the best sum-rate and acceptable FI in Fig. 7.2) and TS-NOMA-S6. We notice from Figs. 7.3 (a), (b), and (c) that TS-NOMA-S5 outperforms NOMA in both sum-rate and FI in all scenarios. This superiority of TS-NOMA-S5 can be explained by the decreased IUI due to handling a smaller number of NOMA users per time interval, and the elimination of ICI. Similarly, from Fig. 7.3 (d) we notice a better sum-rate and FI for TS-NOMA-S4 and -S6, compared to conventional NOMA, due to minimized ICI. Although TS-NOMA-S6 achieves a

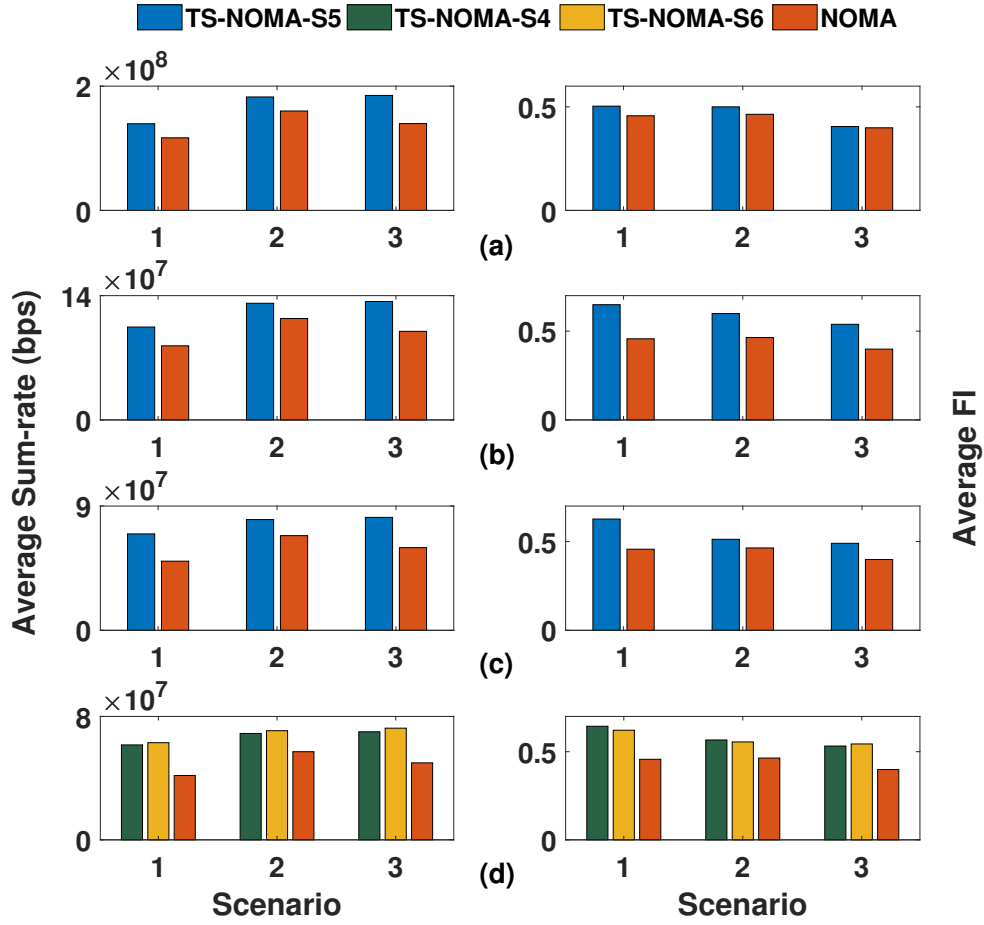


Figure 7.3—Comparison of sum-rate and FI between TS-NOMA and NOMA for (a) $\delta = 70\%$, (b) 50%, (c) 30%, and (d) 25%.

higher sum-rate than TS-NOMA-S4 because of allocating more time resources per user, it needs the same number of SIC detection steps as for conventional NOMA. Overall, compared with conventional NOMA, we can conclude TS-NOMA-S4 and -S5 as the most appropriate schemes for $\delta \leq \delta_{\max}$ and $\delta > \delta_{\max}$, respectively, providing improved sum-rate and FI, as well as reduced Rx complexity.

Note also that for all TS-NOMA schemes in Fig. 7.3, we notice a degradation of FI from Scenario 1 to 3 (from the smallest to the largest number of users), which is because of increased IUI. In addition, we note an increase in the average sum-rate for scenarios with a larger number of users. Yet, the increase in sum-rate from Scenario 2 to 3 is less significant than that from Scenario 1 to 2. This is due to the decrease in the available time resources per user.

7.5 Chapter summary

For the case of multi-cell VLC networks, we proposed the TS-NOMA scheme and showed its efficiency in handling MUI, compared with the conventional NOMA. By separating CCUs and CEUs in different NOMA groups in the time domain, the proposed scheme offers ICI mitigation, dimming compatibility, as well as reduction in the number of users handled by NOMA per time interval (which decreases the average number of SIC detection steps needed at the RxS). We showed the advantage of TS-NOMA over the conventional NOMA in terms of sum-rate and network fairness, especially for the case of light dimming.

The performance gain of TS-NOMA compared to NOMA comes at the price of a low additional synchronization requirement, since only two time slots are to be handled per AP. Also, the required user grouping and time-slot setting for different groups in TS-NOMA, which should be done at the central control unit, increases slightly the network complexity. Nevertheless, this is quite justified, given the improvement achieved in the network performance.

Although MA techniques offer flexibility in handling a large number of users, frequent user-link interruptions could occur due to handovers associated with user transitions between cells. We propose in the next chapter a handover-aware scheduling solution to address the problems associated with user mobility in multi-cell networks.

Chapter 8

Addressing User Handover in Multi-Cell VLC Networks

Contents

| | |
|---|------------|
| 8.1 Introduction | 95 |
| 8.2 Handover-aware scheduling | 97 |
| 8.2.1 Single cluster network | 97 |
| 8.2.2 Multiple cluster network | 101 |
| 8.3 Time scheduling strategies study | 104 |
| 8.3.1 Time scheduling strategies | 105 |
| 8.3.1.1 Single cluster | 105 |
| 8.3.1.2 Multiple clusters | 105 |
| 8.4 Performance analysis | 105 |
| 8.4.1 Main assumptions and considered scenarios | 105 |
| 8.4.2 Numerical results | 106 |
| 8.5 Chapter summary | 110 |

8.1 Introduction

One of the challenges associated with MA management in multi-cell VLC networks is to maintain the user connection during transitions between cells, for which efficient handover techniques should be designed. In general, two types of handover are considered: vertical, i.e., handover between APs of different wireless access technologies, and horizontal, i.e., handover between APs using the same wireless access technology [164, 165]. We consider horizontal handover here, which we refer to as “handover” for simplicity. Due to the limited illumination area of the LEDs, which constraints the cell size, frequent handovers may be required in the VLC for mobile users. As the

area of the communication environment (and hence the number of APs) and/or the user mobility increase, the handover rate increases. Generally, handover algorithms can be classified into “soft” and “hard” handover schemes. In the former, the user establishes data connection with the new AP before breaking the connection with the current AP, to avoid connection disruptions. On the other hand, users in hard handover break connection with the current AP before connecting to the new AP. Of course, the adoption of soft or hard handover is related to the resource utilization in the MA techniques.

Handover management in VLC networks has been receiving increasing attention, due to the potentially high data-rate connections and the impact of handover algorithms on the network performance [166]. In [167], handover was studied for cases of overlapping and non-overlapping cells in the VLC network, while [168] investigated handover modelling while accounting for Rx mobility and orientation. In [169], coverage areas of APs were controlled to improve handover efficiency and user distribution in cells. Also, to reduce handover rate, handover skipping was proposed in [170], which used a reference value and the rate of change of received signal power to mitigate unnecessary handovers. Soft handover solutions were proposed in [171, 172] but the efficiency of resource utilization was not considered.

In this chapter, we propose efficient soft handover solutions allowing an improved network sum-rate performance based on efficient resource utilization and coordinated transmissions by the APs. For this, appropriate solutions are developed for small/medium scale and large scale scenarios. For small and medium -scale VLC networks, we propose scheduling the transmissions of the APs, based on the locations of the Rxs with respect to the AP coverage areas. In particular, by considering the intersection areas between the APs, and selecting the areas where the APs can achieve interference-free simultaneous transmissions, we maximize the resource utilization to improve the network sum-rate performance. We will call this scheme handover-aware scheduling. For large-scale VLC networks, we extend the proposed scheme to multiple cluster VLC networks, where each cluster is composed of APs that broadcast the user signals within the coverage area of the cluster, to decrease the handover rate associated with possible increased mobility. There, given the larger intersection areas between the clusters, careful resource management is considered to maximize the resource utilization. Compared with the conventional non-scheduling based schemes, we show that our proposed handover-aware scheduling scheme offers improved sum-rate and connection reliability.

The rest of this chapter is organized as follows: Section 8.2 explains the proposed handover-aware scheduling for small/medium -scale and large-scale VLC networks, and Section 8.3 explains the considered scheduling strategies. Then Section 8.4 presents the performance analysis, and Section 8.5 concludes the chapter.

8.2 Handover-aware scheduling

To describe the proposed handover-aware scheduling, we consider two cases of single cluster and multiple cluster VLC networks. In the former case, the ensemble of APs is considered as a single cluster, in which APs transmit signals to their users. For the multiple clusters case, each group (cluster) of APs broadcast the same signals to the users within the coverage area of the cluster.

8.2.1 Single cluster network

In this case, the central control unit manages the scheduling of the transmission of each AP in multiple time slots, to mitigate interference, maximize resource utilization, and ensure soft handover, which is illustrated in detail in Fig. 8.1 that considers a 4-cell VLC network. As shown in Fig. 8.1(a), time slots allocated to the users are set based on their locations with respect to the APs. In the blue time slot, all CCUs are handled simultaneously, as they are not affected by ICI. CEUs, on the other hand, are served in three separate time slots (red, green, and yellow), where the users data in such groups are broadcast by more than one AP, generating joint transmission for the CEUs, while avoiding ICI. For the red and the green time slots, each AP pair serve their users simultaneously, to maximize the network resource utilization, and maximize the network sum-rate. On the other hand, Fig. 8.1(b) illustrates the handover decision for non-scheduling based schemes. As shown, when a user served by an AP (i.e., host AP, denoted by AP-H) starts to be in the coverage area of a new AP (i.e., target AP, denoted by AP-T), it compares the strength of the received signals from both AP-H and AP-T. When the received power from AP-T, denoted by $P-T$, is larger than that received from AP-H, denoted by $P-H$, by value equal to the handover margin (HOM) over a continuous duration equal to the time-to-trigger (TTT), handover to AP-T is initiated. The time needed to transfer the user and to start receiving data from the new AP is referred to as handover overhead delay, which we refer to as "handover delay" for simplicity. Note that, by this approach the user receives no data during the handover delay.

We have shown in Fig. 8.1(c) flowcharts for the proposed handover scheme and the conventional (non-scheduling) approach. For the proposed scheduling scheme, starting with the case of handling a CCU in coverage area of AP-H, when the user moves to a new location where it is within the coverage areas of AP-T and AP-H, handover is initiated, and the user data is moved to a new time slot, corresponding to the new location of the user (i.e., a CEU time slot in the mentioned case). By benefiting from the joint transmission in the cell-edge areas in the proposed scheme, the user remains connected with AP-H during the handover delay, which ensures reliable connection for the user. After the handover delay, the user is served by both AP-H and AP-T in the new time slot. Following this, in the case the user keeps moving towards AP-T, ending up as a CCU within the coverage area of AP-T, the user data is moved to a CCU time slot, and no handover is needed, as the user data are already handled by AP-T.

To show how both of the scheduling and non-scheduling based schemes operate in different situations within the VLC network, we show in Fig. 8.2 a step by step evolution for the user data

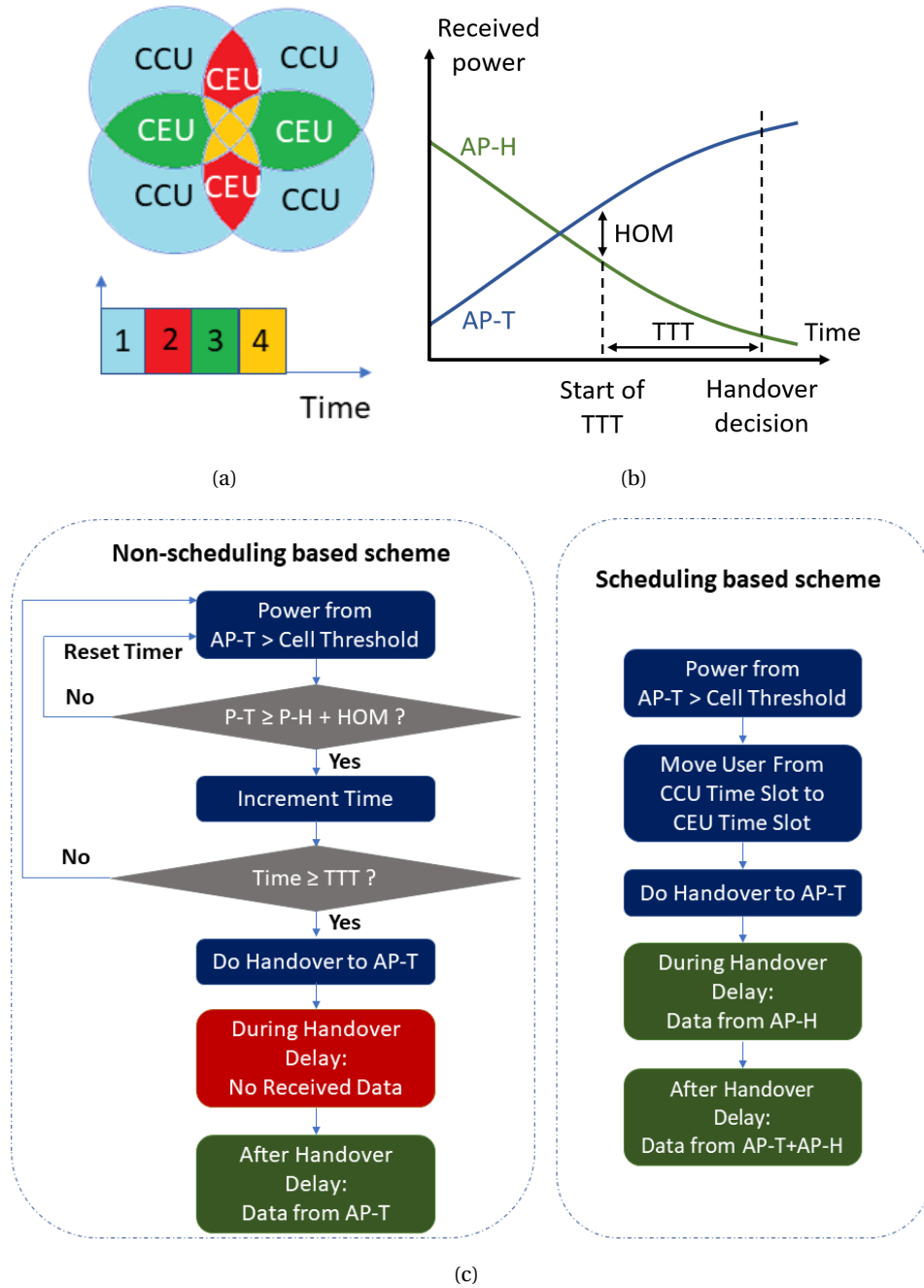


Figure 8.1 — (a) Top view for AP coverage areas distributions for the proposed handover-aware scheduling and the corresponding resource utilization, (b) illustration for the handover decision for non-scheduling based handover, and (c) flowcharts of procedures of non-scheduling and scheduling-based handover approaches.

handling during different handover-related situations, we specifically consider the so called ping-pong effect, where user moves to a new cell then moves back after short time to the old cell, and the short cell dwell time, where user arrives for short time in a cell, before moving to a new cell.

Cells H and T correspond to coverage areas of AP-H and AP-T, respectively.

Steps 1 to 5 in Fig. 8.2 show the handover steps for a CCU moving to a cell-edge area. Firstly, the CCU is handled by AP-H, before moving in the second step to the area at the intersection of AP-H and AP-T coverage. There, in case of non-scheduling based handover, it starts to check satisfying the handover condition, while receiving data from AP-H. After satisfying the condition $P-T \geq P-H + \text{HOM}$ over TTT in step 4, handover is initiated to AP-T, the user is disconnected from AP-H, and starts to receive data from AP-T only after the handover delay (step 5), which results in a link interruption during step 4. On the other hand, for the case of the proposed scheduling based scheme, the user data is firstly handled in CCU time slot in step 1. Following the user transfer to cell-edge area in step 2, handover is initiated to AP-T while keeping the connection with AP-H, and user data is handled in a CEU time slot. Note, during handover delay to AP-T, the user receives data from AP-H, resulting in no link interruptions. After the handover delay, the user is jointly served by AP-H and AP-T in the CEU time slot.

Following step 5, we assume 4 possibilities for the user movement in parts (I), (II), (III), and (IV). In case (I), the user moves to the cell-centre area of AP-T. In case of using the non-scheduling based scheme, the user is already handled by AP-T, whereas for the scheduling-based scheme, the user data is handled in a CCU time slot by AP-T. In case of (II) which is an example of ping-pong effect, the user stays within the cell-edge area, while moving towards AP-H (step II.1), where for the non-scheduling based scheme, if $P-H \geq P-T + \text{HOM}$ over TTT, handover is initiated to AP-H, and the user terminates the connection with AP-T (step II.2), and starts to receive data from AP-H after the handover delay (step II.3), resulting in link interruption. On the other hand, in the case of scheduling based scheme, no change occurs for the user data handling, which is carried out by both AP-H and AP-T in a CEU time slot.

If the user moves with a higher pace towards AP-H cell-centre area resulting in no coverage from AP-T before performing a handover to AP-H, as shown in case (III), more severe link interruptions occur in case of no scheduling. This is because the user has to wait before receiving data from AP-H (step III.3) for satisfying the handover received power condition over TTT (step III.1) and for the handover delay after starting the handover (step III.2). On the other hand, for the scheduling based scheme, the user data will be moved to a CCU time slot, while experiencing no link interruption, as the connection to AP-H is already established. For the case of short cell dwell-time, illustrated in step (IV), TN corresponds to cell of the new target AP (AP-TN), and P-TN corresponds to the power received from AP-TN. In this case, the user moves from AP-T to AP-TN within short time of establishing the handover (step IV.1). There, for the case of no scheduling, the user has to terminate the link with AP-T after satisfying the handover condition $P-TN \geq P-T + \text{HOM}$ over TTT (step IV.2), and to wait for handover delay before starting data reception from AP-TN (step IV.3). For the case of scheduling based scheme, handover is initiated to AP-TN while keeping the connection with AP-T, and the user data is served in a CEU time slot. After the handover delay, the user is jointly served by AP-T and AP-TN.

The figure illustrates the advantages of the proposed handover-aware scheduling in terms of

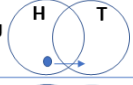
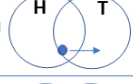
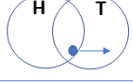
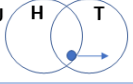






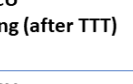




| | No Scheduling | Scheduling |
|--|--|--|
| 1.CCU  | CCU \rightarrow AP-H | 1- CCU time slot 2- CCU \rightarrow AP-H |
| 2.CEU  | 1- $P-T < P-H + HOM$ 2- CEU \rightarrow AP-H | 1- $P-T > P-(\text{Cell Threshold})$ 2- CEU time slot, HO to AP-T 3- CEU \rightarrow AP-H |
| 3.CEU  | 1- $P-T \geq P-H + HOM$ 2- Wait for TTT 3- CEU \rightarrow AP-H | 1- $P-T > P-(\text{Cell Threshold})$ 2- After handover delay: 3- CEU \rightarrow AP-H + AP-T |
| 4. CEU (After TTT)  | 1- $P-T \geq P-H + HOM$ 2- HO to AP-T 3- No data | 1- CEU time slot 2- CEU \rightarrow AP-H + AP-T |
| 5.CEU  | 1- After handover delay: 2- CEU \rightarrow AP-T | 1- CEU time slot 2- CEU \rightarrow AP-H + AP-T |
| (I) CCU  | 1- CCU \rightarrow AP-T | 1- CCU time slot 2- CCU \rightarrow AP-T |
| (II.1) CEU Ping-Pong  | 1- $P-H \geq P-T + HOM$ 2- Wait for TTT 3- CEU \rightarrow AP-T | 1- CEU time slot 2- CEU \rightarrow AP-H + AP-T |
| (II.2) CEU Ping-Pong (after TTT)  | 1- $P-H \geq P-T + HOM$ 2- HO to AP-H 3- No data | 1- CEU time slot 2- CEU \rightarrow AP-H + AP-T |
| (III.3) CEU Ping-Pong (after TTT)  | 1- After handover delay: 2- CCU \rightarrow AP-H | 1- CEU time slot 2- CEU \rightarrow AP-H + AP-T |
| (III.1) CCU Ping-Pong  | 1- $P-H \geq P-T + HOM$ 2- Wait for TTT 3- No data | 1- CCU time slot 2- CCU \rightarrow AP-H |
| (III.2) CCU Ping-Pong (after TTT)  | 1- $P-H \geq P-T + HOM$ 2- HO to AP-H 3- No data | 1- CCU time slot 2- CCU \rightarrow AP-H |
| (III.3) CCU Ping-Pong (after TTT)  | 1- After handover delay: 2- CCU \rightarrow AP-H | 1- CCU time slot 2- CCU \rightarrow AP-H |
| (IV.1) CEU Short Cell Dwell-Time  | 1- $P-TN \geq P-T + HOM$ 2- Wait for TTT 3- CEU \rightarrow AP-T | 1- New CEU time slot 2- CEU time slot, HO to AP-T 3- CEU \rightarrow AP-H + AP-T |
| (IV.2) CEU (after TTT) Short Cell Dwell-Time  | 1- $P-TN \geq P-T + HOM$ 2- HO to AP-TN 3- No data | 1- New CEU time slot 2- After handover Delay: 3- CEU \rightarrow AP-T + AP-TN |
| (IV.3) CEU (after TTT) Short Cell Dwell-Time  | 1- After handover delay: 2- CEU \rightarrow AP-TN | 1- New CEU time slot 2- CEU \rightarrow AP-T + AP-TN |

Figure 8.2 — A step by step comparison between non-scheduling and scheduling based handover approaches over different scenarios.

link reliability compared with the non-scheduling based scheme, by benefiting from the joint transmission by the APs covering the intersection areas between cells.

For transmitted electrical power per AP of P_e , and noise variance at the Rx of σ_n^2 , the SNR for

R_{x_j} is given by:

$$\text{SNR}_{R_{x_j}} = \frac{\sum_{i=1}^{N_t} h_{ij}^2 P_e}{\sigma_n^2}, \quad (8.1)$$

where $h_{ij} = 0$ if R_{x_j} is not within the coverage area of AP_i , and the achievable throughput if R_{x_j} is served in time slot of size t , over transmission period T is then:

$$R_{R_{x_j}} = \frac{t}{T} \frac{B}{2} \log_2 (1 + \text{SNR}_{R_{x_j}}) \quad (\text{bps}), \quad (8.2)$$

where B is the link bandwidth, and the division by 2 due to assuming DCO-OFDM signalling.

8.2.2 Multiple cluster network

For large communication areas (e.g., airports, large exhibition halls, or industrial scenarios), handling of handover becomes more critical, due to higher user mobilities and larger number of users. To benefit from the considered centralized architecture of the VLC networks, where a central control unit is connected to all the APs and carries out most of the computation and synchronization operations, one interesting solution is handling multiple APs as a cluster. In particular, within a cluster, all APs broadcast the signals to the corresponding users. This can be done by broadcasting the same signal, or otherwise by ZF pre-coding of the users signals if the number of Rxs in the cluster does not exceed the number of APs. This approach eliminates the need to handle intra-cluster handovers, which decreases the complexity of the network and the handover rate. However, by considering this approach, it is still required to manage inter-cluster handovers, which can be realized by the same handover approach described above for the case of single cluster networks. To further exploit the centralized architecture in the VLC networks, while ensuring soft handovers, we extend the proposed handover-aware scheduling to the case of multiple cluster networks. Figure 8.3 shows an illustration of the proposed scheme over a 16 AP network, where each 4 APs are grouped into a main cluster (denoted by Clusters 1, 2, 3, and 4) so as to result in the same AP density per cluster.

To achieve soft handover, we propose forming *transition clusters* using the same APs (Clusters A, B, C, D, and E), to serve the users in multiple time slots in the network. Similar to the single cluster case approach, the time slots are distributed based on the locations of the users with respect to the cluster coverage areas. To maximize resource utilization, and minimize inter-cluster interference, a time slot is allocated for main clusters to serve their users simultaneously, and time slots are allocated to the transition clusters, where cluster groups using the same time slots serve their users simultaneously. In contrast to the single cluster case, due to more intersections between the coverage areas of the clusters, and the control of the transmission of each AP in the cluster, users can be served in more than one time slot (time slots of main and transitional clusters), as shown in the right side of the Fig. 8.3. For example, users in the upper right corner of Cluster 1 are in the coverage areas of Clusters A, C, E, and may exist in the coverage areas of Clusters B, D. To simplify the demonstration of the possible associated time slots for the users in each AP, the right side of Fig. 8.3 presents the time slot associations for each AP coverage area, assuming that the blue time

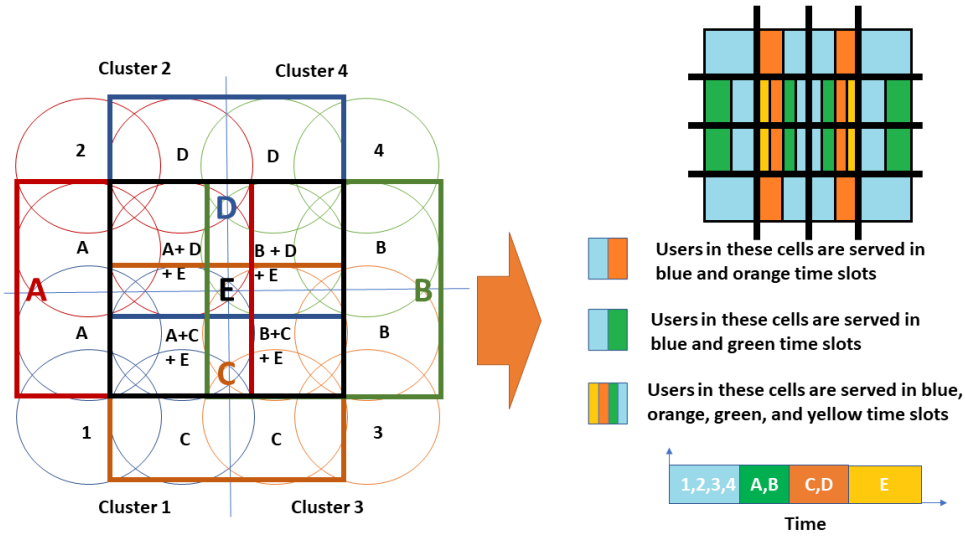


Figure 8.3 — Illustration for the cluster formation, and the corresponding resource utilization for the proposed handover-aware scheduling in case of multiple clusters.

slot is used by the main Clusters, the green time slot is used by Clusters A and B, the orange time slot is used by Clusters C and D, and lastly, the yellow time slot is used by the central Cluster E. However, it should be noted that due to the large intersection between transition clusters, careful management of the user associations is needed. To avoid inter-cluster interference, users who are in the coverage area of two transitional clusters that use the same time slot are not served by any of them. In particular, users who are covered by two main clusters can only be served in either orange or green time slots. For example, see Fig. 8.3, a user in the intersection area between Clusters 1 and 2 could be located in the coverage areas of Clusters C and D, which simultaneously use the orange time slot, resulting in inter-cluster interference in the case of the user being served in the orange time slot. Similarly, users covered by more than two main clusters can only be served in the yellow time slot, as serving them in either blue, green, or orange time slots would result in inter-cluster interference.

To show the operation of the scheduling and non-scheduling based handover schemes in case of multiple clusters, we show in Fig. 8.4 a step by step evolution for the user data handling during different handover-related situations, such as ping-pong. Steps 1 to 7 show the procedures corresponding to the movement of a user (yellow spot in the figure) from the host cluster (C-H), which is blue coloured, to the final cluster (C-F), which is red coloured. For the case of conventional handover, similar to case of single cluster, the handover is carried out to C-F after the power from C-F (denoted by P-CF) exceeds the power from C-H (denoted by P-CH) by a HOM, over a TTT. On the other hand, by the proposed handover-aware scheduling, soft handover is achieved by handling the user using the green coloured transitional cluster (C-T), before arriving at C-F. Firstly, the user is handled by C-H, and moves towards C-F, as shown in step 1. For case of no scheduling, when user is located within the coverage area of Cluster C-F, it remains handled by C-H until satisfying the power and time handover conditions (steps 2 and 3). After satisfying the condition $P\text{-CF} \geq$

P-CH + HOM over TTT (step 4), the user disconnects from C-H, and handover is initiated to C-F, where user starts receiving data from C-F after handover delay (step 5), which causes link interruption. For the case of the scheduling-based scheme, due to deployment of transition clusters, the user exists in the coverage areas of the blue cluster C-H (which is considered as a main cluster) and the green cluster C-T, so that it is served in their associated blue and green time slots (see Fig. 8.3). Following the movement of the user towards the red cluster C-F (which is considered also as a main cluster), it passes by the intersection area between C-H and C-F, where it is served only by C-T to avoid inter-cluster interference. After the user moves totally outside C-H, and arrives in C-F (step 6), handover is initiated to handle the user in C-F, where during the handover delay the user is served only by C-T. After the handover delay, the user is served in the blue time slot by C-F and in the green time slot by C-T (step 7).

Following step 7, we assume 2 possibilities for ping-pong effect in parts (I), (II), where the user moves back to intersection area between C-H and C-F and totally out of coverage area of C-F, respectively. In case (I), using the non-scheduling based approach, the user remains connected to C-F until satisfying the handover condition $P\text{-CF} \geq P\text{-CH} + \text{HOM over TTT}$, after which handover is initiated to C-H (step I.2). After handover delay, the user starts receiving data from C-H (step I.3). On the other hand, using the scheduling based approach, the user is served only by C-T, as it is remaining in the intersection area between two main clusters. For case (II), where the user moves totally to C-H before initiating the handover to C-H, by using the non-scheduling based scheme, the user experiences more severe link interruption occurs than in case (I), as it has to wait for satisfying the handover power and time conditions, in addition to the handover delay, before starting to receive data from C-H. For the scheduling based scheme, the user starts handover to C-H, while being served by C-T during the handover delay. After the handover delay the user is served by both C-H and C-T in the blue and the green time slots, respectively.

The figure illustrates the advantages of the proposed handover-aware scheduling in terms of link reliability compared with the non-scheduling based scheme, benefiting from the deployment of multiple intersecting clusters to offer transmission in multiple time slots.

Lets denote the total number of clusters by K . For Rx_j served by the k^{th} cluster which is allocated time slot t_k over period T , the SNR is calculated as:

$$\text{SNR}_{\text{Rx}_{jk}} = \frac{\sum_{i=1}^{N_t} h_{ij}^2 P_e}{\sigma_n^2}, \quad (8.3)$$

where $h_{ij} = 0$ if AP_i is not included in cluster k . The achievable throughput for Rx_j is then given by:

$$R_{\text{Rx}_j} = \sum_{k=1}^K \frac{t_k}{T} \frac{B}{2} \log_2 (1 + \text{SNR}_{\text{Rx}_{jk}}) \quad (\text{bps}), \quad (8.4)$$

where $\text{SNR}_{\text{Rx}_{jk}} = 0$ if Rx_j is not handled by cluster k .


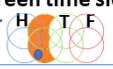
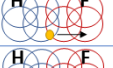

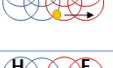
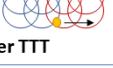






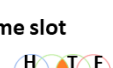

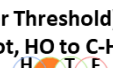
| | No Scheduling | Scheduling |
|---|---|--|
| 1.  | Rx \rightarrow C-H | 1- Rx in Blue + Green time slot 2- Rx \rightarrow C-H + C-T  |
| 2.  | 1- P-F < P-H + HOM 2- Rx \rightarrow C-H | 1- Rx in Green time slot 2- Rx \rightarrow C-T  |
| 3.  | 1- P-F \geq P-H + HOM 2- Wait for TTT 3- Rx \rightarrow C-H | 1- Rx in Green time slot 2- Rx \rightarrow C-T |
| 4.  | 1- P-F \geq P-H + HOM 2- HO to C-F 3- No data | 1- Rx in Green time slot 2- Rx \rightarrow C-T |
| After TTT | | |
| 5.  | 1- After handover delay: 2- Rx \rightarrow C-F | 1- Rx in Green time slot 2- Rx \rightarrow C-T |
| 6.  | 1- Rx \rightarrow C-F | 1- P-F > P-(Cluster Threshold) 2- Green time slot, HO to C-F 3- Rx \rightarrow C-T  |
| 7.  | 1- Rx \rightarrow C-F | 1- After handover delay: 2- Rx in Green + Blue time slot 3- Rx \rightarrow C-T + C-F |
| 8.  | 1- Rx \rightarrow C-F | 1- Rx in Green + Blue time slot 2- Rx \rightarrow C-T + C-F |
| (I.1) Case A Ping-Pong  | 1- P-H \geq P-F + HOM 2- Wait for TTT 3- Rx \rightarrow C-F | 1- Rx in Green time slot 2- Rx \rightarrow C-T  |
| (I.2) Case A Ping-Pong (after TTT) | 1- P-H \geq P-F + HOM 2- HO to C-H 3- No data | 1- Rx in Green time slot 2- Rx \rightarrow C-T |
| (I.3) Case A Ping-Pong (after TTT) | 1- After handover delay: 2- Rx \rightarrow C-H | 1- Rx in Green time slot 2- Rx \rightarrow C-T |
| (II.1) Case B Ping-Pong  | 1- P-H \geq P-F + HOM 2- Wait for TTT 3- No data | 1- P-H > P-(Cluster Threshold) 2- Green time slot, HO to C-H 3- Rx \rightarrow C-T  |
| (II.2) Case B Ping-Pong (after TTT) | 1- P-H \geq P-F + HOM 2- HO to C-H 3- No data | 1- After handover delay: 2- Rx in Green + Blue time slot 3- Rx \rightarrow C-T + C-H |
| (II.3) Case B Ping-Pong (after TTT) | 1- After handover delay: 2- Rx \rightarrow C-H | 1- Rx in Green + Blue time slot 2- Rx \rightarrow C-T + C-H |

Figure 8.4 — A step by step comparison between scheduling and non-scheduling based handover over different scenarios in case of multiple clusters.

8.3 Time scheduling strategies study

To study the performance of the proposed handover-aware scheduling compared with the non-scheduling based schemes, we start by explaining the strategies considered for calculating the time slot size.

8.3.1 Time scheduling strategies

8.3.1.1 Single cluster

Here we consider three time scheduling strategies as described in the following:

- Scheduling-S1: Here, the time slot fraction with respect to signal transmission period is fixed to the average number of users that are served in the time slot, divided by the summation of the average number of users in all the time slots.
- Scheduling-S2: By this approach, the time slot fraction is fixed using the same criterion in Scheduling-S1, while considering the corresponding maximum number of users (instead of average number of users).
- Scheduling-S3: Here, the time slot fraction is set to the sum of users handled in the time slot divided by the total number of users in the network.

8.3.1.2 Multiple clusters

Similar to the single cluster case, we consider three scheduling strategies as follows:

- Scheduling-S4: Here, the time slot fraction for each cluster is fixed to the average number of users per cluster in the time slot, divided by the summation of the average number of users per cluster in all the time slots.
- Scheduling-S5: By this approach, the time slot fraction is fixed similar to Scheduling-S4, while considering the maximum number of users per cluster (instead of average number of users per cluster).
- Scheduling-S6: Here, time slot fraction per cluster equals the sum of users handled in the time slot over the sum of users in all clusters.

8.4 Performance analysis

8.4.1 Main assumptions and considered scenarios

To compare the performance of the scheduling and non-scheduling based handover schemes, for both cases of single cluster and multiple clusters, we assume in each cell an AP positioned at the center of the cell, emitting an optical power of 1.584 W [74], where the heights of the Rxs and the APs are set to 0.85 and 2.5 m, respectively. No concentrator is used at Rxs side, and the Rx FOV is set to 80° , where the channel gain is given by equation (2.2). Different user mobilities are considered, where for the least and the most demanding cases the maximum velocities are considered as 0.5 m/s and 5 m/s, which correspond to walking and mobility in industrial scenarios, respectively. To

Table 8.1 — Locations of APs in the considered single cluster and multiple clusters scenarios.

| Scenario | APs locations |
|---------------------|--|
| Single cluster | (2.25, 2.25, 2.5), (2.25, 4.75, 2.5), (4.75, 2.25, 2.5), (4.75, 4.75, 2.5) |
| Multiple clusters | APs locations in case of multiple clusters |
| First main cluster | (2.25, 2.25, 2.5), (2.25, 4.75, 2.5), (4.75, 2.25, 2.5), (4.75, 4.75, 2.5) |
| Second main cluster | (2.25, 7.25, 2.5), (2.25, 9.75, 2.5), (4.75, 7.25, 2.5), (4.75, 9.75, 2.5) |
| Third main cluster | (7.25, 2.25, 2.5), (7.25, 4.75, 2.5), (9.75, 2.25, 2.5), (9.75, 4.75, 2.5) |
| Fourth main cluster | (7.25, 7.25, 2.5), (7.25, 9.75, 2.5), (9.75, 7.25, 2.5), (9.75, 9.75, 2.5) |

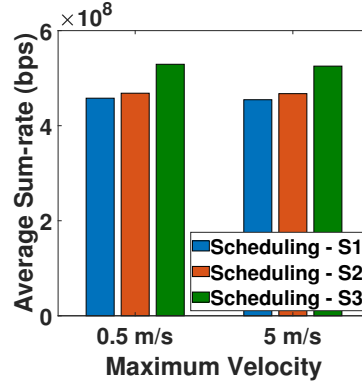
Table 8.2 — Simulation parameters.

| Parameter | Value |
|--|---|
| Room dimension (single cluster) | $(7 \text{ m} \times 7 \text{ m} \times 3 \text{ m}) \text{ m}^3$ |
| Room dimension (multiple clusters) | $(12 \text{ m} \times 12 \text{ m} \times 3 \text{ m}) \text{ m}^3$ |
| LED luminaire Lamertian order m | 1 |
| Number of LED chips per luminaire | 36 [72] |
| LED conversion efficiency S | 0.44 W/A [72] |
| PD responsivity R | 0.4 A/W [47] |
| PD area | 1 cm^2 [69] |
| System bandwidth B | 10 MHz |
| Equivalent Rx noise power spectral density | $10^{-21} \text{ A}^2/\text{Hz}$ [47] |

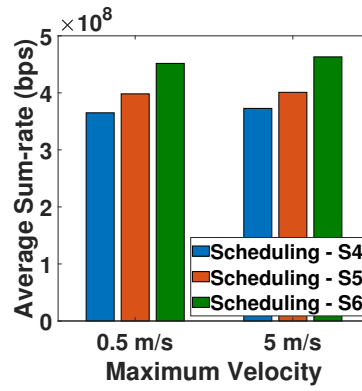
generate the Rxs positions, the RWP mobility model is used, for 45,000 user positions, where each two successive positions are separated in time by 40 ms. Also, to guarantee that the positions are within the cells coverage, user positions for single cluster and multiple clusters are limited to the intervals of (1-6) m and (1-11) m, respectively. For case of single cluster, 4 APs are considered, while for case of multiple clusters, 16 APs are considered, where each 4 APs form a main cluster, as shown in Fig. 8.3. The locations of the APs in cases of single cluster and multiple clusters are specified in Table 8.1 and the rest of the simulation parameters are provided in Table 8.2.

8.4.2 Numerical results

We start by comparing the considered time scheduling strategies specified in Subsection 8.3.1 to select the most appropriate one before comparison with the non-scheduling based approach. Figures 8.5(a) (a) and (b) show the comparison of the average achievable sum-rate between the proposed scheduling strategies for cases of single cluster and multiple clusters, respectively. From



(a) Single cluster



(b) Average Sum-rate

Figure 8.5 — Comparison of sum-rate for case of single cluster over schemes of Scheduling-S1, S2, and S3, and multiple clusters over schemes of Scheduling-S4, S5, and S6, for maximum user velocities of 0.5 m/s and 5 m/s.

Fig.8.5(a), Scheduling-S3 achieve the best performance, followed by Scheduling-S2, over both considered mobility scenarios. For case of multiple clusters, from Fig. 8.5(b) Scheduling-S6 achieves the best performance, followed by Scheduling-S5 for both mobility scenarios. This could be attributed to the more opportunistic approach by Scheduling-S3 and S6 strategies. In particular, fixing the size of the time slots based on the summation of the number of users favours CCUs in the single cluster case, because of a higher user density per time slot compared with the other CEU time slots (see coverage areas per time slot in Fig. 8.1(a)). In addition, considering the summation for case of multiple clusters allocates larger time slots to the users served in the main clusters, due to a larger number of CCUs per clusters that use the time slot (see coverage areas per time slot in Fig. 8.3). The better performance of Scheduling-S2 and S5, compared with Scheduling-S1 and S4, respectively, is due to the more opportunistic approach of the former schemes, by depending on the maximum (instead of the average) of the number of users using the time slot.

To better investigate the performance of the proposed scheduling strategies, we have shown in Fig. 8.6 a comparison between the CDFs of the users achievable throughput for the most demand-

ing case of 5 m/s maximum user speed. We notice a better performance for Scheduling-S3 and S6 schemes compared with the other schemes for both single cluster and multiple clusters cases, benefiting from their more opportunistic approach. However, we notice that Scheduling-S2 and S5 ensure the best performance in terms of minimum achievable user throughput, which results in a more robust performance for the users. Based on the results in Figs.8.5 and 8.6, Scheduling-S2 and S5 schemes are selected for further comparison with the non-scheduling based schemes, as they offer a good trade-off between network sum-rate and minimum user throughput.

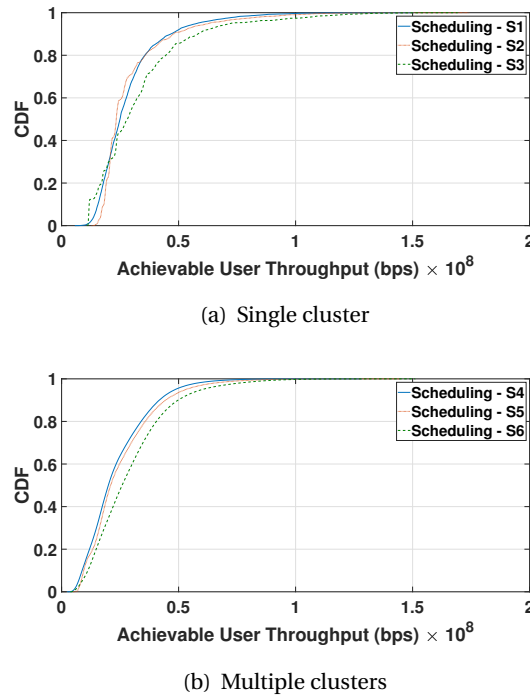
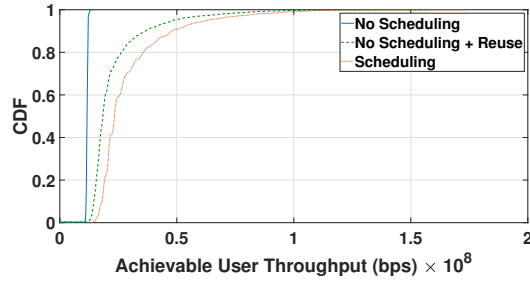


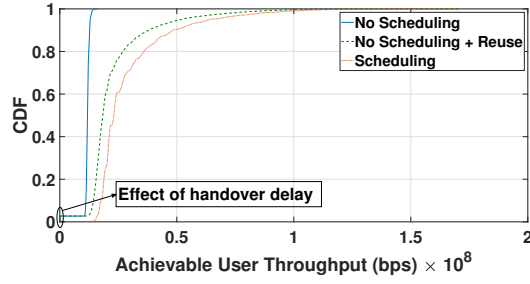
Figure 8.6 — Comparison of CDF of the user achievable throughput for the proposed scheduling strategies in cases of single cluster (Scheduling-S1, S2, and S3) and multiple clusters (Scheduling-S4, S5, and S6) over maximum user velocity of 5 m/s.

To show the advantages of the proposed scheduling-aware handover schemes we consider different non-scheduling based approaches. For the single cluster case, we adopt (i) the conventional approach of distributing the resources (i.e., time slots) equally among the users in the network, and (ii) distributing the resources while considering resource reuse (similar to frequency reuse in OFDMA [87]), where CCUs are served simultaneously by all APs, and CEUs in every cell are served non-simultaneously for ICI mitigation, such that different resources are allocated to CCU and CEUs, as considered in [173]. For this case, the average number of CCUs that use the time slot is considered for calculating the time slot size. We do not consider resource reuse for case of multiple clusters, due to the small intersection areas between the clusters compared with the cluster size. In other words, we only consider distributing the resources equally among the users in the network.

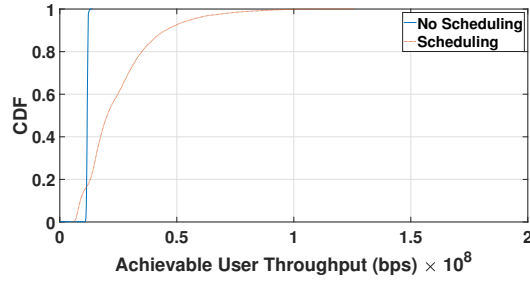
Figure 8.7 compares the CDF of the user achievable throughput using the scheduling and



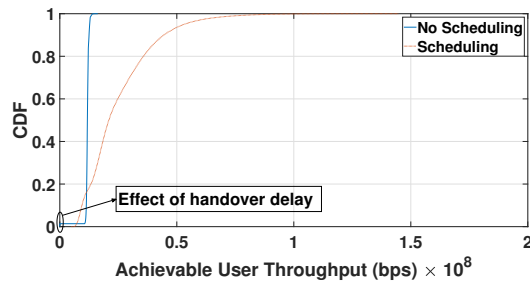
(a) Single cluster - 0.5 m/s



(b) Single cluster - 5 m/s



(c) Multiple clusters - 0.5 m/s



(d) Multiple clusters - 5 m/s

Figure 8.7 — Comparison of CDF of the user achievable throughput using the non-scheduling and the proposed scheduling schemes in cases of single cluster and multiple clusters over maximum user velocities of 0.5 m/s and 5 m/s.

non-scheduling based schemes, for both single cluster and multiple clusters scenarios. The results show that non-scheduling based solutions that do not consider resource reuse offer max-

imum fairness to the users, represented in the slope of the CDF, due to equal allocation of the resources. On the other hand, for the single cluster case, considering resource reuse offers a better user throughput performance, due to a better utilization of the network resources. The proposed handover-aware scheduling outperforms all non-scheduling based techniques, offering higher user-achievable throughputs, and a better minimum user throughput in the single cluster case.

Note, the effect of handover delay (i.e., user throughput = 0) in case of maximum velocity of 0.5 m/s is small compared with maximum velocity of 5 m/s, due to lower handover rate. In addition, the effect of handover delay is more noticeable for the single cluster case, which could be attributed to a higher handovers rate, due to a smaller coverage area per transmission (i.e., AP for single cluster compared to 4 APs for multiple clusters). Overall, these results show the robustness of the proposed schemes in terms of achievable throughput and link reliability.

8.5 Chapter summary

We proposed time scheduling based handover solutions for small/medium scale and large scale VLC networks, by benefiting from joint transmission in cell-edge areas. We compared the performances of different time slot sizing strategies, and showed that allocating the time slot sizing based on the maximum number of users who use the time slot offers good trade-off between the network sum-rate and the minimum achievable throughput. Following this, we compared the performance of the proposed schemes with conventional(non-scheduling based) schemes, in terms of achievable throughput and link reliability.

The advantages of the proposed handover solution come at the expense of a more accurate synchronization requirement. In addition, to improve the network fairness, careful consideration of the time scheduling is needed, especially for the cluster-based case.

Chapter 9

Experimental Investigation of Effect of PA in NOMA

Contents

| | |
|--|-----|
| 9.1 Introduction | 111 |
| 9.2 Experiment setup | 111 |
| 9.3 Effect of varying PA coefficient in NOMA | 114 |
| 9.4 Chapter summary | 114 |

9.1 Introduction

After presenting the theoretical studies in the previous chapters, in this chapter we present the results of the experiments that we carried out to investigate the performance of NOMA, in particular, with respect to varying the PA coefficient.

In the rest of the chapter, we start in Section 9.2 with presenting the considered system setup and parameters. Following this, we present in Section 9.3 the work on varying the PA coefficient on the performance of a single-cell 2-user NOMA system. Lastly, Section 9.4 concludes the chapter.

9.2 Experiment setup

The general schematic diagram for the considered MU VLC scenario considered is shown in Fig. 9.1, for a 1 Tx - 2 Rxs case. We use MATLAB[®] to generate the users data, modulate them, and build the NOMA signals. Following this, we forward the signals to an arbitrary waveform generator (AWG), which provides the AC part of the transmitted signals to the bias-tee (bias-T), where the LED operation point is controlled by the DC voltage provided by the DC power supply to the bias-T. The resulting optical signal emitted by the LED is then received on the Rxs. To detect the

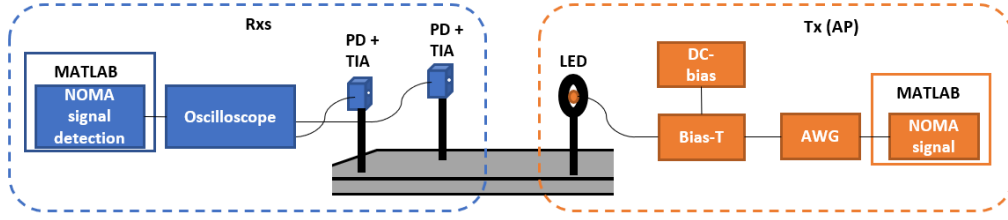


Figure 9.1 — General demonstration for the considered system setup on a 1 Tx - 2 Rx scenario, where the AC part of the transmitted signals is generated using MATLAB[®] and AWG, the DC part is provided by power supply, and a bias-T combines both of the AC and the DC parts and forwards them to the LED. At the Rx, PDs with TIA provide amplified photocurrent to oscilloscope, then signals are processed using MATLAB[®].

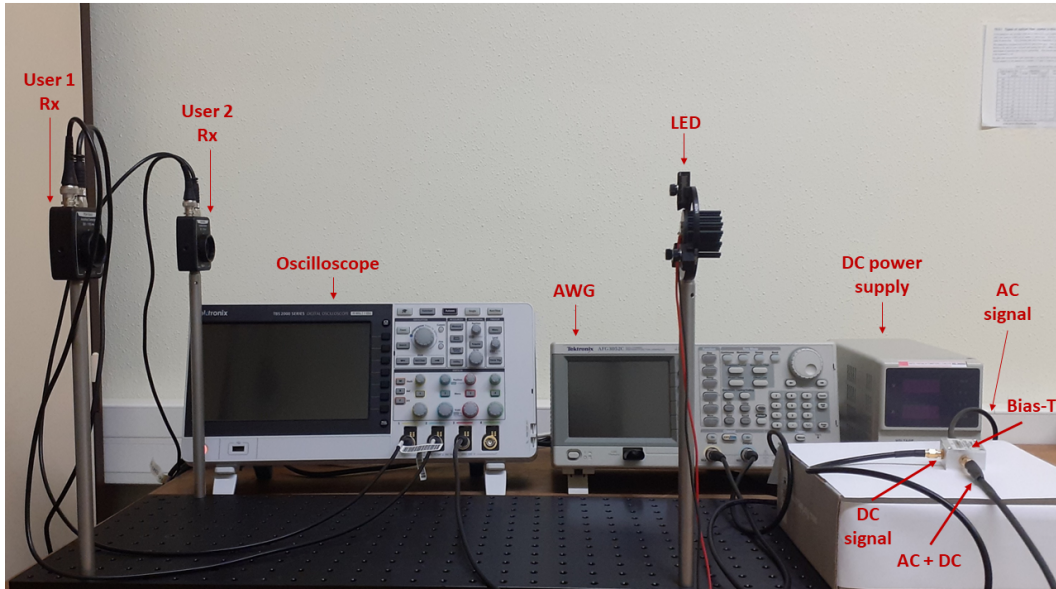


Figure 9.2 — A snapshot of the used experiment setup.

users data, we use PIN PDs with varied TIA gains. The outputs of the TIAs are then acquired by the digital oscilloscope, where the signals are processed with MATLAB[®] to recover the users data and assess the performance of the system based on the error vector magnitude (EVM) performance metric, which is given by [174]:

$$\text{EVM(dB)} = 10 \log_{10} \left(\sqrt{\frac{\sum_{s=1}^{N_s} |S_s - Z_s|^2}{\sum_{s=1}^{N_s} |Z_s|^2}} \right), \quad (9.1)$$

where S_s and Z_s refer to the reconstructed and the transmitted symbol that have index s , respectively, and N_s denotes the total number of symbols. To illustrate the considered setup, Fig. 9.2 shows a snapshot of the experiment setup consisting of the transmitter end and the receiver end, while Fig. 9.3 shows the used setup during operation.



Figure 9.3 — A snapshot of setup during operation.

Table 9.1 — The main parameters considered for the experiment setup.

| Parameter | Value |
|------------------------------|-------------------------------------|
| Tx | |
| DC bias voltage | 2.8 V |
| AC signal amplitude | 0.2 V _{pp} |
| Modulation | OOK RZ |
| Data rate (R_b) | 125 Kb/s |
| LED model | Luxeon Rebel star SR-01-WC310 [175] |
| LED bandwidth | 3 MHz |
| LED position | (0.3, 0, 0.25) m |
| Rx | |
| PD model | Thorlabs PDA100A2 [176] |
| PD type | PIN |
| PD active area | 75.4 mm ² |
| PD peak responsivity | 0.72 A/W |
| PD gain | 20 dB |
| PD bandwidth (at 20 dB gain) | 800 kHz |
| User 1 position | (0, 0, 0.25) m |
| User 2 position | (0, 0.275, 0.25) m |

Table 9.1 provides the parameters and the references of the considered components and setup.

9.3 Effect of varying PA coefficient in NOMA

As explained in Chapter 5, the choice of the PA coefficient impacts the performance of NOMA, and subsequently different PA solutions have been proposed in the literature so far. In addition, the reliance on channel information for carrying out SIC by the users with high decoding order to access their signals, makes their performance prone to degradation due to errors in channel information. To elucidate the impact of PA coefficients on the system performance, while highlighting the effect of errors in channel information, we consider a 1 Tx - 2 Rxs scenario. The PA coefficient is varied from 0.1 to 0.5, and the EVM performance is evaluated accordingly. Figure 9.4 shows a schematic for the considered setup. Assuming that User 2 has a smaller channel gain, its signal is allocated a larger power, and it detects its signal while considering User 1 signal as interference. Also, User 1 detects the User 2 signal, then uses SIC to remove its contribution in the received signal, before detecting its own signal.

Figure 9.5 depicts the EVM for User 1, and the average EVM performance of User 1 and User 2 as a function of the PA coefficient over different values for introduced error in channel information. In Fig. 9.5(a), the EVM performance of User 1 shows that increasing the PA coefficient caused performance improvement. This results from the decrease in the power allocated to User 2 signal, and the increase in the power allocated to User 1 signal (which is considered as interference signal for User 2). On the other hand, the EVM performance of User 1 shows that increasing the PA coefficient started to result in performance degradation at PA coefficient value of 0.4, despite the increase in the power allocated to User 1 signal. This could be reiterated to the decrease in the differences between the power allocated to the signals of User 1 and User 2 due to increasing the PA coefficient, which affects the detection of User 2 signal for performing SIC, and dominates the effect of increasing the power allocated to User 1. Note that, when calculating the BER performance metric for User 2 signals, we observed performance degradation starting from PA coefficient of 0.4, which affirms the observation for User 1. In addition, it is shown also in Fig. 9.5(a) that introducing error in channel information during the decoding of User 1 signals resulted in performance degradation, which increased with the increase in the magnitude of the introduced error. Fig. 9.5(b) presents the average EVM performance for User 1 and User 2. The results show that increasing the PA coefficient improves the average EVM performance, while considering PA coefficient beyond 0.3 resulted in performance degradation, which means that the EVM of User 1 signal dominates the average EVM performance compared to the EVM of User 2 signal, due to a much lower EVM for User 2 which is allocated a larger power level, and decodes the signal without carrying out SIC.

9.4 Chapter summary

We presented in this chapter experimental results for studying the performance of a basic NOMA-based transmission scenario. In particular, we investigated the effect of varying the PA coefficient on the NOMA transmission and the effect of errors in channel information. We showed the impact

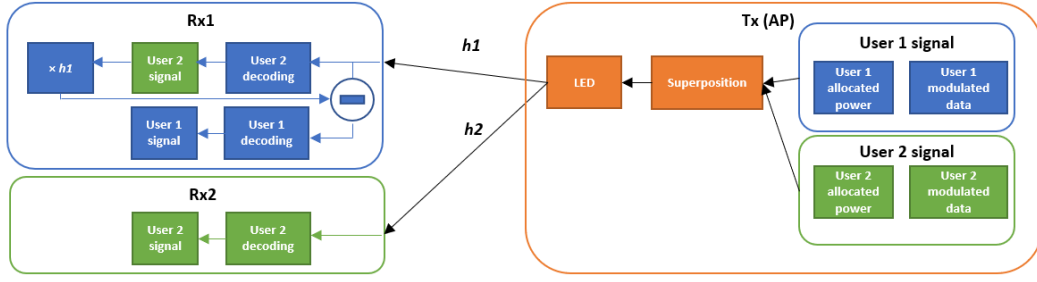
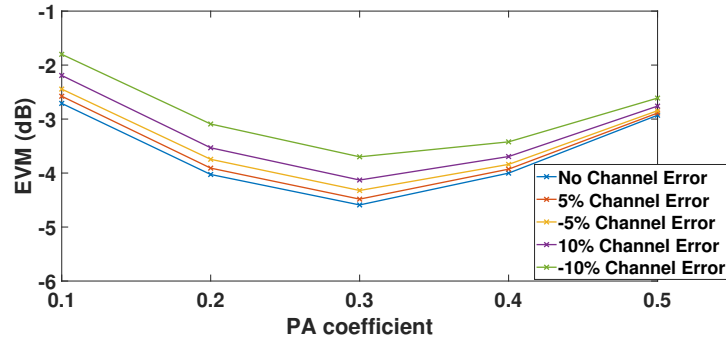
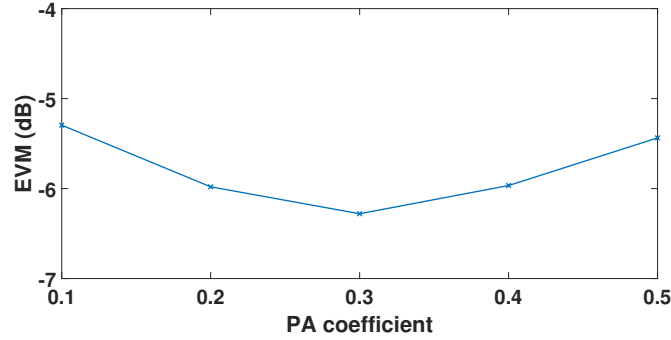


Figure 9.4 — Illustration for the considered setup of 1 Tx - 2 Rx scenario used to assess the impact of varying the PA coefficients on the system performance. It is assumed that the channel gain of User 1 (h_1) is larger than the channel gain of User 2 (h_2). Note the SIC detection accordingly for User 1.



(a) User 1



(b) Average of User 1 and User 2

Figure 9.5 — EVM performance for (a) User 1, and (b) average of User 1 and User 2, in the considered 2-user NOMA scenario.

of increasing the PA coefficient on the signals of the far (lower channel gain) and the near (higher channel gain) users in NOMA, highlighting the performance degradation of the weak user performance due to less power allocated to its signal, and the degradation of the near user performance due to the decrease in the difference between the power levels of the NOMA signals.

Chapter 10

Conclusions and Perspectives

Contents

| | |
|-----------------------------|-----|
| 10.1 Conclusions | 117 |
| 10.2 Perspectives | 119 |

10.1 Conclusions

VLC is a promising technology with potential for supporting diverse services in beyond 5G networks. Multi-cell VLC networks can address the requirement of connecting a relatively large number of devices/users with mobility flexibility in relatively large spaces. The network architecture will depend on lighting and architectural considerations for LED-based luminaire locations and the number of users. An important issue in such multi-cell networks is to manage the MU interference (MUI), in particular, due to intersecting cell coverage areas, as well as handovers due to users' mobility. To address these requirements, as explained in **Chapter 2**, we investigate the use of MU-MISO ZF pre-coding and MA techniques depending on the user density in the network.

We started in **Chapter 3** by considering the low user density case, where the number of users is limited by the number of APs. There, we considered the case study of employing UAV APs to provide lighting and communication to users in outdoor or indoor industrial scenarios. As the performance of MU-MISO ZF pre-coding is affected by the correlation in the network channel matrix, we proposed using PSO to exploit the degrees of freedom offered by controlling the UAVs (Tx) locations. The performance of the proposed optimization was studied and the resulting improvement in the network throughput was demonstrated. In addition, to reduce the computational needs at the UAVs for applying this optimization, we proposed to do the optimization at reduced rates, over different user mobility conditions, which was shown to still provide an improved performance as compared to the non-optimized UAV location case.

Following this, we considered in **Chapter 4** VLC deployment in small/medium space indoor

scenarios, while again limiting the number of users to the number of APs. Since, obviously we cannot modify the AP locations in this case (in contrast to the case study in Chapter 3), we proposed optimization of FOVs of RxS to reduce the correlation in the network channel matrix, while ensuring LOS coverage, and showed the resulting improvement in the network performance. Furthermore, to reduce the computational time needed for doing the optimization, we proposed to use the optimized FOVs as input for the new optimization. We then compared the performance of the original and the modified algorithms with the non-optimized FOVs in case of user mobility. We demonstrated the robust coverage performance of the modified algorithm at the cost of a lower quality of the solution, due to insufficient exploration of the solution space.

Although MU-MISO ZF pre-coding offers a simple and efficient solution for managing MA in low user density VLC networks, a simple solution for handling a larger number of users is to use MA techniques, which is addressed in **Chapter 5**. There, we started with comparing OFDMA and NOMA as the most suitable solutions for large space VLC scenarios in terms of handling a large number of users with high data rate demands. The results presented showed a better performance for NOMA in terms of sum-rate, which encouraged its further development in the succeeding chapters.

In **Chapter 6**, to manage MUI by NOMA, we proposed a hybrid NOMA-ZF pre-coding solution, where CEU signals are handled by ZF pre-coding, while broadcasting the ZF pre-coding signals as the least decoding order NOMA signal in each cell, dedicating small portion of the APs power to them. The advantages of this approach include suppressing IUI for CEUs through SIC detection of the corresponding CCU signals and removing ICI of the other CEU signals by ZF pre-coding. This also potentially reduces the number of handovers for moving users. However, by this method the number of efficiently handled CEUs could not exceed the number of APs. Two hybrid NOMA-ZF pre-coding schemes were proposed, based on the criteria used for calculating the ZF pre-coding coefficients, and their performances were compared with that of conventional NOMA. We showed the advantages of the proposed hybrid solutions in terms of CEUs throughput and the total network throughput.

In order to handle a larger number of CEUs than those allowed by hybrid NOMA-ZF pre-coding, while satisfying the lighting requirements, we proposed in **Chapter 7** efficient time-scheduling, scaling, and coordination of the NOMA transmissions in each cell, which we referred to as TS-NOMA. Grouping the CCUs and CEUs of each cell in different time slots allows a reduction of the number of users per NOMA transmission, which reduces the number of SIC detection steps needed. In addition, by controlling the duration and the position of the time slots, the lighting requirements and ICI mitigation can be achieved. According to the dimming requirements, six different schemes were considered for controlling the time slot size. Comparing the performance of the proposed TS-NOMA with conventional NOMA, we showed the better performance of the former over different light dimming conditions.

Although MA techniques allow handling a larger number of users compared to ZF pre-coding, in general, they are prone to link interruption due to users moving between cells. To enable

smooth handovers in case of adopting MA techniques, we proposed handover-aware scheduling solutions for both of small/medium -scale and large-scale VLC networks in **Chapter 8**, to enable soft handovers. By use of joint transmission in cell-edge areas, and adopting efficient timing and grouping of the users based on their locations, ICI mitigation was ensured. The presented results showed improved performance for the proposed handover-aware scheduling schemes compared with the non-scheduling-based handover approaches, in terms of link reliability and network sum-rate.

Lastly, we presented in **Chapter 9** experimental results for NOMA-based VLC systems, showing the impact of increasing the PA coefficient on the user performance.

10.2 Perspectives

This thesis studied interference mitigation solutions in multi-cell VLC networks, with the aim of improving the user throughput performance. Here, we present some perspective for future research on this topic.

Concerning the work in **Chapter 3**, the proposed optimization of the UAV locations in VLC networks could be extended by considering other pre-coding schemes, while adding other factors to the objective function, such as the received power at the users side, which could be beneficial for energy harvesting applications for users in remote and hard-to-reach areas. Another important parameter is the power consumption of the UAVs, which could be modelled and included in the objective functions, to address the trade-off between improving the network sum-rate and increasing the power consumption according to the user data demands.

Regarding the work on FOV optimization in **Chapter 4**, in addition to addressing different pre-coding schemes, future directions include studying the parameters of the mechanical iris used for controlling the FOVs at the RxS, and accounting for the delay needed to achieve the desired FOVs. Another direction could be updating the objective function used to optimize the FOVs with least possible number of FOV changes, to ensure less delay. Further development of the proposed memory-assisted optimization could be carried out to increase the solution quality by controlling the impact of the optimization results on the new ones.

Concerning the proposed NOMA-based schemes in **Chapters 6** and **7**, the effect of outdated CSI on the user performance should be addressed. In addition, use of more efficient PA techniques to improve the link performance in terms of sum-rate and/or fairness needs to be investigated. Also, optimization techniques (i.e., PSO) can be considered for optimizing the system parameters (e.g., FOVs) for an efficient management of the channel resources according to the user data demands over time.

Concerning the work on the proposed handover-aware scheduling in **Chapter 8**, optimization techniques could be used for deciding the time slots size, with the objective of improving certain performance metrics such as the minimum achievable user throughput and/or the fairness. For

the case of multiple-clusters, real-time optimization of the clustering can be investigated to improve the network performance by limiting the number of Rxs per cluster to the number of APs and applying ZF pre-coding in each cluster.

Regarding the experimental work presented in **Chapter 9**, the use of LED luminaires on the ceiling could be considered for assessing the performance in practical scenarios. In addition, since we studied the NOMA performance for static Rxs, one future direction can be to assess NOMA performance in case of Rx mobility. In such a case, the effect of outdated CSI, and the performance of the proposed handover-aware scheduling (for the case of a multi-cell network) can be investigated.

List of Figures

| | | |
|-----|---|------|
| 1 | Le schéma général d'un système VLC. | viii |
| 2 | L'utilisation des VLC dans divers applications indoor et outdoor. | viii |
| 3 | Un exemple de scénario VLC multicellulaire. | ix |
| 4 | le schéma de pré-codage hybride NOMA-ZF proposé. | x |
| 1.1 | Demonstration of a VLC system, highlighting transmission of the user data using light signals by an LED luminaire, and reception of the data by the user after processing the received signals. | 3 |
| 1.2 | Illustration for different indoor use cases of VLC in rooms/offices and factories (industrial scenarios) to provide high data rate communications, and in hospitals for communications in EMI-sensitive scenarios. Shown also are outdoor use cases of VLC in inter-vehicular communications, communications using streetlights, and communications using UAVs in remote and hard-to-reach areas. | 4 |
| 1.3 | An example of multi-cell VLC scenario, in which two APs provide illumination and communication to the users, highlighting different dimming needs (i.e., different illumination levels) for the users, and transition of user between cells. | 5 |
| 1.4 | Illustration of the contributions of the thesis with respect to the main challenges in VLC. | 10 |
| 2.1 | Block diagram for the main components in the VLC system, highlighting the components at the Tx and the Rx, and the VLC channel. | 12 |
| 2.2 | Demonstration for LOS propagation between AP_i and Rx_j | 15 |
| 2.3 | A generalized block diagram for DCO-OFDM. | 17 |
| 2.4 | Block diagram for the main components in the VLC system, highlighting the components at the Tx and the Rx, and the VLC channel. | 18 |
| 2.5 | An example of 3 Tx - 3 Rx VLC network, where ZF pre-coding is used for interference mitigation at each of the Rxs. | 19 |
| 2.6 | Comparison between TDMA, CDMA, OFDMA, and NOMA techniques with respect to time, frequency, and power domains, for a 3-user example. | 21 |

| | | |
|-----|--|----|
| 2.7 | Illustration for the PSO, where (a) represents the particles (represented by bees) at the first iterations while exploring the solution space and exchanging information about the personal best and global best positions and (b) represents the particles at the final iterations after converging to the optimal solution, that is represented by the largest fitness value. Note that the units of the axes depend on the variables being optimized. | 26 |
| 3.1 | Demonstration for the proposed optimization of UAV locations to improve correlation in the network channel matrix, where the changes of the UAV locations tune the channel gains in the network channel matrix for reduced correlation, which subsequently improves the performance of ZF pre-coding. | 31 |
| 3.2 | Illustration of the VLC system considered, highlighting the flow of information between a cellular network, a central control unit, UAV APs, and Rxs. | 32 |
| 3.3 | Flow chart of the proposed algorithm for location optimization of three UAVs, where ℓ and q are the indices of the number of iterations and particles, respectively. The boxes on the left and right illustrate how UAV locations are converted to integers (Int.), and how two particles move in the solution space to find the optimal solution, respectively. | 33 |
| 3.4 | Top view for the possible locations of the UAVs over the considered indoor industrial and outdoor scenarios. | 35 |
| 3.5 | Comparison between different pairs of particles (N_{\max_p}) and iterations ($N_{\max_{it}}$), over average sum-rate performance, for 4 Rxs 1000 random positions generated for indoor and outdoor scenarios. | 36 |
| 3.6 | Comparison between the optimized and the non-optimized UAV locations, where (a) presents a top view for the possible and the optimized locations of the UAVs, and the locations of the Rxs, and (b) illustrates the fitness value evolution over iterations. The blue and the red boxes provide the performance of the optimized and the non-optimized UAV locations, respectively. | 37 |
| 3.7 | Comparison between optimized and non-optimized UAV locations over average sum-rate performance for different user mobilities for (a) indoor industrial and (b) outdoor scenarios, considering different optimization update intervals. | 39 |
| 4.1 | Illustration of the proposed FOV optimization to reduce the correlation in the network channel matrix for the case of two APs and two Rxs. By tuning the FOVs, the entries of the network channel matrix are controlled. | 43 |
| 4.2 | Illustration of the considered VLC network, highlighting FOV tuning that relies on the CSI of each Rx, which is estimated and transmitted via the uplink to the central control unit. The optimized FOVs' information is transmitted via the downlink to the Rxs. | 44 |
| 4.3 | An example of FOV tuning using mechanical iris for three Rxs, where the FOV value is (a) FOV_1 for Rx_1 , (b) FOV_2 for Rx_2 , and (c) FOV_3 for Rx_3 , such that $\text{FOV}_1 > \text{FOV}_2 > \text{FOV}_3$ | 45 |

| | | |
|-----|---|----|
| 4.4 | Illustration of the considered algorithm for an example of optimizing the FOVs of 3 Rxs in a ZF pre-coding scenario, where the indices ℓ and q refer to the iteration's number and the particle's number, respectively. "Int." stands for integer. The dashed box at the left side shows how the variable values (FOVs) are extracted from integers during the optimization to solve the problem as integer programming problem, for a generalized solution in cases of having non-uniform steps between the possible FOVs. The dashed box at the right side illustrates an example of behaviour of 2 particles, under the influence of original velocity, P_{best} , and G_{best} | 46 |
| 4.5 | Comparison between optimized and non-optimized FOVs for a 4 Rx - 4 AP scenario. (a): Top view for the locations of the Rxs and the APs with heights of 0.85 m and 2.5 m, respectively. (b): Fitness value versus optimization's iterations. The dashed blue boxes represent the optimized FOVs over changes in fitness and their corresponding sum-rates. The dashed red boxes correspond to the non-optimized FOVs (50° , 70° , and 90°). | 50 |
| 5.1 | NOMA signal transmission using superposition coding and reception using SIC in a 2-user example. | 57 |
| 5.2 | Illustration of the considered scenarios, where \times and \circ show APs and users locations, respectively. Scenario 2 has four additional users with respect to Scenario 1, and Scenario 3 has four additional users with respect to Scenario 2, whose locations are indicated on Figs. 5.2(b) and 5.2(c), respectively. | 61 |
| 5.3 | Contrasting users' maximum achievable throughput using NOMA and OFDMA approaches for the scenarios presented in Fig. 5.2. | 62 |
| 5.4 | Comparison between the sum-rates of the CEUs and the total network using NOMA and OFDMA approaches for the three considered scenarios. | 63 |
| 6.1 | Illustration for the proposed hybrid NOMA-ZFP scheme for a 4-cell scenario. CEU locations correspond to the yellow colored areas, i.e., cell intersections. For instance, N_1 denotes the number of CCUs in Cell 1. | 67 |
| 6.2 | Illustration of top view of the considered scenarios: \times and \circ represent AP and user locations, respectively. | 71 |
| 6.3 | Upper bounds on the achieved rates for the users with NOMA-A, NOMA-B, NOMA-ZFP-A, and NOMA-ZFP-B schemes for the three considered scenarios in Fig. 6.2; $P_o = 1.584$ W. . . . | 74 |
| 6.4 | Network FI comparison for the considered MA schemes; $P_o = 1.584$ W. | 75 |
| 6.5 | Network sum-rate comparison for the considered MA schemes; $P_o = 1.584$ W. | 76 |
| 6.6 | Comparison between the total achieved throughput of CEUs for the considered MA schemes; $P_o = 1.584$ W. | 76 |
| 6.7 | Comparison of network sum-rate for the different MA schemes for transmitted optical powers of 5 and 10 W. | 78 |

| | | |
|-----|--|-----|
| 6.8 | Comparison of network FI of the different MA schemes for $P_o = 5$ and 10 W. | 79 |
| 6.9 | Comparison between (a) average achievable throughput for CCUs and CEUs; and (b) average network sum-rate and fairness for NOMA-ZFP-A and NOMA-ZFP-B schemes, for different percentages of power allocated to CEUs, a_{CEU}^2 | 80 |
| 7.1 | Illustration of the proposed TS-NOMA schemes. (a): top view of a 4-cell network example. (b) and (c): signal transmission timing for different users according to Scheme A and B, respectively. | 86 |
| 7.2 | Comparison of sum-rate and FI for TS-NOMA and NOMA for the case of no dimming ($\delta = 1$). | 91 |
| 7.3 | Comparison of sum-rate and FI between TS-NOMA and NOMA for (a) $\delta = 70\%$, (b) 50%, (c) 30%, and (d) 25%. | 92 |
| 8.1 | (a) Top view for AP coverage areas distributions for the proposed handover-aware scheduling and the corresponding resource utilization, (b) illustration for the handover decision for non-scheduling based handover, and (c) flowcharts of procedures of non-scheduling and scheduling -based handover approaches. | 98 |
| 8.2 | A step by step comparison between non-scheduling and scheduling based handover approaches over different scenarios. | 100 |
| 8.3 | Illustration for the cluster formation, and the corresponding resource utilization for the proposed handover-aware scheduling in case of multiple clusters. | 102 |
| 8.4 | A step by step comparison between scheduling and non-scheduling based handover over different scenarios in case of multiple clusters. | 104 |
| 8.5 | Comparison of sum-rate for case of single cluster over schemes of Scheduling-S1, S2, and S3, and multiple clusters over schemes of Scheduling-S4, S5, and S6, for maximum user velocities of 0.5 m/s and 5 m/s. | 107 |
| 8.6 | Comparison of CDF of the user achievable throughput for the proposed scheduling strategies in cases of single cluster (Scheduling-S1, S2, and S3) and multiple clusters (Scheduling-S4, S5, and S6) over maximum user velocity of 5 m/s. | 108 |
| 8.7 | Comparison of CDF of the user achievable throughput using the non-scheduling and the proposed scheduling schemes in cases of single cluster and multiple clusters over maximum user velocities of 0.5 m/s and 5 m/s. | 109 |
| 9.1 | General demonstration for the considered system setup on a 1 Tx - 2 Rxs scenario, where the AC part of the transmitted signals is generated using MATLAB [®] and AWG, the DC part is provided by power supply, and a bias-T combines both of the AC and the DC parts and forwards them to the LED. At the Rxs, PDs with TIA provide amplified photo-current to oscilloscope, then signals are processed using MATLAB [®] | 112 |
| 9.2 | A snapshot of the used experiment setup. | 112 |

| | | |
|-----|--|-----|
| 9.3 | A snapshot of setup during operation. | 113 |
| 9.4 | Illustration for the considered setup of 1 Tx - 2 Rxs scenario used to assess the impact of varying the PA coefficients on the system performance. It is assumed that the channel gain of User 1 (h_1) is larger than the channel gain of User 2 (h_2). Note the SIC detection accordingly for User 1. | 115 |
| 9.5 | EVM performance for (a) User 1, and (b) average of User 1 and User 2, in the considered 2-user NOMA scenario. | 115 |

List of Tables

| | | |
|-----|--|-----|
| 2.1 | Comparison between different MA techniques. | 24 |
| 3.1 | Simulation parameters. | 34 |
| 3.2 | Parameters of the indoor industrial and the outdoor scenarios. | 35 |
| 4.1 | Simulation parameters. | 48 |
| 4.2 | Comparison between different combinations of number of particles (N_{\max_p}) and iterations ($N_{\max_{it}}$) over average sum-rate and LOS blockage performance, for cases of random Rx heights in 4 Rx scenarios. | 48 |
| 4.3 | Number of scenarios with at least 1 Rx with no LOS coverage and average sum-rate performance for optimized (Opt.) and non-optimized fixed FOVs, for fixed and random Z_{Rx} between 0.85 and 1.35 m, and random Rxs' orientations. | 51 |
| 4.4 | LOS blockage and average sum-rate performance for different cases of optimized and non-optimized FOVs for 1000 generated positions of 4 Rxs reflecting user mobility according to random way-point model. | 52 |
| 5.1 | Simulation parameters. | 59 |
| 6.1 | Simulation parameters. | 70 |
| 6.2 | Locations of APs, CCUs, and CEUs (in meter) in the considered scenarios. | 72 |
| 6.3 | Decoding order of users' signals for NOMA-A (ascending) | 72 |
| 6.4 | Sum-rate and FI performance averaged over 100 random scenarios | 77 |
| 7.1 | Simulation parameters. | 90 |
| 8.1 | Locations of APs in the considered single cluster and multiple clusters scenarios. | 106 |
| 8.2 | Simulation parameters. | 106 |
| 9.1 | The main parameters considered for the experiment setup. | 113 |

Bibliography

- [1] Z. Ghassemlooy, L. N. Alves, S. Zvanovec, and M. A. Khalighi, Eds., *Visible Light Communications: Theory and Applications*, CRC-Press, 2017.
- [2] A. Feldmann et al., “The lockdown effect: Implications of the COVID-19 pandemic on internet traffic,” in *Proceedings of the ACM Internet Measurement Conference*. Oct. 2020, IMC ’20, Association for Computing Machinery, Pittsburgh, PA, USA.
- [3] M. Uysal, C. Capsoni, Z. Ghassemlooy, A. Boucouvalas, and Eds. E. Udvary, *Optical Wireless Communications: an Emerging Technology*, Springer, 2016.
- [4] L. Bariah, L. Mohjazi, S. Muhaidat, P. C. Sofotasios, G. K. Kurt, H. Yanikomeroglu, and O. A. Dobre, “A prospective look: Key enabling technologies, applications and open research topics in 6G networks,” *IEEE Access*, vol. 8, pp. 174792–174820, 2020.
- [5] A. A. Huurdeman, *The Worldwide History of Telecommunications*, John Wiley & Sons, Ltd, 2003.
- [6] A. G. Bell, “Selenium and the photophone,” *Nature*, vol. 22, no. 569, pp. 500–503, Sep. 1880.
- [7] R. Zhang, J. Wang, Z. Wang, Z. Xu, C. Zhao, and L. Hanzo, “Visible light communications in heterogeneous networks: Paving the way for user-centric design,” *IEEE Wireless Communications*, vol. 22, no. 2, pp. 8–16, 2015.
- [8] F. R. Gfeller and U. Bapst, “Wireless in-house data communication via diffuse infrared radiation,” *Proceedings of the IEEE*, vol. 67, no. 11, pp. 1474–1486, 1979.
- [9] J. M. Kahn and J. R. Barry, “Wireless infrared communications,” *Proceedings of the IEEE*, vol. 85, no. 2, pp. 265–298, Feb. 1997.
- [10] T. Komine and M. Nakagawa, “Fundamental analysis for visible-light communication system using LED lights,” *IEEE Transactions on Consumer Electronics*, vol. 50, no. 1, pp. 100–107, Feb 2004.
- [11] H. Haas, L. Yin, Y. Wang, and C. Chen, “What is LiFi?,” *Journal of Lightwave Technology*, vol. 34, no. 6, pp. 1533–1544, 2016.

- [12] Z. Xu and B. M. Sadler, "Ultraviolet communications: Potential and state-of-the-art," *IEEE Communications Magazine*, vol. 46, no. 5, pp. 67–73, 2008.
- [13] Zabih Ghassemlooy, Stanislav Zvanovec, Mohammad-Ali Khalighi, Wasiu O. Popoola, and Joaquin Perez, "Optical wireless communication systems," *Optik*, vol. 151, pp. 1–6, 2017, Optical Wireless Communication Systems.
- [14] Mohammad Ali Khalighi, Zabih Ghassemlooy, Mohamed-Slim Alouini, Steve Hranilovic, and Stanislav Zvanovec, "Special issue on: Optical wireless communications for emerging connectivity requirements," *IEEE Open Journal of the Communications Society*, vol. 2, pp. 82–86, 2021.
- [15] F. Miramirkhani, O. Narmanlioglu, M. Uysal, and E. Panayirci, "A mobile channel model for VLC and application to adaptive system design," *IEEE Communications Letters*, vol. 21, no. 5, pp. 1035–1038, 2017.
- [16] Y. Tanaka, T. Komine, S. Haruyama, and M. Nakagawa, "Indoor visible communication utilizing plural white LEDs as lighting," in *12th IEEE International Symposium on Personal, Indoor and Mobile Radio Communications (PIMRC)*, Sep. 2001, San Diego, USA.
- [17] "VisIoN Training Network website," <https://www.vision-itn.eu/>.
- [18] "ENLIGHT'EM Training Network website," <https://www.enlightem.eu/>.
- [19] "COST Action CA19111 - NEWFOCUS website," <https://www.newfocus-cost.eu/>.
- [20] Y. Wang, X. Wu, and H. Haas, "Load balancing game with shadowing effect for indoor hybrid LiFi/RF networks," *IEEE Transactions on Wireless Communications*, vol. 16, no. 4, pp. 2366–2378, 2017.
- [21] S. Shao, A. Khreishah, M. B. Rahaim, H. Elgala, M. Ayyash, T. D. C. Little, and J. Wu, "An indoor hybrid WiFi-VLC internet access system," in *2014 IEEE 11th International Conference on Mobile Ad Hoc and Sensor Systems*, Oct. 2014, pp. 569–574, Philadelphia, PA, USA.
- [22] S. Shao, A. Khreishah, M. Ayyash, M. B. Rahaim, H. Elgala, V. Jungnickel, D. Schulz, T. D. C. Little, J. Hilt, and R. Freund, "Design and analysis of a visible-light-communication enhanced WiFi system," *IEEE/OSA Journal of Optical Communications and Networking*, vol. 7, no. 10, pp. 960–973, 2015.
- [23] P. W. Berenguer, P. Hellwig, D. Schulz, J. Hilt, G. Kleinpeter, J. K. Fischer, and V. Jungnickel, "Real-time optical wireless mobile communication with high physical layer reliability," *Journal of Lightwave Technology*, vol. 37, no. 6, pp. 1638–1646, 2019.
- [24] V. Jungnickel, P. W. Berenguer, S. M. Mana, M. Hinrichs, S. M. Kouhini, K. L. Bober, and C. Kottke, "LiFi for industrial wireless applications," in *2020 Optical Fiber Communications Conference and Exhibition (OFC)*, Mar. 2020, pp. 1–3, San Diego, CA, USA.

- [25] C. Lebas, S. Sahuguede, A. Julien-Vergonjanne, P. Combeau, and L. Aveneau, "Infrared and visible links for medical body sensor networks," in *2018 Global LIFI Congress (GLC)*, Feb. 2018, pp. 1–6, Paris, France.
- [26] M. Yoshino, S. Haruyama, and M. Nakagawa, "High-accuracy positioning system using visible LED lights and image sensor," in *2008 IEEE Radio and Wireless Symposium*, Jan. 2008, pp. 439–442, Orlando, FL, USA.
- [27] K. Qiu, F. Zhang, and M. Liu, "Let the light guide us: VLC-based localization," *IEEE Robotics Automation Magazine*, vol. 23, no. 4, pp. 174–183, Jan. 2016, Orlando, FL, USA.
- [28] N. Lourenço, D. Terra, N. Kumar, L. N. Alves, and R. L. Aguiar, "Visible light communication system for outdoor applications," in *2012 8th International Symposium on Communication Systems, Networks Digital Signal Processing (CSNDSP)*, July 2012, pp. 1–6, Poznan, Poland.
- [29] M. Uysal, Z. Ghassemlooy, A. Bekkali, A. Kadri, and H. Menouar, "Visible light communication for vehicular networking: Performance study of a V2V system using a measured headlamp beam pattern model," *IEEE Vehicular Technology Magazine*, vol. 10, no. 4, pp. 45–53, 2015.
- [30] A. Căilean and M. Dimian, "Current challenges for visible light communications usage in vehicle applications: A survey," *IEEE Communications Surveys Tutorials*, vol. 19, no. 4, pp. 2681–2703, 2017.
- [31] H. Deng, J. Li, A. Sayegh, S. Birolini, and S. Andreani, "Twinkle: A flying lighting companion for urban safety," in *Proceedings of the Twelfth ACM International Conference on Tangible, Embedded, and Embodied Interaction*, Mar. 2018, Stockholm, Sweden.
- [32] Y. Yang, M. Chen, C. Guo, C. Feng, and W. Saad, "Power efficient visible light communication with unmanned aerial vehicles," *IEEE Communications Letters*, vol. 23, no. 7, pp. 1272–1275, 2019.
- [33] N. Cen, "FLight: Toward programmable visible-light-band wireless UAV networking," Sep. 2020, LIOT '20, pp. 24–29, Association for Computing Machinery, London, United Kingdom.
- [34] E. F. Schubert, *Light-Emitting Diodes*, Cambridge University Press, 2 edition, 2006.
- [35] G. Cossu, A. M. Khalid, P. Choudhury, R. Corsini, and E. Ciaramella, "3.4 Gbit/s visible optical wireless transmission based on RGB LED," *Opt. Express*, vol. 20, no. 26, pp. B501–B506, Dec 2012.
- [36] Y. Wang, Y. Wang, N. Chi, J. Yu, and H. Shang, "Demonstration of 575-Mb/s downlink and 225-Mb/s uplink bi-directional SCM-WDM visible light communication using RGB LED and phosphor-based LED," *Opt. Express*, vol. 21, no. 1, pp. 1203–1208, Jan 2013.

- [37] A. Pepe, Z. Wei, and H. Y. Fu, "Heuristic, machine learning approach to 8-CSK decision regions in RGB-LED visible light communication," *OSA Continuum*, vol. 3, no. 3, pp. 473–482, Mar 2020.
- [38] J. Grubor, S. Randel, K. Langer, and J. W. Walewski, "Broadband information broadcasting using LED-based interior lighting," *Journal of Lightwave Technology*, vol. 26, no. 24, pp. 3883–3892, 2008.
- [39] H. Le Minh, D. O'Brien, G. Faulkner, L. Zeng, K. Lee, D. Jung, Y. Oh, and E. T. Won, "100-Mb/s NRZ visible light communications using a postequalized white LED," *IEEE Photonics Technology Letters*, vol. 21, no. 15, pp. 1063–1065, 2009.
- [40] X. Zhang, Z. Babar, P. Petropoulos, H. Haas, and L. Hanzo, "The evolution of optical OFDM," *IEEE Communications Surveys Tutorials*, pp. 1–1, 2021.
- [41] D. Tsonev, H. Chun, S. Rajbhandari, J. J. D. McKendry, S. Videv, E. Gu, M. Haji, S. Watson, A. E. Kelly, G. Faulkner, M. D. Dawson, H. Haas, and D. O'Brien, "A 3-Gb/s single-LED OFDM-based wireless VLC link using a gallium nitride μ LED," *IEEE Photonics Technology Letters*, vol. 26, no. 7, pp. 637–640, 2014.
- [42] P. A. Haigh, Z. Ghassemlooy, S. Rajbhandari, and I. Papakonstantinou, "Visible light communications using organic light emitting diodes," *IEEE Communications Magazine*, vol. 51, no. 8, pp. 148–154, 2013.
- [43] M. A. Khalighi and M. Uysal, "Survey on free space optical communication: A communication theory perspective," *IEEE Communications Surveys Tutorials*, vol. 16, no. 4, pp. 2231–2258, 2014.
- [44] E. Sarbazi, M. Safari, and H. Haas, "Statistical modeling of single-photon avalanche diode receivers for optical wireless communications," *IEEE Transactions on Communications*, vol. 66, no. 9, pp. 4043–4058, 2018.
- [45] M. A. Khalighi, H. Akhouayri, and S. Hranilovic, "Silicon-photomultiplier-based underwater wireless optical communication using pulse-amplitude modulation," *IEEE Journal of Oceanic Engineering*, vol. 45, no. 4, pp. 1611–1621, 2020.
- [46] J. Grubor, S. Randel, K. . Langer, and J. W. Walewski, "Bandwidth-efficient indoor optical wireless communications with white light-emitting diodes," in *2008 6th International Symposium on Communication Systems, Networks and Digital Signal Processing*, July 2008, pp. 165–169, Graz, Austria.
- [47] L. Yin, W. O. Popoola, X. Wu, and H. Haas, "Performance evaluation of non-orthogonal multiple access in visible light communication," *IEEE Transactions on Communications*, vol. 64, no. 12, pp. 5162–5175, Dec. 2016.

- [48] H. Marshoud, P. C. Sofotasios, S. Muhaidat, G. K. Karagiannidis, and B. S. Sharif, "On the performance of visible light communication systems with non-orthogonal multiple access," *IEEE Transactions on Wireless Communications*, vol. 16, no. 10, pp. 6350–6364, Oct 2017.
- [49] L. Zeng, D. C. O'Brien, H. L. Minh, G. E. Faulkner, K. Lee, D. Jung, Y. Oh, and E. T. Won, "High data rate multiple input multiple output (MIMO) optical wireless communications using white LED lighting," *IEEE Journal on Selected Areas in Communications*, vol. 27, no. 9, pp. 1654–1662, Dec. 2009.
- [50] K. Ying, H. Qian, R. J. Baxley, and S. Yao, "Joint optimization of precoder and equalizer in MIMO VLC systems," *IEEE Journal on Selected Areas in Communications*, vol. 33, no. 9, pp. 1949–1958, 2015.
- [51] K. Lee, H. Park, and J. R. Barry, "Indoor channel characteristics for visible light communications," *IEEE Communications Letters*, vol. 15, no. 2, pp. 217–219, February 2011.
- [52] S. Long, M. A. Khalighi, M. Wolf, S. Bourenanne, and Z. Ghassemlooy, "Investigating channel frequency selectivity in indoor visible light communication systems," *IET Optoelectronics*, vol. 10, no. 3, pp. 80–88, May 2016.
- [53] Dehao Wu, Zabih Ghassemlooy, Wen-De Zhong, Mohammad-Ali Khalighi, Hoa Le Minh, Chen Chen, Stanislav Zvanovec, and Anthony C. Boucouvalas, "Effect of optimal Lambertian order for cellular indoor optical wireless communication and positioning systems," *Optical Engineering*, vol. 55, no. 6, pp. 1 – 8, 2016.
- [54] Shihe Long, *Indoor channel modeling and high data-rate transmission for visible light communication systems*, Ph.D. thesis, Ecole Centrale Marseille, 2016.
- [55] P. A. Haigh, A. Burton, K. Werfli, H. Le Minh, E. Bentley, P. Chvojka, W. O. Popoola, I. Papakonstantinou, and S. Zvanovec, "A multi-CAP visible-light communications system with 4.85-b/s/Hz spectral efficiency," *IEEE Journal on Selected Areas in Communications*, vol. 33, no. 9, pp. 1771–1779, 2015.
- [56] Mike Wolf, Sher Ali Cheema, Mohammad Ali Khalighi, and Shihe Long, "Transmission schemes for visible light communications in multipath environments," in *2015 17th International Conference on Transparent Optical Networks (ICTON)*, Sep. 2015, pp. 1–7, Istanbul, Turkey.
- [57] Shihe Long, Mohammad-Ali Khalighi, Mike Wolf, Zabih Ghassemlooy, and Salah Bourenanne, "Performance of carrier-less amplitude and phase modulation with frequency domain equalization for indoor visible light communications," in *2015 4th International Workshop on Optical Wireless Communications (IWOW)*, Sep. 2015, pp. 16–20, Istanbul, Turkey.
- [58] K. Werfli, P. Chvojka, Z. Ghassemlooy, N. B. Hassan, S. Zvanovec, A. Burton, P. A. Haigh, and M. R. Bhatnagar, "Experimental demonstration of high-speed 4×4 imaging multi-CAP

- MIMO visible light communications,” *Journal of Lightwave Technology*, vol. 36, no. 10, pp. 1944–1951, 2018.
- [59] Shihe Long and Mohammad Ali Khalighi, “Advantage of CAP signaling for VLC systems under non-linear LED characteristics,” in *2019 2nd West Asian Colloquium on Optical Wireless Communications (WACOWC)*, 2019, pp. 21–25.
- [60] J. Armstrong and B. J.C. Schmidt, “Comparison of asymmetrically clipped optical OFDM and DC-biased optical OFDM in AWGN,” *IEEE Communications Letters*, vol. 12, no. 5, pp. 343–345, 2008.
- [61] J. Armstrong, “OFDM for optical communications,” *Journal of Lightwave Technology*, vol. 27, no. 3, pp. 189–204, Feb. 2009.
- [62] S. Dimitrov and H. Haas, “Information rate of OFDM-based optical wireless communication systems with nonlinear distortion,” *Journal of Lightwave Technology*, vol. 31, no. 6, pp. 918–929, Mar. 2013.
- [63] J. B. Carruthers and J. M. Kahn, “Multiple-subcarrier modulation for nondirected wireless infrared communication,” *IEEE Journal on Selected Areas in Communications*, vol. 14, no. 3, pp. 538–546, Apr. 1996.
- [64] J. Armstrong and A. J. Lowery, “Power efficient optical OFDM,” *Electronics Letters*, vol. 42, no. 6, pp. 370–372, Mar. 2006.
- [65] X. Deng, S. Mardankorani, G. Zhou, and J. M. G. Linnartz, “DC-bias for optical OFDM in visible light communications,” *IEEE Access*, vol. 7, pp. 98319–98330, 2019.
- [66] Z. Tian, K. Wright, and X. Zhou, “Lighting up the internet of things with DarkVLC,” Feb. 2016, HotMobile 16, pp. 33–38, ACM, St. Augustine, Florida, USA.
- [67] S. Naribole, S. Chen, E. Heng, and E. Knightly, “LiRa: A WLAN architecture for visible light communication with a Wi-Fi uplink,” in *2017 14th Annual IEEE International Conference on Sensing, Communication, and Networking (SECON)*, June 2017, pp. 1–9, San Diego, CA, USA.
- [68] M. Dehghani Soltani, X. Wu, M. Safari, and H. Haas, “Bidirectional user throughput maximization based on feedback reduction in LiFi networks,” *IEEE Transactions on Communications*, vol. 66, no. 7, pp. 3172–3186, July 2018.
- [69] Z. Yu, R. J. Baxley, and G. T. Zhou, “Multi-user MISO broadcasting for indoor visible light communication,” in *International Conference on Acoustics, Speech and Signal Processing (ICASSP)*, May 2013, pp. 4849–4853, Vancouver, Canada.
- [70] Y. Hong, J. Chen, Z. Wang, and C. Yu, “Performance of a precoding MIMO system for decentralized multiuser indoor visible light communications,” *IEEE Photonics Journal*, vol. 5, no. 4, pp. 7800211–7800211, Aug. 2013.

- [71] T. V. Pham, H. Le-Minh, and A. T. Pham, "Multi-user visible light communication broadcast channels with zero-forcing precoding," *IEEE Transactions on Communications*, vol. 65, no. 6, pp. 2509–2521, June 2017.
- [72] H. Ma, L. Lampe, and S. Hranilovic, "Coordinated broadcasting for multiuser indoor visible light communication systems," *IEEE Transactions on Communications*, vol. 63, no. 9, pp. 3313–3324, Sept. 2015.
- [73] B. Li, J. Wang, R. Zhang, H. Shen, C. Zhao, and L. Hanzo, "Multiuser MISO transceiver design for indoor downlink visible light communication under per-LED optical power constraints," *IEEE Photonics Journal*, vol. 7, no. 4, pp. 1–15, Aug. 2015.
- [74] M. W. Eltokhey, M. A. Khalighi, A. S. Ghazy, and S. Hranilovic, "Hybrid NOMA and ZF precoding transmission for multi-cell VLC networks," *IEEE Open Journal of the Communications Society*, vol. 1, pp. 513–526, 2020.
- [75] L. Yin, X. Wu, and H. Haas, "SDMA grouping in coordinated multi-point VLC systems," in *2015 IEEE Summer Topicals Meeting Series (SUM)*, July 2015, pp. 169–170, Nassau, Bahamas.
- [76] T. V. Pham, H. L. Minh, and A. T. Pham, "Multi-cell VLC: Multi-user downlink capacity with coordinated precoding," in *2017 IEEE International Conference on Communications Workshops (ICC Workshops)*, May 2017, pp. 469–474, Paris, France.
- [77] Z. Feng, C. Guo, Z. Ghassemlooy, and Y. Yang, "The spatial dimming scheme for the MU-MIMO-OFDM VLC system," *IEEE Photonics Journal*, vol. 10, no. 5, pp. 1–13, Oct. 2018.
- [78] H. Elgala, R. Mesleh, and H. Haas, "Indoor optical wireless communication: potential and state-of-the-art," *IEEE Communications Magazine*, vol. 49, no. 9, pp. 56–62, Sept. 2011.
- [79] Z. Chen, D. A. Basnayaka, and H. Haas, "Space division multiple access for optical attocell network using angle diversity transmitters," *Journal of Lightwave Technology*, vol. 35, no. 11, pp. 2118–2131, June 2017.
- [80] J. A. Salehi, "Code division multiple-access techniques in optical fiber networks - part i: Fundamental principles," *IEEE Transactions on Communications*, vol. 37, no. 8, pp. 824–833, Aug. 1989.
- [81] S. S. Bawazir, P. C. Sofotasios, S. Muhaidat, Y. Al-Hammadi, and G. K. Karagiannidis, "Multiple access for visible light communications: Research challenges and future trends," *IEEE Access*, vol. 6, pp. 26167–26174, 2018.
- [82] M. F. Guerra-Medina, O. Gonzalez, B. Rojas-Guillama, J. A. Martin-Gonzalez, F. Delgado, and J. Rabadan, "Ethernet-OCDMA system for multi-user visible light communications," *Electronics Letters*, vol. 48, no. 4, pp. 227–228, Feb. 2012.

- [83] P. H. Pathak, X. Feng, P. Hu, and P. Mohapatra, "Visible light communication, networking, and sensing: A survey, potential and challenges," *IEEE Communications Surveys Tutorials*, vol. 17, no. 4, pp. 2047–2077, Fourth Quarter 2015.
- [84] S. Hranilovic, "Minimum-bandwidth optical intensity Nyquist pulses," *IEEE Transactions on Communications*, vol. 55, no. 3, pp. 574–583, Mar. 2007.
- [85] W. Gappmair, "On parameter estimation for bandlimited optical intensity channels," *MDPI Computation, Special Issue on Optical Wireless Communication Systems*, vol. 7, no. 1, pp. 1–13, Feb. 2019.
- [86] M. A. Khalighi, S. Long, S. Bourennane, and Z. Ghassemlooy, "PAM and CAP-based transmission schemes for visible-light communications," *IEEE Access, Special issue on Optical Wireless Technologies for 5G Communications and Beyond*, vol. 5, pp. 27002–27013, Oct. 2017.
- [87] C. Chen, S. Videv, D. Tsonev, and H. Haas, "Fractional frequency reuse in DCO-OFDM-based optical attocell networks," *Journal of Lightwave Technology*, vol. 33, no. 19, pp. 3986–4000, Oct. 2015.
- [88] O. Maraqa, A. S. Rajasekaran, S. Al-Ahmadi, H. Yanikomeroglu, and S. M. Sait, "A survey of rate-optimal power domain NOMA with enabling technologies of future wireless networks," *IEEE Communications Surveys Tutorials*, vol. 22, no. 4, pp. 2192–2235, 2020.
- [89] Z. Yang, W. Xu, and Y. Li, "Fair non-orthogonal multiple access for visible light communication downlinks," *IEEE Wireless Communications Letters*, vol. 6, no. 1, pp. 66–69, Feb. 2017.
- [90] Y. Fu, Y. Hong, L. Chen, and C. W. Sung, "Enhanced power allocation for sum rate maximization in OFDM-NOMA VLC systems," *IEEE Photonics Technology Letters*, vol. 30, no. 13, pp. 1218–1221, Jul. 2018.
- [91] Q. Li, T. Shang, T. Tang, and Z. Dong, "Optimal power allocation scheme based on multi-factor control in indoor NOMA-VLC systems," *IEEE Access*, vol. 7, pp. 82878–82887, 2019.
- [92] Z. Tahira, H. M. Asif, A. A. Khan, S. Baig, S. Mumtaz, and S. Al-Rubaye, "Optimization of non-orthogonal multiple access based visible light communication systems," *IEEE Communications Letters*, vol. 23, no. 8, pp. 1365–1368, 2019.
- [93] S. Feng, T. Bai, and L. Hanzo, "Joint power allocation for the multi-user NOMA-downlink in a power-line-fed VLC network," *IEEE Transactions on Vehicular Technology*, vol. 68, no. 5, pp. 5185–5190, 2019.
- [94] Y. S. Eroglu, C. K. Anjinappa, A. Guvenc, and N. Pala, "Slow beam steering and noma for indoor multi-user visible light communications," *IEEE Transactions on Mobile Computing*, vol. 20, no. 4, pp. 1627–1641, 2021.

- [95] S. Feng, R. Zhang, W. Xu, and L. Hanzo, "Multiple access design for ultra-dense VLC networks: Orthogonal vs non-orthogonal," *IEEE Transactions on Communications*, vol. 67, no. 3, pp. 2218–2232, Mar. 2018.
- [96] X. Zhang, Q. Gao, C. Gong, and Z. Xu, "User grouping and power allocation for NOMA visible light communication multi-cell networks," *IEEE Communications Letters*, vol. 21, no. 4, pp. 777–780, Apr. 2017.
- [97] M. W. Eltokhey, M. A. Khalighi, and Z. Ghassemlooy, "Power allocation optimization in NOMA-based multi-cell VLC networks," in *2021 5th International Workshop on Optical Wireless Communications (IWOW)*, September 2021, Berlin, Germany.
- [98] N. A. Amran, M. Dehghani Soltani, M. Yaghoobi, and M. Safari, "Deep learning based signal detection for OFDM VLC systems," in *2020 IEEE International Conference on Communications Workshops*, June 2020, pp. 1–6, Dublin, Ireland.
- [99] M. A. Arfaoui, M. D. Soltani, I. Tavakkolnia, A. Ghayeb, C. Assi, M. Safari, and H. Haas, "Invoking deep learning for joint estimation of indoor LiFi user position and orientation," *IEEE Journal on Selected Areas in Communications*, pp. 1–1, 2021.
- [100] M. H. Khadr, I. Walter, H. Elgala, and S. Muhaidat, "Machine learning-based massive augmented spatial modulation (ASM) for IoT VLC systems," *IEEE Communications Letters*, vol. 25, no. 2, pp. 494–498, 2021.
- [101] B. Lin, Q. Lai, Z. Ghassemlooy, and X. Tang, "A machine learning based signal demodulator in NOMA-VLC," *Journal of Lightwave Technology*, pp. 1–1, 2021.
- [102] I. Boussaid, J. Lepagnot, and P. Siarry, "A survey on optimization metaheuristics," *Information Sciences*, vol. 237, pp. 82 – 117, 2013.
- [103] L. Calvet, J. de Armas, D. Masip, and A. A. Juan, "Learnheuristics: hybridizing metaheuristics with machine learning for optimization with dynamic inputs," *Open Mathematics*, vol. 15, no. 1, pp. 261–280, 2017.
- [104] Mahmoud W. Eltokhey, K.R. Mahmoud, Zabih Ghassemlooy, and Salah S.A. Obayya, "Optimization of locations of diffusion spots in indoor optical wireless local area networks," *Optics Communications*, vol. 410, pp. 577–584, 2018.
- [105] M. W. Eltokhey, K. R. Mahmoud, and S. S. A. Obayya, "Optimised diffusion spots' locations for simultaneous improvement in SNR and delay spread," *Photonic Network Communications*, vol. 31, no. 1, pp. 172–182, 2016.
- [106] M. S. Demir, S. M. Sait, and M. Uysal, "Unified resource allocation and mobility management technique using particle swarm optimization for VLC networks," *IEEE Photonics Journal*, vol. 10, no. 6, pp. 1–9, 2018.

- [107] M. W. Eltokhey, K. R. Mahmoud, Z. Ghassemlooy, and S. S.A. Obayya, "Optimization of intensities and locations of diffuse spots in indoor optical wireless communications," *Optical Switching and Networking*, vol. 33, pp. 177 – 183, 2019.
- [108] M. W. Eltokhey, M. A. Khalighi, and Z. Ghassemlooy, "Optimization of receivers field-of-views in multi-user VLC networks: A bio-inspired approach," *IEEE Wireless Communications*, to appear.
- [109] M. W. Eltokhey, M. A. Khalighi, and Z. Ghassemlooy, "UAV location optimization in MISO ZF pre-coded VLC networks," *IEEE Wireless Communications Letter*, under revision.
- [110] J. Kennedy and R. Eberhart, "Particle swarm optimization," in *Proceedings of ICNN'95 - International Conference on Neural Networks*, Nov. 1995, vol. 4, pp. 1942–1948 vol.4, Perth, Australia.
- [111] Y. Wang, M. Chen, Z. Yang, T. Luo, and W. Saad, "Deep learning for optimal deployment of UAVs with visible light communications," *IEEE Transactions on Wireless Communications*, vol. 19, no. 11, pp. 7049–7063, 2020.
- [112] N. Kalikulov, R. C. Kizilirmak, and M. Uysal, "Unmanned-aerial-vehicle-assisted cooperative communications for visible light communications-based vehicular networks," *Optical Engineering*, vol. 58, no. 8, pp. 1–9, 2019.
- [113] A. Amantayeva, M. Yerzhanova, and R. C. Kizilirmak, "UAV location optimization for UAV-to-vehicle multiple access channel with visible light communication," in *2019 Wireless Days (WD)*, Apr. 2019, pp. 1–4, Manchester, UK.
- [114] A. Suleimen and R. C. Kizilirmak, "UAV assisted vehicular communication with VLC using NOMA," in *2020 12th International Symposium on Communication Systems, Networks and Digital Signal Processing (CSNDSP)*, July 2020, pp. 1–5, Porto, Portugal.
- [115] Z. Zhu, Y. Yang, C. Guo, M. Chen, S. Cui, and H. V. Poor, "Power efficient deployment of VLC-enabled UAVs," in *2020 IEEE 31st Annual International Symposium on Personal, Indoor and Mobile Radio Communications*, Aug. 2020, pp. 1–6, London, UK.
- [116] Y. Wang, M. Chen, Z. Yang, X. Hao, T. Luo, and W. Saad, "Gated recurrent units learning for optimal deployment of visible light communications enabled UAVs," in *2019 IEEE Global Communications Conference (GLOBECOM)*, Dec. 2019, pp. 1–6, Waikoloa, HI, USA.
- [117] Q. V. Pham, T. Huynh-The, M. Alazab, J. Zhao, and W. J. Hwang, "Sum-rate maximization for UAV-assisted visible light communications using NOMA: Swarm intelligence meets machine learning," *IEEE Internet of Things Journal*, vol. 7, no. 10, pp. 10375–10387, 2020.
- [118] Y. Shi and R. Eberhart, "A modified particle swarm optimizer," in *1998 IEEE International Conference on Evolutionary Computation Proceedings. IEEE World Congress on Computational Intelligence*, May 1998, pp. 69–73, Anchorage, USA.

- [119] A. Ratnaweera, S. K. Halgamuge, and H. C. Watson, "Self-organizing hierarchical particle swarm optimizer with time-varying acceleration coefficients," *IEEE Transactions on Evolutionary Computation*, vol. 8, no. 3, pp. 240–255, Jun. 2004.
- [120] C. Sauer, M. Schmidt, and M. Sliskovic, "Delay tolerant networks in industrial applications," in *2019 24th IEEE International Conference on Emerging Technologies and Factory Automation (ETFA)*, Sep. 2019, pp. 176–183, Zaragoza, Spain.
- [121] T. Q. Wang, Y. A. Sekercioglu, and J. Armstrong, "Analysis of an optical wireless receiver using a hemispherical lens with application in MIMO visible light communications," *Journal of Lightwave Technology*, vol. 31, no. 11, pp. 1744–1754, 2013.
- [122] T. Chen, L. Liu, B. Tu, Z. Zheng, and W. Hu, "High-spatial-diversity imaging receiver using fisheye lens for indoor MIMO VLCs," *IEEE Photonics Technology Letters*, vol. 26, no. 22, pp. 2260–2263, 2014.
- [123] K. D. Dambul, D. C. O'Brien, and G. Faulkner, "Indoor optical wireless MIMO system with an imaging receiver," *IEEE Photonics Technology Letters*, vol. 23, no. 2, pp. 97–99, 2011.
- [124] A. H. Azhar, T. Tran, and D. O'Brien, "A Gigabit/s indoor wireless transmission using MIMO-OFDM visible-light communications," *IEEE Photonics Technology Letters*, vol. 25, no. 2, pp. 171–174, 2013.
- [125] K. Park, H. M. Oubei, W. G. Alheadary, B. S. Ooi, and M. Alouini, "A novel mirror-aided non-imaging receiver for indoor 2×2 MIMO-visible light communication systems," *IEEE Transactions on Wireless Communications*, vol. 16, no. 9, pp. 5630–5643, 2017.
- [126] T. Fath and H. Haas, "Performance comparison of MIMO techniques for optical wireless communications in indoor environments," *IEEE Transactions on Communications*, vol. 61, no. 2, pp. 733–742, 2013.
- [127] A. Nuwanpriya, S. Ho, and C. S. Chen, "Indoor MIMO visible light communications: Novel angle diversity receivers for mobile users," *IEEE Journal on Selected Areas in Communications*, vol. 33, no. 9, pp. 1780–1792, 2015.
- [128] T. Q. Wang, R. J. Green, and J. Armstrong, "MIMO optical wireless communications using ACO-OFDM and a prism-array receiver," *IEEE Journal on Selected Areas in Communications*, vol. 33, no. 9, pp. 1959–1971, 2015.
- [129] K. Park, W. G. Alheadary, and M. Alouini, "A novel mirror diversity receiver for indoor MIMO visible light communication systems," in *2016 IEEE 27th Annual International Symposium on Personal, Indoor, and Mobile Radio Communications (PIMRC)*, Sep. 2016, pp. 1–6, Valencia, Spain.

- [130] K. Park, H. M. Oubei, W. G. Alheadary, B. S. Ooi, and M. Alouini, "Design and experimental demonstration of mirror-aided non-imaging receiver for indoor MIMO-VLC systems," New York, NY, USA, Oct. 2016, HotWireless 16, pp. 66–70, Association for Computing Machinery, New York, NY, USA.
- [131] K. Park and M. Alouini, "Improved angle diversity non-imaging receiver with a help of mirror in indoor MIMO-VLC systems," in *2018 IEEE Wireless Communications and Networking Conference (WCNC)*, Apr. 2018, pp. 1–6, Barcelona, Spain.
- [132] M. Morales-Céspedes, H. Haas, and A. G. Armada, "Optimization of the receiving orientation angle for zero-forcing precoding in VLC," *IEEE Communications Letters*, vol. 25, no. 3, pp. 921–925, 2021.
- [133] C. He, T. Q. Wang, and J. Armstrong, "MIMO optical wireless receiver using photodetectors with different fields of view," in *2015 IEEE 81st Vehicular Technology Conference (VTC Spring)*, May 2015, pp. 1–5, Glasgow, UK.
- [134] H. Marshoud, D. Dawoud, V. M. Kapinas, G. K. Karagiannidis, S. Muhaidat, and B. Sharif, "MU-MIMO precoding for VLC with imperfect CSI," in *2015 4th International Workshop on Optical Wireless Communications (IWOW)*, Sep. 2015, pp. 93–97, Istanbul, Turkey.
- [135] I. Abdalla, M. B. Rahaim, and T. D. C. Little, "Dynamic FOV visible light communications receiver for dense optical networks," *IET Communications*, vol. 13, no. 7, pp. 822–830, 2019.
- [136] R. C. Kizilirmak, C. R. Rowell, and M. Uysal, "Non-orthogonal multiple access (NOMA) for indoor visible light communications," in *International Workshop on Optical Wireless Communications (IWOW)*, Sep. 2015, pp. 98–101, Istanbul, Turkey.
- [137] L. Dai, B. Wang, Y. Yuan, S. Han, C. I, and Z. Wang, "Non-orthogonal multiple access for 5G: solutions, challenges, opportunities, and future research trends," *IEEE Communications Magazine*, vol. 53, no. 9, pp. 74–81, Sept. 2015.
- [138] H. Marshoud, V. M. Kapinas, G. K. Karagiannidis, and S. Muhaidat, "Non-orthogonal multiple access for visible light communications," *IEEE Photonics Technology Letters*, vol. 28, no. 1, pp. 51–54, Jan. 2016.
- [139] S. Al-Ahmadi, O. Maraqa, M. Uysal, and S. M. Sait, "Multi-user visible light communications: State-of-the-art and future directions," *IEEE Access*, vol. 6, pp. 70555–70571, 2018.
- [140] R. K. Jain, D. M. W. Chiu, and W. R. Hawe, "A quantitative measure of fairness and discrimination," *Eastern Research Laboratory, Digital Equipment Corporation, Hudson, MA*, 1984.
- [141] H. Shi, R. V. Prasad, E. Onur, and I. G. M. M. Niemegeers, "Fairness in wireless networks: Issues, measures and challenges," *IEEE Communications Surveys & Tutorials*, vol. 16, no. 1, pp. 5–24, First Quarter 2014.

- [142] H. Shen, Y. Deng, W. Xu, and C. Zhao, "Rate-maximized zero-forcing beamforming for VLC multiuser MISO downlinks," *IEEE Photonics Journal*, vol. 8, no. 1, pp. 1–13, Feb. 2016.
- [143] Michael Grant and Stephen Boyd, "CVX: Matlab software for disciplined convex programming, version 2.1," <http://cvxr.com/cvx>, Mar. 2014.
- [144] Michael Grant and Stephen Boyd, "Graph implementations for nonsmooth convex programs," in *Recent Advances in Learning and Control*, V. Blondel, S. Boyd, and H. Kimura, Eds., Lecture Notes in Control and Information Sciences, pp. 95–110. Springer, 2008.
- [145] R. Wang, Q. Gao, J. You, E. Liu, P. Wang, Z. Xu, and Y. Hua, "Linear transceiver designs for MIMO indoor visible light communications under lighting constraints," *IEEE Transactions on Communications*, vol. 65, no. 6, pp. 2494–2508, Jun. 2017.
- [146] H. Elgala and T. D. C. Little, "Reverse polarity optical-OFDM (RPO-OFDM): dimming compatible OFDM for gigabit VLC links," *Opt. Express*, vol. 21, no. 20, pp. 24288–24299, Oct. 2013.
- [147] F. Zafar, D. Karunatilaka, and R. Parthiban, "Dimming schemes for visible light communication: the state of research," *IEEE Wireless Communications*, vol. 22, no. 2, pp. 29–35, 2015.
- [148] J. Gancarz, H. Elgala, and T. D. C. Little, "Impact of lighting requirements on VLC systems," *IEEE Communications Magazine*, vol. 51, no. 12, pp. 34–41, 2013.
- [149] J. A. Jacko, *Human Computer Interaction Handbook: Fundamentals, Evolving Technologies, and Emerging Applications*, CRC-press, 2012.
- [150] T. Wang, F. Yang, J. Song, and Z. Han, "Dimming techniques of visible light communications for human-centric illumination networks: State-of-the-art, challenges, and trends," *IEEE Wireless Communications*, vol. 27, no. 4, pp. 88–95, 2020.
- [151] Q. Wang, Z. Wang, and L. Dai, "Asymmetrical hybrid optical OFDM for visible light communications with dimming control," *IEEE Photonics Technology Letters*, vol. 27, no. 9, pp. 974–977, 2015.
- [152] Y. Yang, Z. Zeng, J. Cheng, and C. Guo, "An enhanced DCO-OFDM scheme for dimming control in visible light communication systems," *IEEE Photonics Journal*, vol. 8, no. 3, pp. 1–13, 2016.
- [153] H. Sugiyama, S. Haruyama, and M. Nakagawa, "Brightness control methods for illumination and visible-light communication systems," in *2007 Third International Conference on Wireless and Mobile Communications (ICWMC'07)*, Mar. 2007, Guadeloupe, French Caribbean.
- [154] A. B. Siddique and M. Tahir, "Joint brightness control and data transmission for visible light communication systems based on white LEDs," in *2011 IEEE Consumer Communications and Networking Conference (CCNC)*, Jan. 2011, pp. 1026–1030, Las Vegas, NV, USA.

- [155] A. B. Siddique and M. Tahir, "Joint rate-brightness control using variable rate MPPM for LED based visible light communication systems," *IEEE Transactions on Wireless Communications*, vol. 12, no. 9, pp. 4604–4611, 2013.
- [156] S. Tao, Y. Zuo, H. Yu, Q. Li, and Y. Tang, "Power allocation of non-orthogonal multiple access with variable on-off keying dimming control in visible light communication networks," in *2018 IEEE 18th International Conference on Communication Technology (ICCT)*, Oct. 2018, pp. 321–325, Chongqing, China.
- [157] D. Zhai, R. Zhang, L. Cai, B. Li, and Y. Jiang, "Energy-efficient user scheduling and power allocation for NOMA-based wireless networks with massive IoT devices," *IEEE Internet Things J.*, vol. 5, no. 3, pp. 1857–1868, Jun. 2018.
- [158] Y. Wu, K. Ni, C. Zhang, L. P. Qian, and D. H. K. Tsang, "NOMA-assisted multi-access mobile edge computing: A joint optimization of computation offloading and time allocation," *IEEE Trans. Veh. Technol.*, vol. 67, no. 12, pp. 12244–12258, Dec. 2018.
- [159] S. Shahsavari, F. Shirani, and E. Erkip, "A general framework for temporal fair user scheduling in NOMA systems," *IEEE J. Sel. Topics Signal Process.*, vol. 13, no. 3, pp. 408–422, Jun. 2019.
- [160] K. Lee and H. Park, "Modulations for visible light communications with dimming control," *IEEE Photon. Technol. Lett.*, vol. 23, no. 16, pp. 1136–1138, Aug. 2011.
- [161] Z. Wang, W. D. Zhong, C. Yu, J. Chen, C. P. S. Francois, and W. Chen, "Performance of dimming control scheme in visible light communication system," *Opt. Express*, vol. 20, no. 17, pp. 18861–18868, Aug. 2012.
- [162] X. You, J. Chen, H. Zheng, and C. Yu, "Efficient data transmission using MPPM dimming control in indoor visible light communication," *IEEE Photon. J.*, vol. 7, no. 4, pp. 1–12, 2015.
- [163] R. Mesleh, H. Elgala, and H. Haas, "On the performance of different OFDM based optical wireless communication systems," *IEEE J. Opt. Commun. Netw.*, vol. 3, no. 8, pp. 620–628, Aug. 2011.
- [164] Y. Wang and H. Haas, "Dynamic load balancing with handover in hybrid Li-Fi and Wi-Fi networks," *Journal of Lightwave Technology*, vol. 33, no. 22, pp. 4671–4682, 2015.
- [165] F. Wang, Z. Wang, C. Qian, L. Dai, and Z. Yang, "Efficient vertical handover scheme for heterogeneous VLC-RF systems," *IEEE/OSA Journal of Optical Communications and Networking*, vol. 7, no. 12, pp. 1172–1180, 2015.
- [166] M. S. Demir, H. B. Eldeeb, and M. Uysal, "CoMP-based dynamic handover for vehicular VLC networks," *IEEE Communications Letters*, vol. 24, no. 9, pp. 2024–2028, 2020.

- [167] A. M. Vegni and T. D. C. Little, "Handover in VLC systems with cooperating mobile devices," in *2012 International Conference on Computing, Networking and Communications (ICNC)*, Jan. 2012, pp. 126–130, Maui, HI, USA.
- [168] M. D. Soltani, H. Kazemi, M. Safari, and H. Haas, "Handover modeling for indoor Li-Fi cellular networks: The effects of receiver mobility and rotation," in *2017 IEEE Wireless Communications and Networking Conference (WCNC)*, Mar. 2017, pp. 1–6, San Francisco, CA, USA.
- [169] M. Rahaim and T. D. C. Little, "SINR analysis and cell zooming with constant illumination for indoor VLC networks," in *2013 2nd International Workshop on Optical Wireless Communications (IWOW)*, Oct. 2013, pp. 20–24, Newcastle upon Tyne, UK.
- [170] X. Wu and H. Haas, "Handover skipping for LiFi," *IEEE Access*, vol. 7, pp. 38369–38378, 2019.
- [171] E. Dinc, O. Ergul, and O. B. Akan, "Soft handover in OFDMA based visible light communication networks," in *2015 IEEE 82nd Vehicular Technology Conference (VTC2015-Fall)*, Sep. 2015, pp. 1–5, Boston, MA, USA.
- [172] M. S. Demir, F. Miramirkhani, and M. Uysal, "Handover in VLC networks with coordinated multipoint transmission," in *2017 IEEE International Black Sea Conference on Communications and Networking (BlackSeaCom)*, June 2017, pp. 1–5, Istanbul, Turkey.
- [173] M. W. Eltokhey, M. A. Khalighi, and Z. Ghassemlooy, "Dimming-aware interference mitigation for NOMA-based multi-cell VLC networks," *IEEE Communications Letters*, vol. 24, no. 11, pp. 2541–2545, 2020.
- [174] Mehmet Mert Sahin and Huseyin Arslan, "Waveform-domain NOMA: The future of multiple access," in *2020 IEEE International Conference on Communications Workshops (ICC Workshops)*, 2020, pp. 1–6.
- [175] Luxeon Star, "Luxeon Rebel star SR-01-WC310," <https://www.luxeonstar.com/cool-white-5650k-20mm-star-coolbase-led-235lm>.
- [176] Thorlabs, "Thorlabs PDA100A2," <https://www.thorlabs.com/thorproduct.cfm?partnumber=PDA100A2>.

